

**Thermal network model development for an extended  
range electric vehicle battery pack with experimental  
verification through dynamic environmental exposure**

by

Ryan Fillion

A Thesis Submitted in Partial Fulfillment  
of the Requirements for the Degree of

Master of Applied Science in Automotive Engineering

in

The Faculty of Engineering and Applied Science  
University of Ontario Institute of Technology

July 2017

© Ryan Fillion, 2017

## ABSTRACT

---

The primary objective of this thesis was to develop a thermal simulation model of the Chevrolet Volt battery pack, with focus placed on the influence of packaging components external to the cell modules, and on the pack's response to ambient environmental influences. The thermal network model representing the pack was refined experimentally using heat flux and temperature measurements taken over a series of more than 100 laboratory test runs on a production vehicle battery pack. The initial model representing lab conditions produced simulation results with very good accuracy, comparable to the level of signal noise itself. The verified and calibrated lab model was then modified to match the environment of the real vehicle, taking into consideration engine bay temperature, chassis temperature, underbody convection, and road radiation. This full thermal model was further checked using road test data, and still reproduced temperature and heat flow with accuracy comparable to the initial lab test runs. The final thermal network representation can be employed in conjunction with a separate powertrain simulation model to perform a complete vehicle dynamic analysis regarding battery thermal effects through a wide range of drive profiles combined with environmental exposure conditions.

**Keywords:** dynamic thermal model, thermal network, battery pack, PHEV, EREV, battery thermal management, heat flux measurement, air flow measurement, road testing, Chevrolet Volt

## **ACKNOWLEDGEMENTS**

---

I am extremely grateful for the guidance and support provided by my supervisor Dr. Greg Rohrauer. Working in his lab over the years has given me the opportunity to learn many new things that I would have otherwise missed out on. His wealth of knowledge in many areas and ability to examine things from different perspectives have really pushed me to deepen my understanding to the point where I am confident in the work I have done.

Thanks to my friends and lab mates Kathryn and Lokendra for helping me set up countless tests, and for helping me brainstorm solutions to the numerous problems I encountered. I am also grateful for the support from my girlfriend, family, and friends.

# TABLE OF CONTENTS

Abstract.....	i
Acknowledgements.....	ii
List of Figures.....	vii
List of Tables.....	xii
Nomenclature.....	xiv
1 Introduction .....	1
1.1 Major Project Details.....	1
1.2 Combined Powertrain and Battery Pack Thermal Model.....	1
1.3 Thesis Objectives.....	3
2 Background On Battery Thermal Management.....	4
2.1 Battery Thermal Management in Electrified Vehicles .....	4
2.1.1 Types of EVs.....	4
2.1.2 Importance of Thermal Management.....	5
2.1.3 Thermal Management Strategies .....	6
2.2 Effects of External Conditions on BTMS Operation .....	8
3 Literature Review: Thermal Modelling.....	11
3.1 Introduction .....	11
3.2 CAD Modelling.....	12

3.3	Thermal Equivalent Circuit Modelling.....	13
3.3.1	Background.....	13
3.3.2	Review of Battery Pack Modelling Using Thermal Equivalent Circuits	17
3.4	Summary.....	21
4	Experimental Methods.....	23
4.1	Overview.....	23
4.1.1	Goals for the Lab Model.....	23
4.1.2	Battery Pack Description.....	23
4.1.3	Original Model.....	25
4.2	Measurements.....	26
4.2.1	Experimental Setup.....	27
4.2.2	Thermal Resistance Measurement.....	42
4.2.3	Effect of emissivity on measurements.....	52
4.2.4	Heat Flux Measurement Validation.....	57
5	Model Development and Validation.....	58
5.1	Changes to Original Model.....	58
5.2	Steady-state Model.....	59
5.2.1	Model Description.....	60
5.2.2	Simplification Process.....	70
5.2.3	Refinement.....	74

5.3	Dynamic Model.....	83
5.3.1	Addition of Capacitors .....	83
5.3.2	Modelling of a More Realistic Heat Source .....	85
5.3.3	Tuning of Interior Capacitor.....	87
5.4	Summary and Final Layout.....	89
5.5	Results .....	90
5.5.1	Simulation Validation.....	90
5.6	Summary and Conclusions .....	97
5.6.1	Summary.....	97
5.6.2	Recommendations.....	97
5.6.3	Conclusions .....	98
6	Thermal Model Adaptation to the Full Vehicle.....	99
6.1	Introduction .....	99
6.2	Airflow Measurement.....	100
6.2.1	Requirements and sensor selection .....	100
6.2.2	Hot-film Anemometer Operation and Circuit Implementation .....	101
6.2.3	Hot-film Anemometer Calibration .....	104
6.2.4	Complications and limitations.....	109
6.3	Road Testing.....	112
6.3.1	Instrumentation and Sensor Setup.....	113

6.3.2	Road Testing Overview .....	114
6.4	Environmental Source Adaptations .....	117
6.4.1	Front Bulkhead .....	117
6.4.2	Cover .....	122
6.4.3	Underbody Convection and Road Effects .....	125
6.4.4	Summary .....	138
6.5	Results .....	139
6.5.1	Results .....	141
6.6	Summary .....	146
7	Conclusion .....	148
7.1	Summary .....	148
7.2	Conclusions .....	149
7.3	Contributions .....	152
7.4	Future Work .....	153
	References .....	155
	Appendices .....	163
	Appendix A: Resistor Tolerance Sheet .....	163
	Appendix B: Transient Lab Testing Results @ 37 °C .....	165

## LIST OF FIGURES

---

Figure 1.1 – Basic visual representation of the thermal network model sub-sections	2
Figure 3.1 - Structural comparison between Cauer and Foster ladder models.....	17
Figure 3.2 - Example of a two-resistor thermal model of a cylindrical cell [88].....	18
Figure 3.3 – (a) Complex cell thermal network, (b) external thermal model including cooling plate and insulated wall; adapted from [92] .....	20
Figure 4.1 - Lab EREV battery pack .....	24
Figure 4.2 - Original thermal network.....	25
Figure 4.3 - Fluid conditioning cart setup (a) with outlined fluid loops: Loop 1 – pack circulation loop and Loop 2 – bypass loop (b) .....	27
Figure 4.4 – Effect of a step fluid temperature input on system response; ideal input (red), preheat response (black), no preheat response (grey).....	29
Figure 4.5 - Fluid port temperature and pressure drop measurement.....	31
Figure 4.6 - Thermocouple mounting method .....	33
Figure 4.7 - Omega HFS-4 heat flux sensor .....	34
Figure 4.8 - Typical heating and cooling response: Temperature (°C) vs Time (h)...	40
Figure 4.9 - Spatial difference in manifold temperature .....	42
Figure 4.10 - Cell frame schematic, showing separate heat flow paths.....	44
Figure 4.11 - Side path sensor placement .....	45
Figure 4.12 – Foil-covered heat pad experiment.....	53
Figure 4.13 - Sensor heat flux with varying pad heat flux .....	54
Figure 4.14 - Foil and sensor temperatures at varying heating rates .....	55
Figure 4.15 - Outside cover thermocouples covered in foil (outlined).....	56
Figure 5.1 - Preliminary lab battery pack thermal model.....	59
Figure 5.2 - Bulkhead resistances.....	61

Figure 5.3 - Bulkhead measurement points: outside (left), inside (right).....	61
Figure 5.4 –Manifold resistance chain.....	63
Figure 5.5 - Side path resistances.....	64
Figure 5.6 – Top resistance chain.....	65
Figure 5.7 - Endplate path resistances .....	67
Figure 5.8 - Endplate cover sections .....	68
Figure 5.9 – Bottom heat flow path .....	68
Figure 5.10 – Steady-state thermal network with reduced cover path (with legend) .....	71
Figure 5.11 – Schematic showing the equivalency between a resistor and a modified GVALUE component.....	75
Figure 5.12 - $R_{obh}$ PSpice component properties with output current expression.....	77
Figure 5.13 - Schematic detailing the electrical connections for $R_{obh}$ .....	77
Figure 5.14 - Final reduced steady-state thermal network.....	83
Figure 5.15 - Heat flow limit (W per cell) vs. input heat flow at 3, 6, and 9 Lpm.....	86
Figure 5.16 - Input heat rate: experimental vs simulation .....	88
Figure 5.17 - Final transient lab model .....	89
Figure 5.18 - Simulated vs. measured temperatures: endplate, top, and baseplate..	91
Figure 5.19 - Simulated vs. measured temperatures: side and manifold .....	91
Figure 5.20 - Simulated vs. measured temperatures: bulkhead, inside cover, and outside cover .....	92
Figure 5.21 - Simulated vs. measured heat flow: top and bulkhead .....	94
Figure 5.22 - Simulated vs. measured heat flow: side, manifold, and endplate .....	95
Figure 5.23 - Simulated vs. measured heat flow: baseplate and cover .....	95
Figure 6.1 - Hot-film airflow sensor construction [106] (left) and sensor with size comparison (right) .....	102

Figure 6.2 - Manufacturer recommended circuit for FS5 [106] (left) and custom sensor board (right).....	103
Figure 6.3 - Calibration tunnel setup (not to scale).....	105
Figure 6.4 – Calibration data for hot-film sensor voltage to mass flow rate (kg/h) with 3 <sup>rd</sup> , 4 <sup>th</sup> , and 5 <sup>th</sup> order polynomial curve fits.....	107
Figure 6.5 - Depiction of air flow over the hot-film sensor at yaw angles of 0° and 15° .....	109
Figure 6.6 - Flow sensor placement inside of tube with corresponding directions	110
Figure 6.7 - Vane anemometer placement inside of calibration tunnel .....	111
Figure 6.8 - Underside of baseplate with thermocouples and heat flux sensors attached .....	114
Figure 6.9 - View of vehicle underbody depicting major components and general thermocouple locations.....	118
Figure 6.10 - Bulkhead heat flow path schematic modified to represent the vehicle’s environment .....	118
Figure 6.11 - Exact location of the front thermocouple between the engine and firewall .....	119
Figure 6.12 - Comparison of firewall, bulkhead, and underbody air temperatures during test run #9.....	120
Figure 6.13 – Vehicle speed (km/h) and engine power (kW) profiles for road test #9 .....	120
Figure 6.14 - Air temperatures and vehicle speed during road test #9 .....	121
Figure 6.15 - Thermal network schematic of the cover path as modelled for the vehicle .....	122
Figure 6.16 - View from the rear driver side of two chassis temperature thermocouples .....	123
Figure 6.17 - Top view of the pack rear showing the approximate location for the middle sensor .....	123
Figure 6.18 – Underbody shield: on the vehicle (left) and removed showing the interior face (right) .....	126

Figure 6.19 – Shield resistor broken up into its constituents (left) and combined baseplate/shield thermal network (right).....	127
Figure 6.20 - Baseplate temperature with shield attached: experimental vs. simulation .....	128
Figure 6.21 –Current output expression for $R_{rad}$ PSpice component with corresponding equation terms .....	130
Figure 6.22 - Underbody air velocity and vehicle speed (km/h) for road test run #4 .....	131
Figure 6.23 - Underbody air velocity and vehicle speed (km/h) for highway speed road test run #5.....	131
Figure 6.24 – Full baseplate path including shield, convection, and radiation sources .....	134
Figure 6.25 - Baseplate environment test network.....	134
Figure 6.26 – Static parking lot test temperature conditions (top) and experimental vs simulation baseplate heat flow in mW per cell (bottom) .....	136
Figure 6.27 - Commuting drive cycle inputs: air speed in m/s (top) and temperature sources (bottom).....	137
Figure 6.28 - Heat flow out of baseplate (mW per cell): experimental vs simulation .....	137
Figure 6.29 - Full thermal network model with adaptations made to match the vehicle .....	139
Figure 6.30 - Input temperature sources for parking lot heat soak.....	140
Figure 6.31 - Baseplate temperature: experimental vs simulation during heat soak .....	141
Figure 6.32 –Baseplate heat flow: experimental vs simulation during heat soak....	142
Figure 6.33 - Average fluid temperature during heat soak test: experimental vs simulation .....	143
Figure 6.34 – Comparison of A/C compressor power to simulation input source heat flow (W per cell) with correlated inlet fluid temperature .....	143
Figure 6.35 – Power profiles ( $\dot{Q}_{in}$ and $\dot{W}_{comp}$ ) during active cooling with corresponding COP .....	145

Figure A1 - Simulated vs. measured temperatures: endplate, top, and baseplate ...	165
Figure A2 - Simulated vs. measured temperatures: side and manifold.....	165
Figure A3 - Simulated vs. measured temperatures: bulkhead, inside cover, and outside cover .....	166
Figure A4 - Simulated vs. measured heat flow: top and bulkhead .....	167
Figure A5 - Simulated vs. measured heat flow: side, manifold, and endplate.....	167
Figure A6 - Simulated vs. measured heat flow: baseplate and cover .....	168

## LIST OF TABLES

---

Table 3.1 - Analogous quantities between electrical and thermal circuits .....	14
Table 3.2 - RC element configurations used in building thermal modelling.....	16
Table 4.1 - Direct measurement uncertainties with bit resolution.....	38
Table 4.2 - Heat flow balance through cover path for all tests.....	57
Table 5.1 - Legend for Figure 5.1: temperature nodes and thermal resistance nomenclature .....	60
Table 5.2 - Changes to resistances from the simplification of the airgap, cover, and ambient paths.....	72
Table 5.3 – Steady-state nodal temperatures: experimental vs. simplified simulation .....	73
Table 5.4 - Steady-state heat flow: experimental vs. simplified simulation .....	73
Table 5.5 - Resistance changes with temperature .....	74
Table 5.6 - Voltage-controlled resistor lookup tables for $R_{bh1}$ , $R_{obp}$ , $R_{oc}$ , and $R_{obh}$ , .....	76
Table 5.7 – Steady-state nodal temperatures: experimental vs. simplified simulation with variable resistors .....	78
Table 5.8 - Steady-state heat rates: experimental vs. simplified simulation with variable resistors .....	79
Table 5.9 - List of resistor tolerances, changes, and final values.....	80
Table 5.10 – Steady-state nodal temperatures: experimental vs. simplified simulation with variable resistors .....	81
Table 5.11 - Steady-state heat rates: experimental vs. simplified simulation .....	82
Table 5.12 - Absolute maximum and RMS errors in temperature during transient heating.....	93
Table 5.13 - Absolute maximum and RMS errors in heat flow during transient heating and signal noise levels .....	96
Table 6.1 – Outer cover resistance $R_{oc}$ evaluated at different outer cover temperatures $T_{oc}$ .....	125

Table A1 - Resistor tolerance data ..... 163

Table A2 - Resistor tolerance data continued..... 164

Table A3 - Absolute maximum and RMS errors in temperature during transient heating..... 166

Table A4 - Absolute maximum and RMS errors in heat flow during transient heating and signal noise levels ..... 168

## NOMENCLATURE

---

$A$	Area {m <sup>2</sup> }
$B$	Measurement component bias
$Bi$	Biot number
$C$	Thermal capacitance {J/°C} or {J/K}
$c_p$	Specific heat capacity {J/kgK}
$h$	Heat transfer coefficient {W/m <sup>2</sup> K}
$k$	Thermal conductivity {W/mK}
$L$	Characteristic length {m}
$m$	Mass {kg}
$\dot{m}$	mass flow rate {kg/s}
$Nu$	Nusselt number
$Pr$	Prandtl number
$\dot{q}$	Heat flux {W/m <sup>2</sup> }
$\dot{Q}$	Rate of heat flow {W}
$R$	Thermal resistance {°C/W} or {K/W}
$Re$	Reynolds number
$S$	Precision index of measurement
$T$	Temperature {°C} or {K}
$U$	Resultant uncertainty
$V$	Velocity {m/s}
$\dot{V}$	Volumetric flow rate {m <sup>3</sup> /s}
$\dot{W}$	Power {W}
$\Delta T$	Temperature differential {°C}
$\varepsilon$	Emissivity
$\nu$	Kinematic viscosity {m <sup>2</sup> /s}
$\rho$	Density {kg/m <sup>3</sup> }
$\sigma$	Stefan-Boltzmann constant

## Subscripts

$ag$	Airgap
$amb$	Ambient environment
$avg$	Average
$bh$	Bulkhead
$bh1$	Fluid to bulkhead
$bh2$	Inside pack to bulkhead
$bot$	Bottom frame
$bp$	Baseplate
$c$	Battery pack cover
$chassis$	Vehicle chassis
$comp$	Compressor

<i>cond</i>	Conduction
<i>conv</i>	Convection
<i>end</i>	Endplate
<i>eng</i>	Engine compartment
<i>ic</i>	Inner surface of battery pack cover
<i>in</i>	Into battery pack
<i>int</i>	Internal of modules
<i>M</i>	Measurement
<i>man</i>	Manifold
<i>obh</i>	Outside surface of bulkhead
<i>obp</i>	Outer surface of baseplate
<i>oc</i>	Outer surface of battery pack cover
<i>out</i>	Out of battery pack
<i>R</i>	Result
<i>rad</i>	Radiation
<i>sh</i>	Baseplate debris shield
<i>side</i>	Side frame
<i>top</i>	Top frame path
<i>top1</i>	Top surface of retention frame
<i>top2</i>	Top surface of battery terminal cover
<i>tot</i>	Total

## Abbreviations

ABM	Analog behavioural modelling
BEV	Battery electric vehicle
BMS	Battery management system
BTMS	Battery thermal management system
CAD	Computer-aided design
CCA	Constant current anemometer
CFD	Computational fluid dynamics
COP	Coefficient of performance
CTA	Constant temperature anemometer
CTD	Constant temperature difference
DAQ	Data-acquisition
DC	Direct current
EREV	Extended-range electric vehicle
ESS	Energy storage system
EV	Electrified vehicle
FE	Finite element
fs	Full-scale
HEV	Hybrid electric vehicle
ICE	Internal combustion engine
Lpm	L/min
PHEV	Plugin hybrid electric vehicle
PTC	Positive temperature coefficient

RMS	Root mean square
RSS	Root sum of squares
RTD	Resistance temperature detector
SOC	State of charge
SPICE	Simulation program with integrated circuit emphasis

# 1 INTRODUCTION

---

## 1.1 MAJOR PROJECT DETAILS

The work presented in this thesis is part of a larger research project involving a comprehensive investigation of thermal management systems in electrified vehicles, with much of the focus on improving battery thermal management system function of the first generation Chevrolet Volt. Improving such systems can lower cost, improve vehicle range, and prolong battery life. Investigations as a part of this larger project have included the use of phase-change materials for battery thermal management [1], modelling and control of a thermoelectric heat pump [2], [3], thermoelectric devices utilizing metal foam heat-exchangers [4], and exploring battery pack insulation strategies [5].

## 1.2 COMBINED POWERTRAIN AND BATTERY PACK THERMAL MODEL

The most recent branch of the project was the development of a full vehicle powertrain model incorporating a complete battery pack thermal model. Such a comprehensive simulation model provides the ability to study the effects of climate on the vehicle and battery system for any drive profile. The research group has published some preliminary work discussing the development and capabilities of this model [6].

The powertrain model of the extended-range electric vehicle (EREV) was developed and refined in *Autonomie*, a Matlab based program formerly known as PSAT (Powertrain Systems Analysis Toolkit), which can be run through any drive cycle, and produce battery pack information such as voltage, current, state of charge, etc. The main issue is that the performance of the battery pack relies heavily on the operating temperature of the cells; this uncovered the need for a full battery pack thermal model that can run alongside *Autonomie*.

The equivalent circuit method for thermal modelling was chosen due to its low computational requirements and high speed. The electrical circuit simulation program ORCAD PSpice, is used to solve the thermal network rapidly. The original thermal network model was developed analytically, in an attempt to model the entire construction of the battery pack, including external environmental effects. Two graduate students (including the author) took on the realization of further refining this battery pack thermal model experimentally, an effort that is wholly lacking in the literature. The experimental process provides validation points but more importantly, improves the understanding of the thermal dynamics within this complex system allowing for the development of a more accurate thermal network representation.

Due to the complexity of the thermal interactions of a full size battery pack, the modelling was split into two portions: 1) the cell module assembly and 2) external construction and environment. Figure 1.1 depicts the two portions of the full model, with their respective heat loads and physical components.

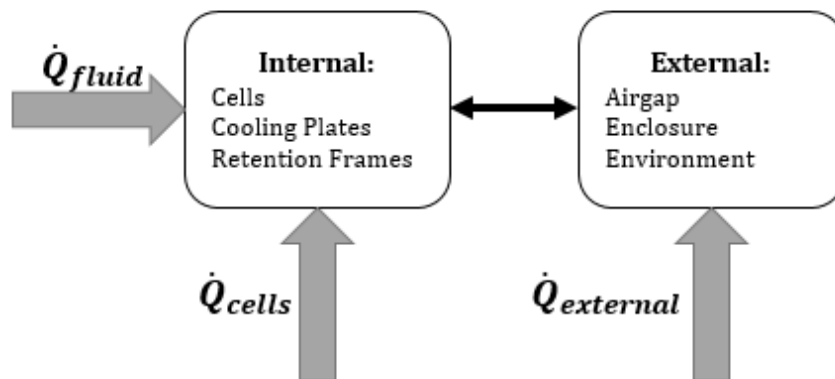


Figure 1.1 – Basic visual representation of the thermal network model sub-sections

The modelling of the internal module assembly is being conducted in parallel to the present endeavour by another student. This encompasses the cells (with heat generation) and their interactions with the cooling plates, and the surrounding retention frames. The external portion (author’s work) encompasses the heat transfer outward of the cell-retention frames. This consists of an airgap between the

modules and the enclosure cover, the enclosure itself, and its interactions with the local environment.

### **1.3 THESIS OBJECTIVES**

The main goal was to experimentally refine a thermal network model that accurately predicts temperatures and rates of heat flow for specific components of a full EREV battery pack assembly during transient and steady states. The investigation and dynamic modelling of the environmental sources surrounding the battery pack (road radiation, convection, and chassis influence) was necessary to extend the model's functionality in order to mimic the installation on a real vehicle, allowing the thermal model to be linked to the Autonomie powertrain model. Faster than real time simulation speeds are required for this to function alongside the Autonomie model in practice, and also for the possibility to have such simulation embedded into a predictive battery thermal management control system for future application. The pack thermal model also entails the need for identifying corresponding physical significances, allowing design changes to be analytically derived and easily applied to the thermal network. A secondary objective for this thesis was to share some of the insight gained during the experimental measurement process, in order to help others conduct similar experiments more readily and accurately.

## **2 BACKGROUND ON BATTERY THERMAL MANAGEMENT**

---

A short overview on some key aspects relating to battery thermal management in electrified vehicles (EVs), such as thermal operating conditions and thermal management strategies is outlined. The effects of environmental factors on the operation and lifespan of batteries are also discussed. This background is introduced in order to help clarify the motivation behind developing a full battery pack thermal model.

### **2.1 BATTERY THERMAL MANAGEMENT IN ELECTRIFIED VEHICLES**

#### **2.1.1 Types of EVs**

A hybrid electric vehicle (HEV) employs an internal combustion engine (ICE) as the main power plant, but also uses an electric motor to load-level and assist the ICE. There are different degrees of hybridization, which indicate the level of assistance delivered by the electric machine(s). A mild hybrid, such as the first generation Honda Insight, employs an electric motor/generator in parallel to assist the engine with propulsion. A full (strong) hybrid, such as the Toyota Prius, has a power-split type transmission that also allows for pure electric propulsion. The power is split between two electric machines and the ICE, which permits the engine to be loaded down or tuned off in order to operate the vehicle more efficiently.

A plugin hybrid (PHEV) is essentially a full hybrid with a larger battery pack that allows for a much longer duration of pure electric propulsion. These vehicles can operate in either charge-sustaining or charge-depleting modes. In charge-depleting mode, the battery provides the bulk of propulsion power and is therefore being discharged. In charge-sustaining mode, engine power is used to recharge the batteries in order to maintain the battery pack near its lowest permissible state of charge (SOC). Like HEVs, PHEV battery packs are also partially recharged from regenerative braking and engine power, but are primarily designed for charging from the power

grid due to their much larger energy capacity. An extended-range electric vehicle (EREV) is PHEV where the ICE does not normally provide direct torque to the wheels, and therefore operates in a pure electric propulsion mode over long distances. The mechanical power from the engine is converted to electrical power by the means of an electric motor/generator, which is used to recharge the battery pack and/or to provide propulsion torque in combination with the traction motor. In charge-depleting mode, the engine is turned off and the “generator” can operate as a second traction motor using a power split device [7]. Two popular EREVs on the present market are the Chevrolet Volt and the BMW i3 REx. Battery electric vehicles (BEVs), such as the Nissan Leaf and Tesla Model S and X, offer the highest level of electrification. These vehicles always use pure electric propulsion and even larger battery packs (up to ~100 kWh) in order to increase their driving range. The work described in this thesis applies mainly to PHEVs, EREVs, and BEVs since the battery thermal management system becomes quite significant in these types of vehicles.

### **2.1.2 Importance of Thermal Management**

One of the main obstacles faced by EV manufacturers is to extend battery longevity to span the expected life of the vehicle. Based on the United States Council for Automotive Research (USCAR), which is formed by the big three American auto manufacturers, the current battery calendar life goal is 10 years, and the future goal for 2018-2020 is 15 years [8]. The calendar life of a battery pack is determined by many factors such as cell chemistry, frequency of use, depth of discharge, charging rates, and operating temperature [9].

Batteries can have a large thermal operating window of -40 to 70 °C, depending on the cell chemistry. The internal impedance however varies greatly over this range of temperatures, which directly affects electrical performance. A higher impedance increases the internal voltage drop of the cell, which in turn decreases its available power output and capacity [10]. This translates directly to a loss in vehicle performance and range. Nagasubramanian [11] measured the power and energy densities of common 18650 lithium-ion batteries and showed that the internal

impedance increases significantly as temperatures dip below freezing. At -40 °C, a reduction in power density greater than 95% was observed when compared to battery performance at 25 °C. Poor performance was also observed at -20 °C (~75% reduction). The internal impedance also increases with elevated temperatures, but here the risk of thermal runaway with lithium-ion batteries is much more serious.

Extreme temperatures also cause permanent cell damage, which accelerates capacity fade over time. The result is a decrease in all-electric range and in battery calendar life. A recent example was the battery degradation experienced by Nissan Leaf owners who live in hot climates. Vehicles driven in locations where ambient temperatures regularly exceeded 32 °C experienced large capacity losses (up to 28%) in the first year of use [12]. This issue is mainly due to inadequate thermal management since it involves an air-cooled battery pack.

In sum, the purpose of a vehicle's battery thermal management system (BTMS) is to maintain the temperature of the batteries within an optimal range, in order to prolong battery life and help prevent thermal runaway. The optimum temperature range is centred on where internal impedance is minimized, which is generally slightly above room temperature (25-40 °C) [13]. An efficient method of reaching and maintaining this temperature interval is the key to reducing the BTMS' impact on vehicle range as well as increasing battery life.

### **2.1.3 Thermal Management Strategies**

Two main types of thermal management strategies are utilized in present day battery packs: forced air and liquid. BTMS types are categorized based on their method of heat transfer used to cool and heat the batteries. The term "cooled" is often elected to describe the function of the BTMS since its usual purpose is to cool the batteries, but in most cases it also applies to heating, which is relevant in cold climates.

The simplest type of BTMS uses forced air as the heat transfer medium. A fan is employed to draw air from the cabin over the outer surface of the cells. This strategy

is commonly used in HEV and PHEV battery packs since they are relatively small in size and mass [14], [15]. Because air has both low thermal conductivity and heat capacity, a large exposed surface area to volume ratio for every cell is required to allow sufficient heat transfer. This requires the cells to be spaced apart, thus decreasing packaging efficiency, which is an important parameter in battery pack design, particularly for large packs. Air-cooled packs that use a single inlet and outlet tend to generate temperature gradients between cells; this lowers performance by causing charge imbalances within the pack [16]–[18]. Uniformity of conditions is important since the most degraded cell in a pack essentially determines the limits of operation across the whole assembly. In BEVs, EREVs, and some PHEVs, there is a higher current demand on the battery pack which in turn generates even more heat; here, an air cooled BTMS strategy becomes ineffective. More sophisticated liquid systems are usually required in these cases.

In liquid systems, a heat transfer fluid, normally an ethylene glycol mix, circulates through a heat exchanger that is in thermal contact with the cells. A refrigerant loop is used to chill the coolant, and resistive heaters are typically employed to heat the fluid; EREV's have the added benefit of utilizing engine heat and generator power to warm the fluid. These systems are designed for uniform cooling at every cell to prevent pack level degradation. The structure of the cooling mechanism is dependent on the cell packaging arrangement. For example, the Chevrolet Volt uses pouch cells, which are thin, rectangular and have no hard shell casing. The cells are placed in direct contact with the cooling plate, and the entire assembly is held together by plastic frames [19], [20]. This design creates an effective cooling system due to the high thermal contact area and also allows for very compact packaging. The Tesla Model S on the other hand uses thousands of small cylindrical cells which have a low thermal mass for their surface area. In this battery pack, the fluid circulates through a heat exchanger tube that is in contact with almost half of each cell perimeter [21]. Another liquid cooling method involves the use of direct refrigerant expansion, as implemented in the BMW i3. The base plate of this battery pack is constructed from aluminium which houses a series of refrigerant tubes. The cell modules are also

aluminum-encased and mounted in thermal contact with the heat exchanger base, which pulls heat away from the batteries [22].

In every case, the BTMS requires power from the battery pack in order to operate refrigeration and pumping systems. In PHEVs and BEVs, this power can also be supplied via the grid, in order to pre-condition the pack when vehicle is plugged in. It can be concluded that the effectiveness of the BTMS has a direct impact on the range and longevity of an EV, which is a main concern for consumers. The design of the active portion of a BTMS (i.e. cooling system) gets attention and focus in the literature, but an important passive aspect of thermal management is often overlooked, insulation. The next section will discuss the effects that insulation has on BTMS operation and provide some added details for the motivation behind this thesis.

## **2.2 EFFECTS OF EXTERNAL CONDITIONS ON BTMS OPERATION**

In general, a BTMS should be designed to provide enough cooling based on the highest rate of heat generation within the cells, but this may not be sufficient once environmental factors come into play. A prime example would be a vehicle parked, unplugged, in the sun over the period of an average summer work day. The vehicle and battery pack will be absorbing heat from the surroundings during this time, up until the owner drives off. In this case, the battery could be at a temperature well above ambient, and the cooling system would be deployed to operate at full load in order to quickly cool the system. This cooling power is provided by the battery pack itself, which means that the cells are operating at non-ideal temperatures and generating more heat. Additionally, if the vehicle owner begins to drive aggressively, the operating conditions for the cells worsen, reducing their lifespan further. To account for such circumstance, the vehicle requires an over-engineered cooling system, which is more expensive and unnecessary most of the time. At the opposite end of the spectrum, temperatures below  $-25\text{ }^{\circ}\text{C}$  (not uncommon in Canada) could render the system almost inoperable or pose a high risk of damage. In this case, PHEVs rely on the ICE to cover operating needs, which is not possible in BEVs.

A way to mitigate this problem is to better insulate the cells from both the environment and the thermal mass of the packaging surrounding them. By reducing the parasitic influence of the surroundings, the BTMS can fulfill its intended purpose more efficiently. It can be thought of as reducing the battery pack's time constant in response to the cooling/heating system. This change will shorten the amount of time and energy required to cool or heat the battery pack, increasing overall system efficiency.

Added insulation increases the battery pack's time constant in response to external conditions by lowering the rate of heat leakage to/from the environment. This decreases the frequency at which the BTMS is required to operate, and in the parking lot case referenced, better insulation would reduce the temperature rise of the battery pack during the day. Nelson et al. [23] discussed this effect but did not show any results. The temperature rise of an HEV battery pack, wrapped in 10 mm of insulation, over the period of a day was simulated, and the battery temperature increased by 50% of the difference between the battery and ambient over a period of 7 h. It was suggested that insulation should be doubled in order to increase the battery's time constant. Carlson et al. [24] tested the battery system performance and fuel consumption of two production HEVs in sub-zero temperatures. The vehicles were driven during the day and parked outside overnight where the ambient temperature was -15 °C. The battery pack that was better insulated reached -8 °C, whereas the other battery had already reached ambient. Battery function was limited below 0 °C and fuel economy was halved. This illustrates the point that by insulating the batteries, greater vehicle energy efficiency can be achieved.

A formal study on the Chevrolet Volt's cold weather on-road performance [25] has shown that once temperatures descend below freezing, the ICE operates more frequently, consuming more gasoline. Additionally, the all-electric range decreased at a rate of approximately 1 km per °C as temperatures decreased from 10 °C to -4 °C. At -26 °C, the vehicle's all-electric range was reduced to 47% of its original range (at 21°C).

Yuksel et al. [9] recently (2017) published a study examining various effects on PHEV battery life using a coupled powertrain and thermal model. Their comprehensive model was used to simulate normal daily use with varying degrees of severity in climate and driving style. They concluded that simply employing (air) cooling while operating in mild climates is extremely beneficial for battery health, predicting a battery calendar life of nearly twice that of a no cooling and hot climate case.

The effects of extreme daily temperatures (loss of range, shortened battery life) are often discussed in car owner forums and in the media, but research pertaining to the exploration and mitigation of these effects is very scarce. There are countless studies discussing heat/cold soaks on individual cells, but little information regarding the external influences on battery packs or the interaction between the cells and their packaging. The motivation underlying this work is to create a thermal model that can accurately predict environmental effects on the batteries. The key aspect of the model is the ability to predict the impact of certain physical design changes, on the thermal dynamics of the entire battery system. Such analysis leads to identifying and quantifying the most effective design changes, which can be implemented at minimal cost to maximize the effectiveness of any added insulation or thermal mass and the resultant performance increment.

## 3 LITERATURE REVIEW: THERMAL MODELLING

---

### 3.1 INTRODUCTION

The previous chapter provided some general background about EVs and thermal management. Reasons for improving insulation strategies were discussed, highlighting a lack of formal research in the area. This section serves as a literature review pertaining to thermal modelling of EV battery systems. The two main types of modelling approaches are compared: CAD and thermal equivalent circuits. Justification for the use of thermal network modelling for the present application is provided.

The key function of a thermal model is to accurately predict transient and steady-state temperatures and rates of heat flow at points of interest when the system is subjected to a set of realistic inputs and boundary conditions. Thermal models are beneficial tools for battery pack and BTMS designers. (1) Cell models can be used to determine cooling system requirements based on internal heat generation. (2) Cooling system models can be deployed to evaluate the effectiveness of heat removal and assess design changes. (3) A thermal model of the cell surroundings (frames, enclosure, and environment) can be employed to evaluate the level of insulation provided by the battery pack enclosure and analyze heat leakage paths. Using the three types of thermal models, designers are able analyze the entire battery system, evaluate design iterations, and improve battery operating conditions. Coupling a comprehensive battery thermal model to a powertrain model can provide useful information about energy consumption during standard drive cycles. The impact of battery pack construction and BTMS operation strategies on vehicle range can be examined along with many other scenarios. This is one of the goals among the author's research group [6], and the work in this thesis relates to the development of a thermal model for the cell surroundings of the Chevrolet Volt vehicle platform.

## 3.2 CAD MODELLING

A prominent method of battery pack thermal modelling is to create a virtual model using computer-aided design (CAD) software, and to conduct finite element (FE) or computational fluid dynamics (CFD) simulations to evaluate the design. A major advantage of CAD methods is accurate modelling of complex geometry which describes the physical layout of the design and material properties. FE and CFD methods have been shown to provide accurate results when utilized correctly; this requires thorough understanding of the necessary boundary conditions, meshes, thermal interfaces, and simulation parameters.

CFD models are useful in understanding and characterizing fluid flow in and around battery packs. Aspects of air-cooled battery pack design such as manifold construction/layout [26]–[29], airflow strategies [28], [30], [31], and cell arrangements [32], [33] have been investigated using CFD. Cooling channel design for liquid-cooled battery packs have also been investigated through CFD studies [34]–[36]. CFD was similarly employed by Javani et al. to investigate the effects of phase change material on a cell [37]. Heat transfer coefficients that are difficult to determine analytically due to complex convection currents can be derived from CFD simulations [33], [35], [38], [39]. These external effects can be used as boundary conditions in FE simulations or as external resistances in a thermal network model.

FE models used for battery pack thermal analysis generally consist of either a cell or a module with varying degrees of structure surrounding the cells [13], [40]–[45]. It is common to use cell heat generation values as inputs to the models, and temperature distributions are analyzed based on different rates of cooling and battery layouts. FE simulations are also used to analyze and refine cooling strategies [46], [47].

CAD models of full-sized battery packs with considerations of the environment are limited in the literature. Mi et al. [46] modelled a 48 cell air-cooled HEV battery pack. The enclosure and surroundings were not ignored, but the casing was assumed to be well insulated, and the heat-spreading cooling plates were presumed to be effective

enough to neglect heat transfer from the cells to ambient. Mayyas et al. [48] modelled a Toyota Prius PHEV battery pack, and compared their model to drive cycle experiments conducted on a dynamometer. The simulation results predicted higher temperatures than expected, and the authors concluded that better modelling of the pack's surroundings was required.

Matthe et al. [19] briefly presented a CFD thermal model of a battery pack installed on a Chevrolet Volt (EREV). The effects of the exhaust system on enclosure temperatures were demonstrated, which indicates that some external factors were considered during the design of the vehicle. Brennan [5] modelled a full-sized EREV battery pack (detached from the vehicle) including the enclosure and surroundings using CFD. The battery pack was instrumented with thermocouples and subjected to a heat soak inside a thermal chamber; this test was used to validate the thermal model. Different levels of insulation around the enclosure were simulated along with some proposed modifications to the cell retention frames. A significant increase in the battery pack's thermal time constant in response to external heating was observed in simulations. The main drawback to this method was that the complexity of the pack design required multiple sub-models in order to capture the entire system. CAD models are very resource and time intensive, which is the prime reason for the lack of full battery pack simulations that include dynamic environmental effects.

### **3.3 THERMAL EQUIVALENT CIRCUIT MODELLING**

#### **3.3.1 Background**

A thermal equivalent circuit, also known as a thermal network or lumped-parameter thermal model, is a thermal model of a system represented by a network of interconnected components analogous to an electrical circuit. Electrical quantities are replaced by their thermal counterparts which are compared in Table 3.1.

Table 3.1 - Analogous quantities between electrical and thermal circuits

Quantity →	Across Variable	Through Variable	Dissipation Element	Storage Element
<b>Electrical</b> [unit]	Voltage - $V$ [V]	Current - $I$ [A]	Electrical resistance - $R$ [ $\Omega$ ]	Electrical capacitance - $C$ [F]
<b>Thermal</b> [unit]	Temperature - $T$ [ $^{\circ}$ C] or [K]	Rate of heat flow - $\dot{Q}$ [W]	Thermal resistance - $R$ [ $^{\circ}$ C/W] or [K/W]	Thermal capacitance (heat capacity) - $C$ [J/ $^{\circ}$ C] or [J/K]

The electrical analogy is often discussed in heat transfer textbooks, mainly relating to the development of thermal resistance networks. These are normally constructed to determine steady-state temperatures and heat fluxes at points of interest in a system. Examples of multi-layered walls and pipes are commonly given along with formulations for convection, radiation, and conduction resistances [49], [50].

Lumped-capacitance theory is another concept which relates the temperature change of a highly conductive body immersed in a fluid, to the charging of an electrical capacitor. In this case, the body is assumed to be at a uniform temperature since its internal conductive resistance is much smaller than the convective resistance on its outer surface. The ratio of these two thermal resistances is known as the Biot number which is found using Equation (3.1); where  $L$  is the body's characteristic length,  $A$  is its outer surface area,  $k$  is the conductivity of the material, and  $h$  is the convective heat transfer coefficient. Values of less than 0.1 are required for the lumped-capacitance representation to be seen as accurate. The fully uniform temperature assumption is limiting since it implies no temperature gradient across an object subjected to heat flow.

$$Bi = \frac{\text{internal conduction resistance}}{\text{external convection resistance}} = \frac{hL}{k} \quad (3.1)$$

A more reasonable assumption for less specific systems is that temperature varies in one spatial direction; this is known as a partially-lumped system [51]. This method

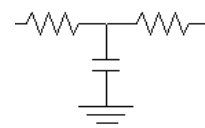
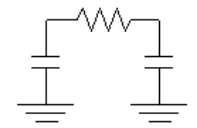
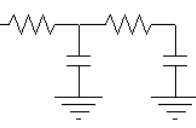
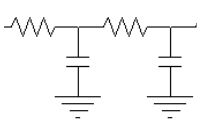
does not ignore conduction resistances through a thickness, but assumes that the surface temperature is uniform. Analytical methods even for simple geometry are complex, and numerical solutions tend to be more favourable. Numerical finite-difference methods using conduction theory are generally employed to solve heat transfer problems in multiple dimensions; but as pointed out in Holman [52], equivalent circuit theory along with finite-difference methods yields similar results. This allows for extensive RC thermal networks to be solved without having to deal with a set of complex differential equations.

The boundary conditions of such a system are defined using heat and temperature sources. Heat sources/sinks are represented by current sources; for example, the heating of a resistive component on an electrical circuit board could be modelled using a current source. Boundary conditions where the temperature is defined, are represented by voltage sources; these generally represent the temperature of an infinite sink/source such as the ambient temperature outside of a building, and are adequately modelled by an ideal voltage source. The initial conditions of the system are defined by the starting voltage or temperature of the capacitors in the thermal equivalent circuit.

Thermal networks have been used for modelling the heat transfer of buildings since the 1970's [53]. Simple building models have been developed using a single resistor/capacitor (RC) pair per component [54]–[56]; this configuration will be referred to as the L shape. The RC parameters for this shape can be calculated based on material properties, and therefore have physical meaning. The main issue with the L configuration is the loss of transient accuracy as the wall construction becomes thicker or more complex [57]. As a result, more sophisticated element configurations have been explored, some of which are depicted in Table 3.2. The T and  $\Pi$  shaped elements retain the physical significance of the R and C values when derived analytically. As with the L shape, the T and  $\Pi$  configurations provide relatively poor accuracy during initial periods of the response ( $< 1\tau$ , or one time constant) when compared to higher order models [58]. The transient accuracy of a model can be

improved by increasing the number of simple elements (L or T) which represent a fraction of the total R and C values [57]–[60]. More complex elements such as the 2R2C, 3R2C, and 3R4C are also used to model thick or multi-layered walls. The R and C parameter values for these elements are generally determined numerically using a variety of optimization algorithms [55], [61]–[64]. The general procedure is to minimize the error between the simulation and experimental measurements.

Table 3.2 - RC element configurations used in building thermal modelling

	<u>2R1C (T shape)</u>	<u>1R2C (Π shape)</u>	<u>2R2C</u>	<u>3R2C</u>
				
<b>Ref.</b>	[53], [57]–[60]	[53], [58], [63]	[64]	[61]–[65]

Thermal networks are also widely employed in the thermal modelling of electronics. For example, Karagol and Bikdash [66] developed a thermal network model of a circuit board. Thermal resistance values were determined by running thermal simulations on a CAD model of the circuit board, and capacitances were calculated using material properties. Galloway and Shidore [67] used thermal networks to model complex traces on printed circuit boards. Other electronic components such as power supplies [68], inductors [69], and transformers [70] have been successfully modelled using thermal networks.

Ladder type thermal circuits are also used in thermal modelling of electronics [71]. Ladder models are divided into either Cauer or Foster structures which are shown in Figure 3.1. In the Cauer model, R and C values are physical quantities that are representative of the layers of material being modelled. Lumped capacitance is assumed and each node represents the temperature of a layer or component. The RC parameters of a Foster model are empirical and are determined by matching the network response to experiments [72]. Only the outer node voltages (as shown in Figure 3.1) have physical significance which limits the practicality of this type of model. Nevertheless, ladder models have been used to model transistors [72], [73] and circuit boards [71].

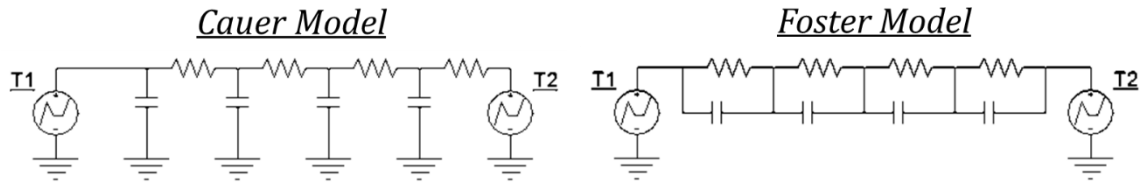


Figure 3.1 - Structural comparison between Cauer and Foster ladder models

The electric machines industry has undergone much development in the thermal modelling area in order to increase efficiency and extend operating ranges [74]. Many authors have used thermal networks, made up of either T or L shaped elements, for modelling different types of electric machines [75]–[82]. There is great focus on correctly modelling the motor windings since they are structurally complex, and calculating their thermal resistance analytically is not trivial. Internal losses which generate heat are represented by current sources and ambient temperatures by voltage sources. Convection and radiation heat transfer coefficients (i.e. external resistances) are generally determined through CFD analysis due to the complexity of air movement around the motors [38], [83]. These CFD obtained values for convection and radiation heat transfer are then implemented as resistances inside the thermal networks. The main motivation for using thermal networks rather than CAD models is to decrease simulation times and computational requirements.

### 3.3.2 Review of Battery Pack Modelling Using Thermal Equivalent Circuits

The most common use of thermal networks in battery system thermal modelling is a model for a single cell. The first step is quantifying the cell's heat generation at different operating conditions (SOC and temperature); this acts as the heat source in the thermal circuit model. Heat generation is usually determined from an electro-thermal model which considers electrochemical reactions inside the cell. A large number of papers are available which discuss the modelling of cell heat generation for different types of cell chemistries. This topic will not be discussed further since it does not pertain directly.

The most basic type of cell thermal network model is made up of a heat source (derived from a cell heat generation model), a cell at uniform temperature, and an external resistance which represents the cooling system [84], [85]. These models use forced air as the cooling method and can be employed to quickly estimate the cooling power requirements for small HEV packs.

The fully-lumped cell temperature assumption is limiting, and some authors have pointed out that knowledge of the internal cell temperature is more important than the surface condition [86], [87]. In practice however, the internal cell temperature is not accessible through non-intrusive means. As a result, partially lumped capacitance cell models (example shown in Figure 3.2) which include the thermal resistance of the cell have been developed [86]–[89].

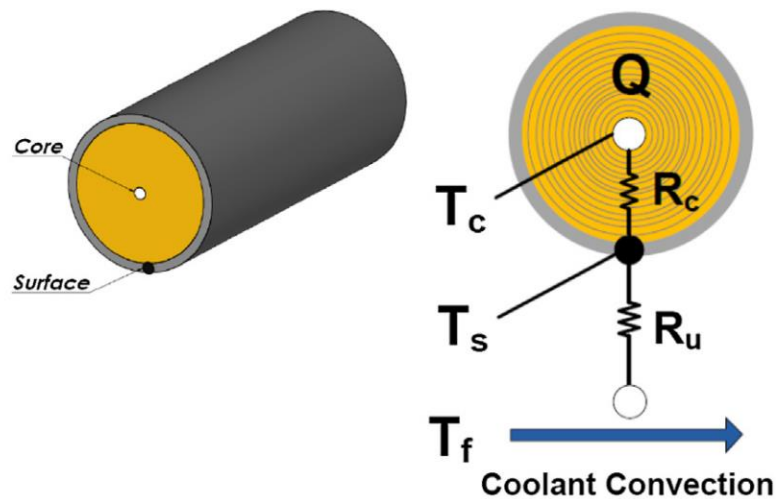


Figure 3.2 - Example of a two-resistor thermal model of a cylindrical cell [88]

The benefit to these models is the estimation of the cell's core temperature based on surface temperature measurement. References [86]–[88] used optimization algorithms to extract their RC parameter values by curve fitting simulation responses to experiments/FEA simulations. Forgez et al. [89] experimentally determined the cooling resistance and the cell's thermal resistance using the steady-state cell heat generation (estimated from a separate model), ambient temperature, and cell surface temperature. The thermal capacitance of the battery was determined by curve fitting

the model's response to the measured surface temperature. Greco et al. [35] developed a similar type of model for prismatic cells. Rather than using forced air convection, the cells were cooled by a heat pipe, which is more applicable to liquid cooled battery packs.

The next logical step is to extend the functionality by expanding the model to encompass multiple cells in the form of modules or a full battery pack [90]. Depending on the structural layout of the battery pack, interactions between cells or the effects of cell arrangements need to be considered. Smith et al. [91] modelled a set of 16 cylindrical cells that were tightly packaged together and exposed to air convection. A thermal circuit was structured to consider the interaction between cells, as well as the effects of positive temperature coefficient (PTC) current limiters installed at the top of each cell. CFD was used to extract the resistance values including the airflow around the module. The capacitance value of the PTC limiter had to be slightly modified from the material property derived value in order to improve transient response. Hu et al. [39] took a different approach and used a Foster network to model an air-cooled module made up of six cylindrical cells. CFD was used to extract the RC parameters, and the thermal network results were in agreement with their CFD simulations. The main drawback to a Foster network is that the RC parameters have to be re-extracted for any design change, which cannot be done quickly.

Thus far, the effects of the battery pack enclosure have been ignored. Damay et al. [92] developed a comprehensive thermal network model of a module made up of large prismatic cells tightly packaged together. The cells are cooled from the bottom, and the module is surrounded by thick insulation. Figure 3.3 shows the cell model (left) and a simplified depiction of the external thermal resistances (right). RC parameters were primarily evaluated analytically, except for the cell thickness resistance ( $R_{i,x}$ ), cooling resistance ( $R_{e,base}$ ), and cell capacitance which were determined experimentally. Cell surface temperatures were predicted within 1 °C of their experiments. This may be slightly above some "errors" reported in other papers

discussed previously, but is still very close considering the aforementioned model more realistically resembles an actual commercial battery pack.

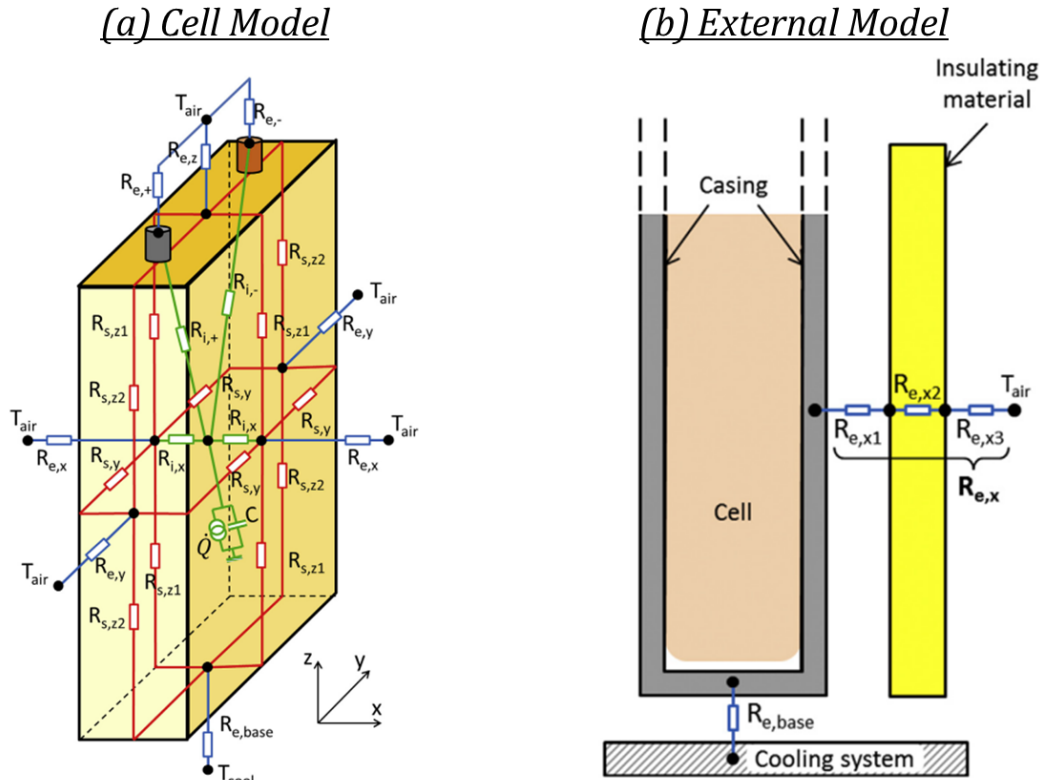


Figure 3.3 – (a) Complex cell thermal network, (b) external thermal model including cooling plate and insulated wall; adapted from [92]

Neubauer and Wood [93] utilized a thermal network model to represent a PHEV battery pack located inside the vehicle cabin. The model considered the effects of solar irradiance and ambient temperature on the cabin temperature. The battery pack however is considered as a single lumped mass at a uniform temperature. This thermal network model was used to carry out the analysis performed by Yuksel et al. [9], which has been discussed previously in Section 2.2.

The majority of thermal network models relating to battery packs are limited to cells or modules. The effects of battery pack construction and vehicle installation details are usually neglected, which as discussed in Section 2.2 play an important part in reducing the impact of energy inefficiency associated with challenging environmental conditions. The work in this thesis aims to extend the use of thermal networks to

account for battery pack constructions and realistic environmental exposure conditions such as road radiation and convection due to vehicle movement.

### **3.4 SUMMARY**

CAD modelling has the ability to accurately capture geometric detail and thermal interactions between components and their surroundings, at the cost of computational power and simulation time. As a result, their use in battery pack thermal modelling is generally limited to cell-level models. In the case of modelling full battery packs, the large model has to be simplified order to even be rendered solvable on a modern computer. Simulations of sub-models containing individual components and smaller assemblies are condensed and used as inputs in the scaled-up full pack model [5], [29] in order to entail solutions to the whole problem.

Thermal circuit simulation models on the other hand require little computational power and can be solved faster than in real time. This method is commonly utilized in cell-level models, with the advantages of quickly predicting cell temperatures and subsequent embedment of process controls. Simpler network models of entire battery packs have been developed, mainly for HEVs, but a battery pack's dynamic environmental exposure is generally overlooked, leaving the predictions incomplete.

The thermal network modelling method is the approach that best suits the needs of this project. The fast simulation time allows for easy implementation with the Autonomie powertrain model which functions on a time-step basis. This benefit also opens up the possibility of using the network model for predictive control purposes in the future, and long heat-soak (several days) studies can be conducted in the matter of minutes, allowing for the impact of daily temperature fluctuations on the battery pack to be examined in conjunction with drive cycles. The main drawback to this method is the difficulty of modelling 3-dimensional geometries and environmental effects, which both require some simplification.

For this project, a thermal network with physically meaningful R and C values was desired in order to facilitate design changes. These RC parameters were derived and verified experimentally in this work, but can also be generated using FE and CFD simulations in a similar manner. The latter approach is recommended for a new design in conceptual development, prior to the existence of full scale prototypes. Being able to embed a thermal model into a BTMS control system can benefit the overall vehicle energy efficiency. In order to run predictive controls, a simple yet accurate dynamic model is required. The faster than real-time solving capability of a thermal network suits the requirement for this type of control scheme. It is something that cannot be achieved using a CAD model.

Based on this literature review and trade-off analysis, the use of a thermal network to simulate a full battery pack and its dynamic environment was deemed to be the most suitable method for meeting the goals of this project.

## 4 EXPERIMENTAL METHODS

---

This chapter explains the process of developing a dynamic thermal network which describes the heat transfer between the battery modules and the environment for an EREV battery pack. A series of experiments were conducted in a laboratory setting on a full battery pack. Temperature and heat flux measurements were used to define a thermal network, and to calculate the required thermal resistances. The completed lab thermal network model is presented at the end of this chapter and verified using measurements taken during the experiments.

### 4.1 OVERVIEW

#### 4.1.1 Goals for the Lab Model

The model discussed in this chapter is limited to the exterior portion of the cells and modules of an electrically-dormant EREV battery pack. This is described in more detail below. The goals for this model are as follows:

- To accurately predict component temperatures and their rates of heat flow during transient and steady-state periods
- Be adaptable to dynamic conditions such as:
  - Ambient air temperature
  - Cooling/heating system temperature
- Easily modifiable to quickly apply and assess the impact of physical design changes

#### 4.1.2 Battery Pack Description

A full-sized, liquid-cooled EREV battery pack (shown in Figure 4.1) was the object of testing in the laboratory and is the basis for the thermal model developed. The pack consists of 288 cells divided into four modules (front, middle, rear left and rear right). The cells are constrained by interlocking plastic frames which are clamped down to a

metal baseplate. A parallel cooling method is utilized in this BTMS and functions as follows: water/ethylene glycol mix (50/50) enters through the inlet port into a distribution manifold, then flows through cooling plates into a collection manifold and out the pack. A cooling plate is sandwiched between every second cell; therefore each cell has one face in contact with a heat exchanger (cooling) plate.



Figure 4.1 - Lab EREV battery pack

This is a production battery pack that has all of the plumbing and electrical hardware needed to be fully operational. This makes fluid circulation and charging/discharging possible with the necessary equipment (fluid pump and large battery cycler).

Performing thermal testing on a standalone battery pack allows most of the vehicle's effects to be eliminated, thus the interactions inside the pack can be investigated in greater detail. Situating the battery pack in a laboratory setting also allows most environmental fluctuations to be minimized; therefore the pack is primarily affected by variations in the lab's HVAC. The testing performed in the lab involves heating the pack from the inside by circulating warm fluid (details in section 4.2.1). This helps create a state of unidirectional heat flow that originates from inside the cooling plates and propagates out to the environment. The approach facilitates heat path determination and thermal resistance measurements.

### 4.1.3 Original Model

Figure 4.2 depicts the original thermal network that was developed by others in the research group prior to the experimental work in this thesis. This model was developed analytically with many assumptions made. The purpose of the experiments was to investigate and improve the paths outlined in this circuit and to provide validation data. An in-depth discussion about the layout and meaning of the components in this thermal network can be found in reference [6].

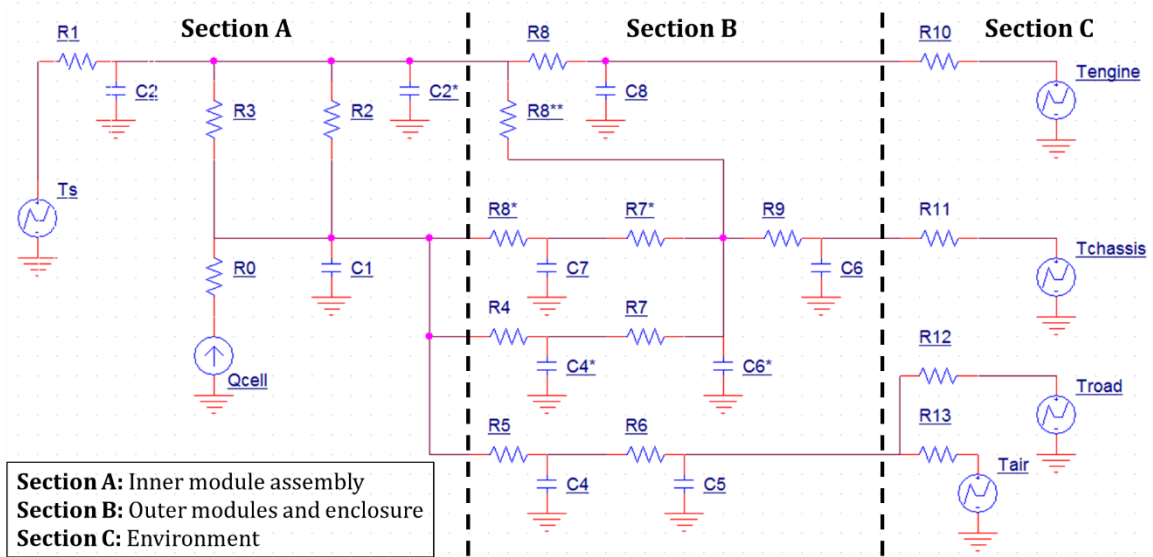


Figure 4.2 - Original thermal network

The original thermal network is meant to represent the battery pack as installed on a vehicle. This includes six input sources that represent the coolant temperature ( $T_s$ ), cell internal heat generation ( $Q_{cell}$ ), heating from the engine ( $T_{engine}$ ), chassis effects ( $T_{chassis}$ ), underbody airflow ( $T_{air}$ ), and road radiation ( $T_{road}$ ). This model contains a network that represents the various heat paths inside the cell modules, outlined by “Section A”. Here, the heat transfer dynamics between the cooling plates, the cells, and their retention frames are modelled. The detailed modelling of “Section A” components constitutes the work being carried out by another student, as mentioned in Chapter 1.

“Section B” represents the components within the battery pack enclosure. This model indicates how heat flows between the frames, endplates ( $R8^*$ ), cover ( $R9$ ) and baseplate ( $R6$ ). In this model, the frame is split up into three parts: bottom ( $R5$ ), manifold ( $R3$ ), and top/sides ( $R4$ ). An airgap separates the frames and endplates from the cover ( $R7$ , and  $R7^*$ ). The bottom part of the frame is connected to the baseplate through  $R6$ , and the manifold connects to the front bulkhead through  $R8$ .

“Section C” represents the environment surrounding the enclosure which includes most of the sources.  $R10$  represents the resistance between the front bulkhead and the hot air surrounding the engine. The baseplate, which faces the road, is subjected to underbody air currents ( $R13$ ) and road radiation ( $R12$ ).

This overall thermal circuit provides the framework for the areas to be investigated. Illustrations of each component and their location are provided in later sections. The temperature nodes in the circuit on the previous page were used as guidelines for thermocouple placement, and heat flux sensors were positioned where resistance measurements were thought to be required. As the experimental runs progressed, nodes and resistor values were modified, and new ones were created based on the experimental observations.

## **4.2 MEASUREMENTS**

This section provides details on the experimental setup and methodology. The process of measuring the thermal characteristics is discussed and an uncertainty analysis is performed. A discussion pertaining to difficulties encountered during the measurement process is included as it can be useful for others attempting similar types of measurements. Everything in this section is related to the lab battery pack setup described in Section 4.1.2.

## 4.2.1 Experimental Setup

### 4.2.1.1 Equipment and Sensors

#### *Fluid Conditioning Cart*

In order to take thermal resistance measurements, a thermal steady-state has to be reached. This requires a constant heat source applied to the system under measurement for a sufficient period of time, and is achieved by circulating warm fluid through the pack. The fluid conditioning cart in Figure 4.3 (a) was already available in the lab as a part of an HVAC test bench system from Complex Engineering. The cart contains a rotary vane pump (capable of 22 Lpm) and a 6 kW fluid heater which were used to circulate warm fluid for this setup. A built-in Watlow temperature controller allows the user to define a fluid temperature set-point to the nearest °C and is capable of reaching the set-point in a relatively short amount of time with minimal overshoot. The fluid cart also utilizes a calibrated magnetic flowmeter and a PowerFlex AC drive controller for flow control of the pump. The flowrate can be varied to within 0.01 Lpm using digital controls, and can be monitored through multiple digital readouts that exist on the cart.

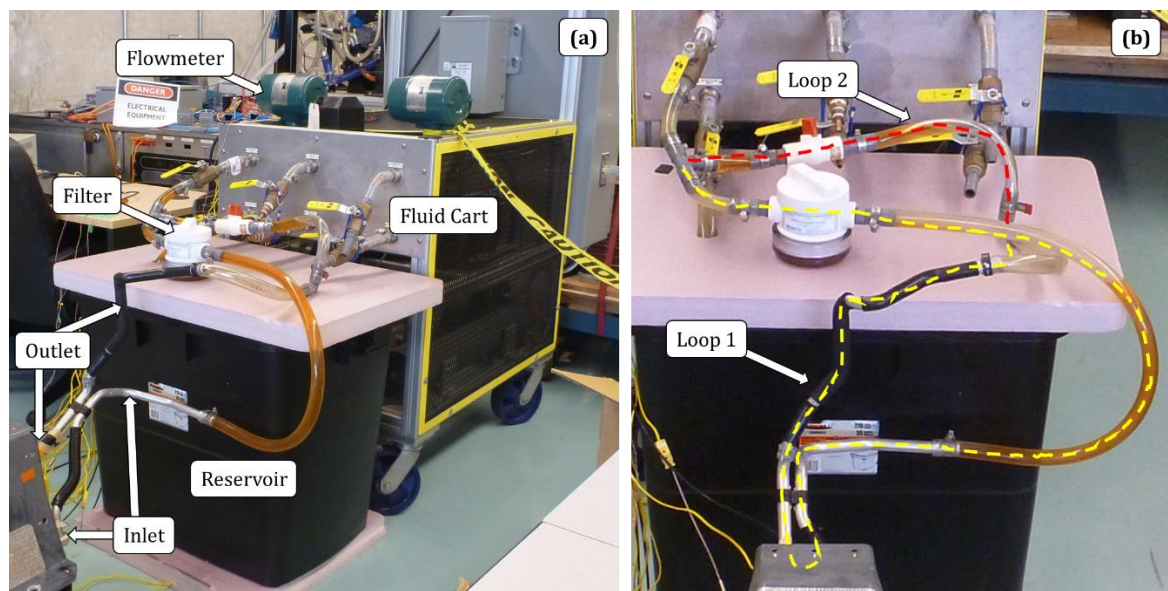


Figure 4.3 - Fluid conditioning cart setup (a) with outlined fluid loops: Loop 1 – pack circulation loop and Loop 2 – bypass loop (b)

For a given test, the fluid cart is set to a constant temperature and flowrate and warm fluid circulates through the battery pack for a period of several hours. This allows an equilibrium to be reached between the fluid inside the pack, and dissipation to the room. At steady-state, the heat being removed from the fluid source (heat into the system) must equal the heat flowing into the room (heat out of the system). By changing the fluid temperature and flowrate, different constant heat inputs can be achieved.

Figure 4.3 (b) depicts the two loops of the fluid reservoir designed to conduct the experiments. The fluid is a 50/50 mixture of water and ethylene glycol, also used in the production vehicle. The concentration of ethylene glycol was periodically measured using an ethylene glycol refractometer (Hanna HI 96831) and adjusted to 50% in order to keep the fluid properties constant over the testing duration.

Loop 1 is responsible for sending fluid through the battery pack. In this loop, the bypass valve is closed, and fluid is pushed through the filter and the battery pack. The inlet and outlet hoses are placed at opposite ends of the reservoir to prevent any bubbles from entering the system. The filter ensures that only clean fluid is flowing inside the pack, and fluid is pushed through the filter to minimize any foaming due to cavitation.

Loop 2 was created to provide a step input to the system in order to better evaluate the time constant of the battery pack due to sudden heating. Before every run, the bypass valve is opened and the valve on the filter is closed to prevent fluid from entering the battery pack. The pumping system is now in bypass mode. Fluid is circulated inside the reservoir and heated up until the desired temperature is reached, then Loop 1 is opened (Loop 2 is closed) and heated fluid flows through the battery pack.

A constant temperature input is needed in order to reduce the fluid conditioning cart's influence on the time response of the entire system. This is illustrated in Figure 4.4.

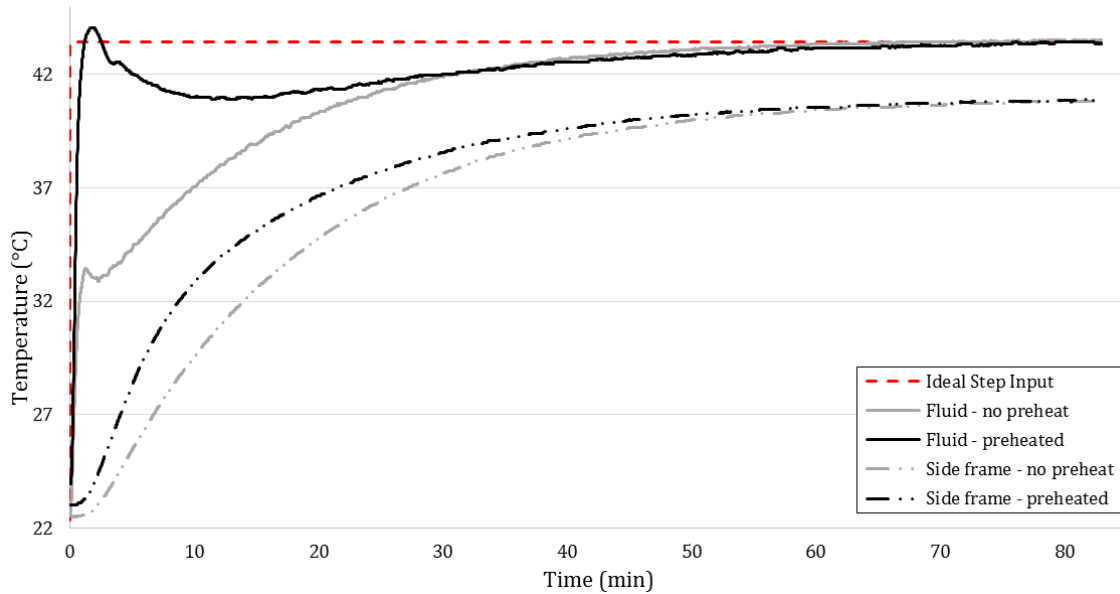


Figure 4.4 – Effect of a step fluid temperature input on system response; ideal input (red), preheat response (black), no preheat response (grey)

The grey lines show the temperature response of the inlet fluid and the side frame when Loop 2 (pre-heat) is not utilized. The black lines represent the same components when the fluid is preheated by activating Loop 2 before the start of the test. It is clear that preheating the fluid results in a more step-like input since virtually all the fluid is already up to temperature. A true step input could not be achieved since it would require a more powerful heater or a much greater volume of fluid. Even though the reservoir contains approximately 60 L water and ethylene glycol mixture, the thermal inertia of the fluid reservoir is too low to remain fully heated after the cooled fluid emerging from the pack begins to mix in. For all practical purposes, this was still deemed close enough to a step input. A comparison of the side frame response to the both inputs is also shown in Figure 4.4. The run using the preheated fluid shows a faster rise time naturally. The use of a step input proves important when comparing simulation results to the experiments for validation.

### ***Data Acquisition System***

The data acquisition system (DAQ) used for all the experiments consists of multiple IPETRONIK measurement modules communicating with a standalone laptop through

IPETRONIK's IPEmotion software. Two types of measurement modules were used: M-SENS 8 modules for voltage measurement, and M-THERMO K16 modules for thermocouple temperatures. A module rack containing two M-SENS and two M-THERMO blocks was used, allowing for 16 voltage and 32 thermocouple inputs.

The M-SENS blocks use 16 bit analog-to-digital conversion with selectable voltage input ranges from 0.1 – 100 V, and variable sensor excitation voltages (0 – 15 V). The input range and excitation of each channel was appropriately selected to match its respective sensor's output level. High quality, shielded cables were utilized to minimize the amount of noise pickup.

The M-THERMO blocks have integrated miniature female K-type thermocouple input connections, and four internal resistance temperature detectors (RTD) for built-in cold-junction compensation. The block achieves a resolution of 0.087 °C with an accuracy of  $\pm 0.035$  % of the full temperature range of -60 – 1000 °C (0.371 °C). A sample rate of 1 Hz was utilized for all measurements since larger thermal systems react rather slowly and using higher rates would result in unnecessarily large data files.

### ***Flowrate and Pressure Drop***

The pressure drop across the fluid ports on the battery pack was monitored for pumping requirement purposes using an Omega PX26 Series differential pressure transducer with a range of 0 – 15 psi. The pressure transducer was installed between the inlet and outlet ports of the battery pack as shown in Figure 4.5 and produces a voltage output proportional to its input voltage with an accuracy of 1.0 % of full scale (0.15 psi).

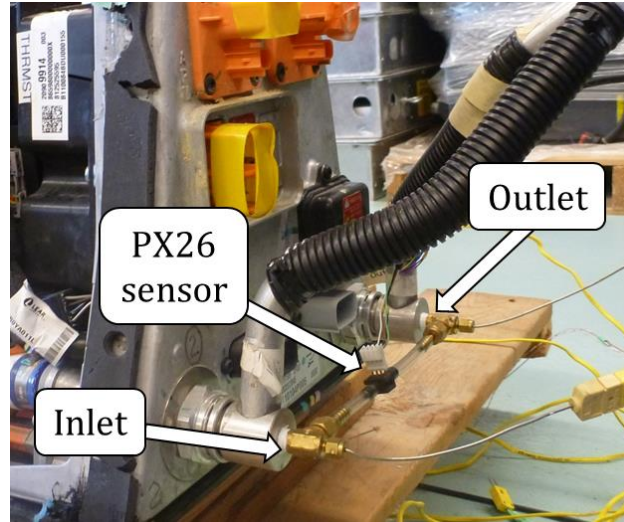


Figure 4.5 - Fluid port temperature and pressure drop measurement

The output of the magnetic flowmeter was monitored to record the fluid flowrate during the test runs. The digital meter readout and measured output were periodically cross-checked to ensure the correct flowrate was being recorded.

### ***Internal Temperature Sensors***

To get an idea of what the vehicle would read as cell temperatures, some of the internal temperature sensors (thermistors) were monitored by tapping into the onboard BMS boards located atop the cell modules. A wiring schematic from the vehicle service manual was studied to determine the location and wiring for each sensor. A calibration run was previously performed on such a sensor outside of the battery pack, taken from a dismantled cell module. The calibration consists of measuring the sensor's resistance over a range of known temperatures (measured by a reference thermocouple). The Steinhart-Hart model was used to convert sensor resistance ( $R$ ) to temperature ( $T$ ) as shown in Equation (4.1) [94].

$$\frac{1}{T} = A + B \ln R + C (\ln R)^2 \quad (4.1)$$

Applying three calibration points ( $T, R$ ) that span the desired operating range of the sensor ( $\sim 20$ - $50$  °C in this case) to Equation (4.1) yields a 3-by-3 system of equations

that can be solved to produce the coefficients  $A$ ,  $B$ , and  $C$ . In practice, a standard voltage divider method was employed to determine the sensor's resistance, and the corresponding temperature was extracted from the Steinhart-Hart equation.

### ***Thermocouples***

Omega K-type thermocouples and connectors were employed for temperature measurement since a large number of them were already available, along with a reliable DAQ (IPETRONIK system). The standard limits of error for these thermocouples are 2.2 °C for temperatures under 293 °C. Methods of further quantifying uncertainty are presented subsequently in Section 4.2.1.2.

Stainless steel sheathed thermocouple probes were inserted into the inlet and outlet ports of the battery pack as visible in Figure 4.5. Surface temperatures were measured using PVC insulated thermocouple wire. To ensure surface measurement accuracy, the thermocouples were placed on their flat side with as much length as possible in contact with the surface. Figure 4.6 shows the mounting method in use on multiple sensors placed inside the cover. A layer of thermally conductive 3M 8810 double-sided tape with approximate dimensions of 7 x 1 cm was placed on the surface under the thermocouple. The tape has a thermal conductivity of 0.6 W/m\*K which provides good thermal contact between the surface and the sensor. Another small piece of thermal tape was put over the thermocouple bead bridging to the bottom piece of tape for better heat transfer around the tip. A longer piece of polyester tape (Airtech Flashbreaker 1) was used to secure the thermocouple in place and to provide an insulating layer to better capture the surface temperature of interest. Polyester tape was much more effective at keeping the sensors in place than electrical tape, especially at warmer temperatures. Small pieces of electrical tape were used to keep the rest of the thermocouple wire from moving. This mounting method allowed for consistency which is important for reducing measurement errors.



Figure 4.6 - Thermocouple mounting method

### ***Heat Flux Sensors***

Heat flux  $\{W/m^2\}$  was measured using Omega HFS-4 heat flux sensors (Figure 4.7). These are thin-film (0.18 mm thick) thermoelectric-type sensors that generate a voltage proportional to the temperature difference across their thickness. The minute temperature differential is captured and amplified by the thermopile (many thermocouples in series). The junctions themselves are visible in the magnified portion of Figure 4.7 as the location on a trace where the color switches from dark to light (circled).

In construction, metal traces of the two thermoelectric junction materials are deposited on a very thin carrier film in a regular pattern. This film is then interwoven between somewhat thicker narrow strips of Kapton such that successive junctions are positioned alternately above and below the sensor mid-plane. This assembly is laminated together, with the glue line (fracture line) as the weakest spot, depicted in Figure 4.7. The sensor is very pliable along these lines, thus easily subjecting the deposited metal traces to fracture in this region; so peeling a mounted sensor along the stiffer direction is highly recommended to minimize damage. The figure also shows the integrated K-type thermocouple, which conveniently uses the same cold junction compensation as the rest of the stand-alone K-type thermocouples used for data acquisition.

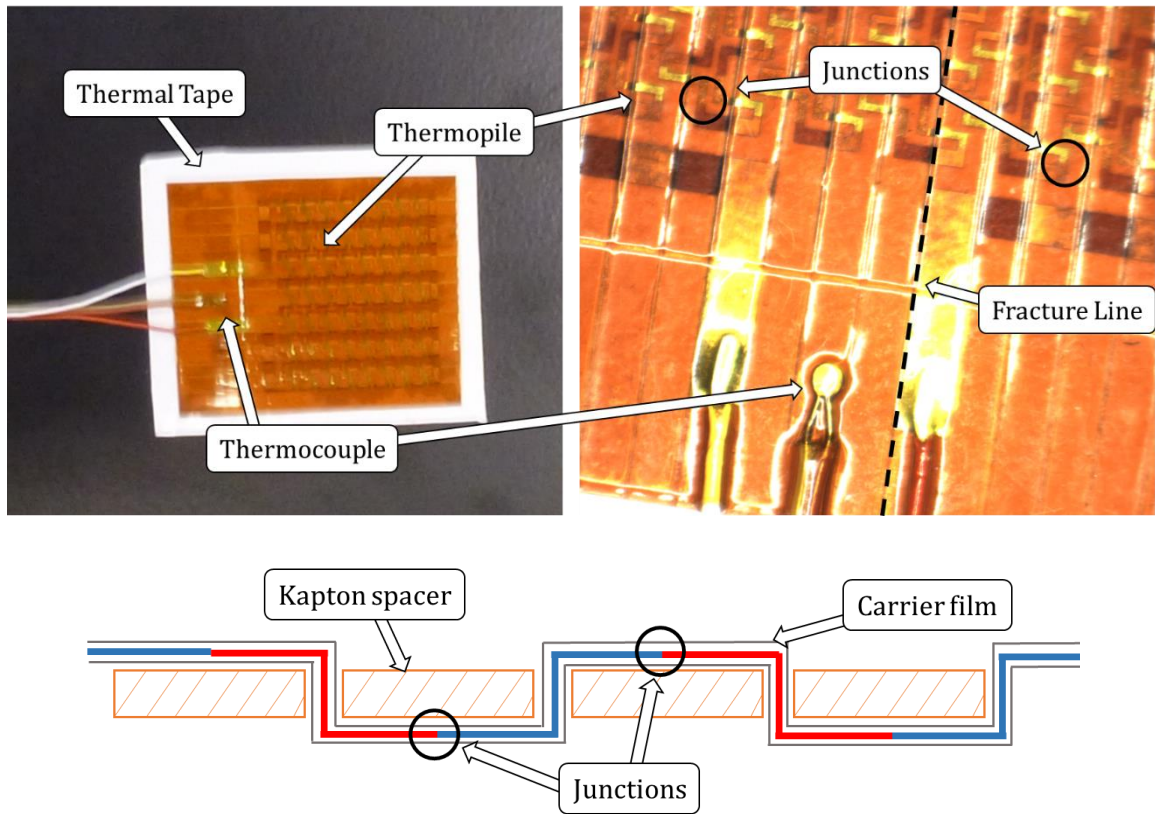


Figure 4.7 - Omega HFS-4 heat flux sensor

The signal level of these sensors is in the  $\mu\text{V}$  range but by scaling the M-SENS input channels to  $\pm 0.1\text{ V}$ , a  $3\ \mu\text{V/bit}$  resolution is achieved. Each individual sensor has a calibration coefficient provided by Omega of approximately  $2\ \mu\text{V}/(\text{W}/\text{m}^2)$  which translates to a heat flux resolution of  $1.5\ (\text{W}/\text{m}^2)/\text{bit}$ .

To ensure accurate heat flux measurement, the sensor must not interfere with the surface being measured. To keep the thermal resistance of the sensor minimal, the same thermally conductive tape was stuck on the surface and the heat flux sensor placed on top. This was found to be the most effective and reliable method. Simply taping the sensor to a surface usually resulted in an airgap forming under the sensor which reduced the sensor's output. Using a thermally conductive paste can remove the airgap but the reading is directly affected by the thickness of the paste; this is not practical nor consistent when multiple sensors are being used. The thermal tape method makes the sensors removable but great care must be taken to not bend them

excessively as they are extremely fragile. Several were broken during the experimentation process which required their performance to be monitored closely.

#### ***4.2.1.2 Uncertainty Analysis on Direct Measurements***

It is important to quantify the level of uncertainty present in a measurement in order to establish the level of “trust” that can be put into such a measurement. It is often the case where a measurement is assumed to be “true”, when in reality many factors affect the accuracy of the measurement. This section describes the method used for estimating the uncertainty present in the primary measurements (e.g., temperature and heat flux). The propagation of uncertainty is discussed subsequently in Section 4.2.2. The uncertainty analyses carried out are based on the procedures outlined by Moffat [95] and NASA [96].

#### ***Methodology***

A direct, or primary, measurement is obtained directly from a sensor’s output, such as a temperature reading from a thermocouple. In general, a measurement has two types of uncertainty (or error): fixed and random. The fixed error, often referred to as bias, is usually a constant offset from the true value and is defined by the manufacturer of the sensor. For example, if a temperature sensor is said to have an accuracy of  $\pm 0.25$  °C, the fixed error would be 0.25 °C. The bias can also be given as a percentage of the full operating range of the sensor (% fs). The random error, or precision index, is related to its standard deviation and is dependent on signal noise caused by factors such as changing test conditions, power spikes, and electrical interference.

In this work, a multiple-sample measurement method is used. Many readings are recorded during a single test and the mean value is used as the final measurement. The level of random error in the measurement decreases as the number or sample points increases since the fluctuations average out closer to the true mean of the signal. The following list outlines the measures taken to reduce the level of random error in the measurements:

- Switching power supplies were moved away from the test area
- Shielded cable was used where possible
- DAQ sample rate was reduced to 1 Hz to reduce its influence on the signal noise
- Test area was partially fenced/boarded off to prevent large-scale convection currents from fans and HVAC
- Measurement recording time was at least 30 min (>1800 sample points)

### ***Analysis***

The bias of a primary measurement,  $B_M$ , can be found by taking the root sum of squares (RSS) of the bias of each component in the measurement system, where  $n$  is the number of components in the measurement system.

$$B_M = \sqrt{\sum_{i=1}^n B_i^2} \quad (4.2)$$

The precision index,  $S_M$ , is the standard deviation of the mean of the measurement sample, which is calculated using Equation (4.3). The standard deviation of the measurement sample,  $S_i$ , is calculated using Equation (4.4);  $N$  is the number of measurement points,  $X_i$  represents each individual reading, and  $\bar{X}$  is the mean of the sample set.

$$S_M = \frac{S_i}{\sqrt{N}} \quad (4.3)$$

$$S_i = \sqrt{\sum_{i=1}^N \frac{(X_i - \bar{X})^2}{N - 1}} \quad (4.4)$$

$S_i$  physically represents the noise level of the measurement signal, whereas  $S_M$  represents the deviation of the measurement sample mean from the population (true) mean. As the number of sample points ( $N$ ) increases, the sample mean approaches the true mean, and the random error tends to zero.

The total uncertainty,  $U_M$ , is the root sum of squares (RSS) of the bias and precision index of the measurement. The Student's t-distribution  $t$  value for  $N-1$  degrees of freedom is used to relate the sample mean deviation to the population mean. The measured value would then be stated as  $M = X \pm U_M$ .

$$U_M = \sqrt{B_M^2 + (tS_M)^2} \quad (4.5)$$

### ***Sample Calculation***

The following section shows how the uncertainty is determined for a particular temperature measurement from a thermocouple. The first step is to assess the signal chain and interpret manufacturer data to find the bias of each individual component of the measuring system. The measurement system in this case consists of two parts: the thermocouple, and the DAQ.

The accuracy of the K-type thermocouple is given as 2.2 °C, which can be interpreted as  $\pm 1.1$  °C. The DAQ has an accuracy  $\pm 0.035$  % fs, which translates to  $\pm 0.371$  °C. From Equation (4.2), the total fixed error is:

$$B_M = \sqrt{B_{DAQ}^2 + B_{thermocouple}^2} = \sqrt{(0.371 \text{ } ^\circ\text{C})^2 + (1.1 \text{ } ^\circ\text{C})^2}$$

$$\therefore \mathbf{B_M = 1.16 \text{ } ^\circ\text{C}}$$

The precision error is found by calculating the sample standard deviation of the measurement period. The sample measurement being examined has a mean of 38.43 °C, with a sample standard deviation of 0.05994 °C over a period of 3303 measurement points. Equation (4.3) yields:

$$S_M = \frac{0.05994 \text{ } ^\circ\text{C}}{\sqrt{3303}} = \mathbf{0.001044 \text{ } ^\circ\text{C}}$$

For 3302 data points, the t-value is 1.96. The total uncertainty on the thermocouple measurement is thus:

$$U_M = \sqrt{(1.16 \text{ }^\circ\text{C})^2 + (1.96 * 0.001044 \text{ }^\circ\text{C})^2} = \mathbf{1.16 \text{ }^\circ\text{C}}$$

The temperature measurement can now be stated as  $T = 38.43 \pm 1.2 \text{ }^\circ\text{C}$ . The uncertainty is written using the same number of significant figures as stated in the manufacturer’s specification (1.2 °C instead of 1.16 °C). Because of the large sample set, the random error is virtually eliminated and the total uncertainty is approximately equal to the bias of the measurement system. This procedure was followed for all the direct measurements taken and the results are presented in Table 4.1. The bit resolution of each type of measurement is included for reference and comparison. The “total certainty” values in this table are used to evaluate the propagation of uncertainty through compound measurements, which will serve as a guideline for refining the thermal model in Section 5.2.3.

Table 4.1 - Direct measurement uncertainties with bit resolution

<b>Direct Measurement</b>	<b>Total Uncertainty</b>	<b>Bit Resolution</b>
Pressure	0.036 psi	0.0092 psi
Flowrate	0.045 Lpm	0.0113 Lpm
Temperature	1.2 °C	0.087 °C
Heat flux	3.0 W/m <sup>2</sup>	1.5 W/m <sup>2</sup>
Temperature difference	0.11 °C	0.1097 °C

#### **4.2.1.3 Test Method and Procedure**

The main goal for these experiments is to thermally characterize the battery pack in order to help build a thermal network that better represents the system. This is achieved by mapping out the thermal interactions between all the components in the battery pack using temperature and heat flux measurements. The measurement points are used for validating the thermal network simulation during transient and steady-state periods.

### ***Testing Method***

The general procedure is to provide a constant fluid temperature and flowrate input to the battery pack while taking temperature and heat flux measurements at points of interest. The fluid temperatures set-points were 30, 37, 45, 50, and 55 °C. The lower limit of 30 °C is closest to the fluid temperature that would normally be circulated in the vehicle, but due to the small temperature difference between the fluid and lab ambient air, the quality of measurement declines due to a lower signal-to-noise ratio on both the thermocouples and heat flux sensors. The upper experimental temperature was limited to 55 °C to mitigate ageing damage to the cells. The runs at this temperature provide a high signal-to-noise ratio and are considered to be the most reliable of the measurements. The initial temperature increments were of 5 °C but the fluid temperatures of 35 and 40 °C were merged into one run at 37 °C to reduce the amount of testing time.

The flowrates utilized were 3, 6, 9, and 10 Lpm. 3 Lpm was the lowest flowrate at which the fluid cart could properly control the temperature of the fluid. The upper limit was chosen to mimic the maximum flowrate commensurate with a vehicle installed and operating pack.

Due to the limited number of heat flux sensors available (4 for most experiments), eight sets of tests were conducted in order to measure every component. Specific paths/interactions were chosen for investigation in each set of tests, and observed at each temperature and flowrate. Some components were measured multiple times to verify reproducibility and to provide relatable reference points between tests.

The general test procedure was as follows:

- Set desired temperature set-point on the fluid bench
- Close loop 1 and open loop 2 (bypass mode)
- Start pump and wait for the reservoir temperature to reach the set-point
- Turn off pump and start recording in IPEmotion

- Close loop 2 and open loop 1
- Start pump and set it to the desired flowrate
- Wait until the system has been at steady-state for at least 30 minutes
- Turn off the pump
- Let the battery pack cool down to room temperature and stop recording data

Figure 4.8 shows a typical test run displayed in IPEmotion. The run shown was for a fluid temperature set-point of 50 °C at 9 Lpm. The inlet fluid does not fully reach the set-point but rather sits approximately 1 °C below, (49 °C in this case). This offset is consistent for the other set-points but is of no real importance. The tests can be divided into three time periods: heating, steady-state, and cooling. The heating period is the initial transient portion where the battery is absorbing heat from the fluid. The steady-state period (sectioned off by vertical lines) is determined when all of the temperatures are no longer increasing. The thermal resistance measurement period now begins and the test is continued for at least 30 minutes (to increase the number of measurement points and reduce the effects of random error).

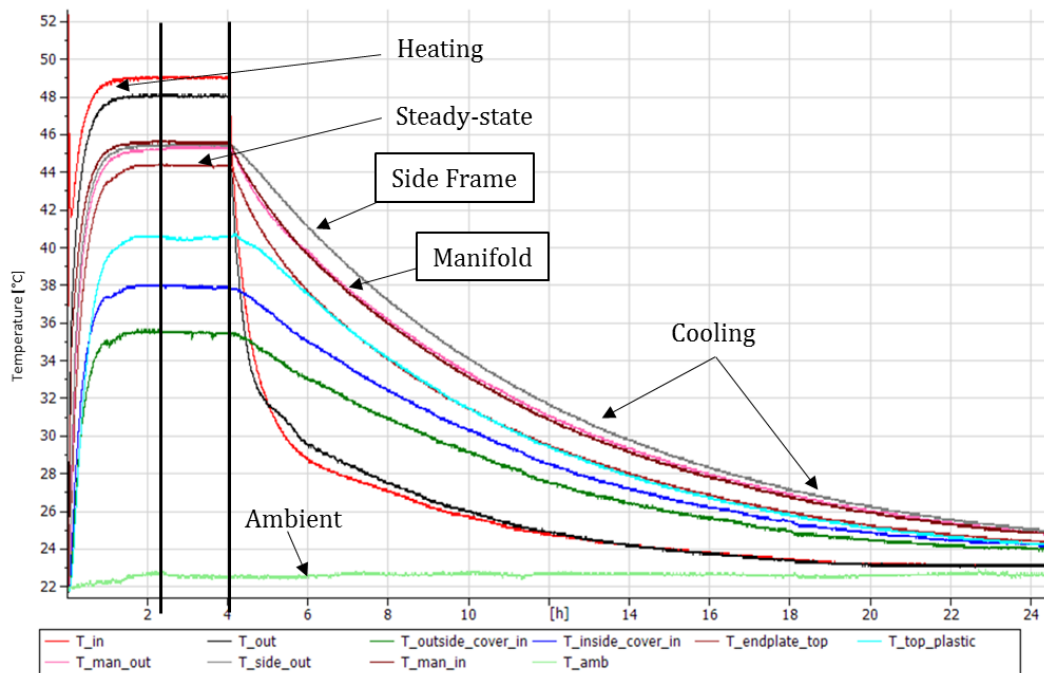


Figure 4.8 - Typical heating and cooling response: Temperature (°C) vs Time (h)

Once the system has been at steady-state for long enough, the pump is shut off and the cooling process begins. Due to the battery pack's large thermal mass, it takes over a day to cool down to room temperature. The test shown in Figure 4.8 did not reach room temperature for the first 20 hours of cooling. Before starting a new test, the entire pack should be at a uniform temperature to ensure consistency in the results.

The cooling portion of the curve can be used to assess the degree of isolation of each component from the environment. In Figure 4.8 for example, the side frame (grey) and the manifolds (pink) are at the same steady-state temperature but the manifolds show a faster cooling rate. This indicates that there is greater heat leakage from the manifolds to the environment.

### ***Assumptions***

The following assumptions are made to simplify the experiments and data analysis:

- **Fluid temperature input is constant:** while not a perfect step input, the beginning portion of the fluid temperature input averages close to the steady-state value. This is the closest to a step input that could be achieved in practicality.
- **Environmental conditions are constant:** the ambient conditions of the laboratory represent the environment. The room temperature is assumed to be constant throughout a single test (~24 hour period). The change in temperature usually fluctuates within 0.5 °C during the test period. Air currents are generally minimal but variations do occur sometimes when the ventilation system turns on and off.
- **Front module is representative of the entire pack:** the battery pack TMS is designed to provide even cooling for all cells. The middle of the front module was chosen to be measured due to its high accessibility and ease of sensor placement. Preliminary tests (Figure 4.9) have shown that there is no practical difference in temperature (~0.1 °C) or heat flux (~4 W/m<sup>2</sup>) between the front, middle, and rear modules.

- **Thermal resistances are constant:** this applies to the majority of the resistors in the thermal network which are conductive in nature. The external resistances are affected by convection and radiation which are temperature dependent. For simplicity it is assumed that these do not vary significantly during normal operating conditions.

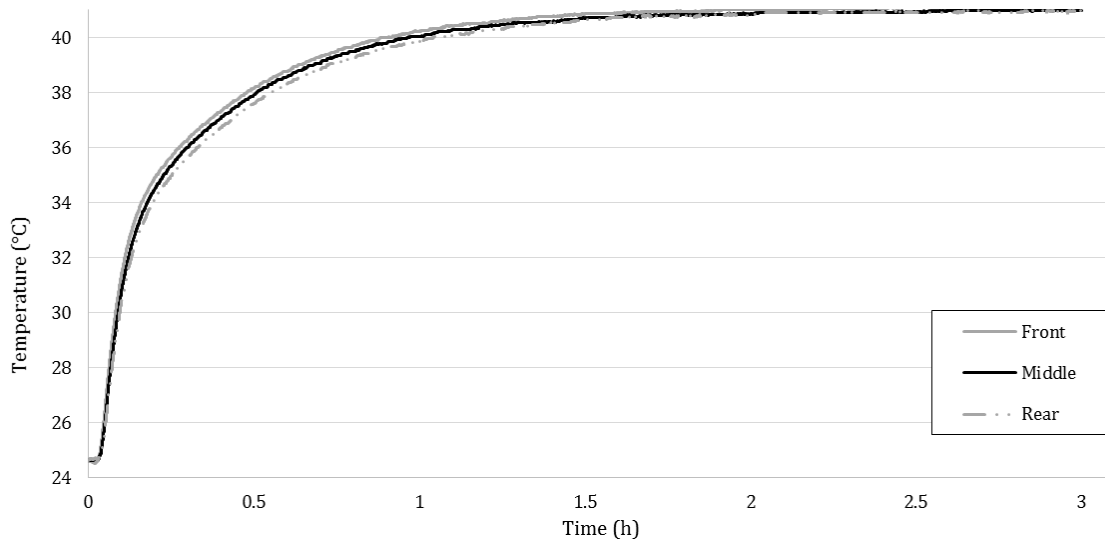


Figure 4.9 - Spatial difference in manifold temperature

For example, Figure 4.9 shows the variation in manifold temperature between the front and the rear. The steady-state values differ by only 0.1 °C. Due to the construction of the pack, the transient response is slightly different. This is caused by heat being lost in the manifold as the fluid is sent to the rear of the pack. The heat flux behaves in a similar manner since it is related to the temperature of the surface. The same trend is also exhibited by the side frame and baseplate. The small number of heat flux sensors available made it practical to only take one module's measurements as representative of the pack average.

#### 4.2.2 Thermal Resistance Measurement

The procedure outlined in the previous section was followed to create conditions suitable for thermal resistance measurements. This section describes the methodology behind these measurements, and an uncertainty analysis on the

resistance measurements is performed. An example is given to help illustrate the process.

### ***Methodology***

Thermal resistance measurements are taken to determine the resistor values to be used in the thermal network simulation. To measure a thermal resistance, a temperature differential ( $\Delta T$ ) and the rate of heat flow that it causes ( $\dot{Q}$ ) must be known.  $\Delta T$  is measured by installing a thermocouple on each side of the 'resistor' which could represent the thickness of a component or a gap between two objects. The rate of heat flow (in W) is not directly measurable and is calculated using the heat flux ( $\dot{q}$ ) and surface area ( $A_s$ ) as follows:

$$\dot{Q} = \dot{q}A_s \quad (4.6)$$

The heat flux is measured by the HFS-4 sensor and the surface area is physically measured as accurately as possible. All of the components in the thermal network are scaled down to a per-cell contribution, since the cell is the most important component in the ESS and is the increment in any battery pack design. In the thermal sense, there are 288 cells in parallel, flowing out heat, even though the cells are electrically wired in a 3P-96S configuration. To simplify the resultant circuit, equivalent series and parallel resistors were created to represent individual components in the assembly. An example would be the addition of the inlet and outlet manifolds. Due to symmetry, these components are added as parallel resistors, resulting in a single manifold resistance. This method lowers the complexity of the thermal network while remaining true to the original system. In a similar manner, resistors that appear in series (like a sequential stack of materials and gaps between them) can be summed up to get an equivalent resistor. Additionally, the circuit values are the average of the individual measurements taken over the entire range of testing conditions (temperature and flowrate).

### *Assumptions*

- **Surface temperature and heat flux are uniform:** the instrumentation is not sensitive enough to detect small variations in surface temperature. Components are divided locally into 'lumped' thermal masses which have surfaces uniform in temperature.
- **Heat flows primarily in one direction:** the experiment is designed for heat to flow from the cooling plates outward to the environment.
- **Average fluid temperature inside cooling plate:** the temperature of the fluid inside the cooling plates is assumed to be at the arithmetic-mean temperature of the inlet and outlet.

### *Sample procedure*

The side frame path will be used as an example to help visualize the process (other paths are discussed in more detail later). The cell and frame assembly shown in Figure 4.10 is separated into the following six parts: 1) top, 2) inlet side, 3) outlet side, 4) inlet manifold, 5) outlet manifold, and 6) bottom. The frame is symmetrical about its centre which allows for the inlet and outlet sides and manifolds to be combined into single equivalent resistances.

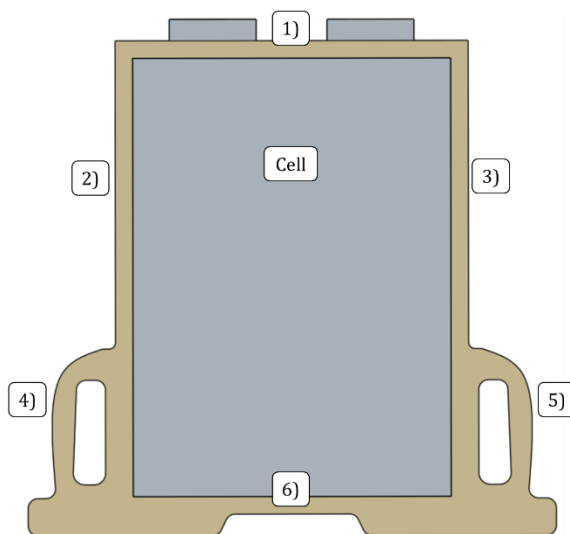


Figure 4.10 - Cell frame schematic, showing separate heat flow paths

Heat originates in the centre and flows out radially through the frames. Figure 4.11 illustrates the physical measurements points (red circles) and resistances (black rectangles). The inlet and outlet side frame resistances are depicted as  $R_1$  and  $R_2$ , respectively. There is also an airgap between the side frame and cover denoted as  $R_3$  and  $R_4$  at both sides. A heat flux sensor is placed on the surface of the side frames ( $\dot{q}_1$ ,  $\dot{q}_2$ ,  $T_1$ , and  $T_2$ ) and thermocouples are placed on the inside of the cover ( $T_3$  and  $T_4$ ) at the same height as the heat flux sensors. The inside temperature,  $T_{avg}$ , is approximated as the mean fluid temperature between inlet and outlet. In reality, heat transfer through the heat exchanger (i.e. cooling plate) varies along the length of the cooling channels, and the fluid at the centre of the cooling plate is at the log-mean temperature rather than the arithmetic-mean temperature. Calculating the log-mean fluid temperature requires knowledge of the cell surface temperature, which in this case is unknown. However, due to the small temperature difference between inlet and outlet fluid, the variation between log-mean and arithmetic-mean temperature is insignificant (hundredths of 1 °C). This justifies the use of the arithmetic mean fluid temperature as the proxy for fluid temperature inside the cooling plate. All measurements discussed here are at steady-state.

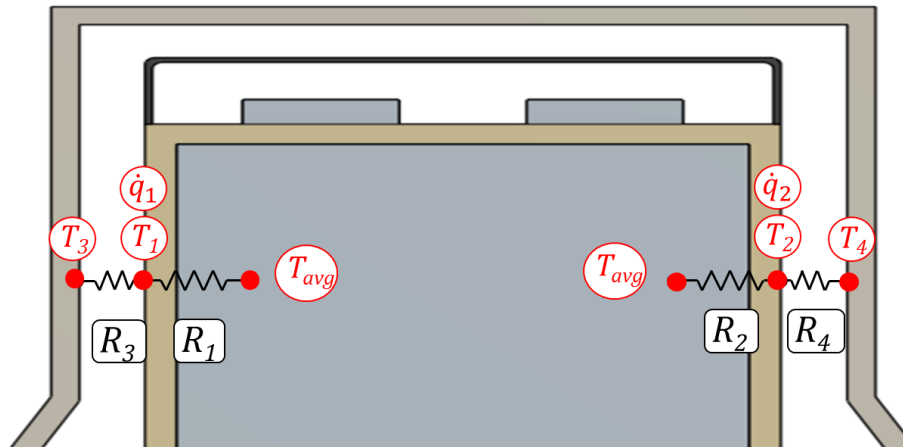


Figure 4.11 - Side path sensor placement

$R_1$  would be calculated as follows:

$$R_1 = \frac{\Delta T_1}{\dot{Q}_1} = \frac{T_{avg} - T_1}{\dot{q}_1 A_{side}} \quad (4.7)$$

The same procedure is used to calculate the other three resistors. To simplify this thermal network from four resistor to two, the side resistors ( $R_1$  and  $R_2$ ) and the airgap resistors ( $R_3$  and  $R_4$ ) are added as parallel resistors as follows:

$$R_{side} = R_{12} = \left( \frac{1}{R_1} + \frac{1}{R_2} \right)^{-1} = \frac{R_1 + R_2}{R_1 R_2} \quad (4.8)$$

$$R_{side\ airgap} = R_{34} = \left( \frac{1}{R_3} + \frac{1}{R_4} \right)^{-1} \quad (4.9)$$

The resistance value {K/W or °C/W} is then multiplied by the total number of cells in the battery pack (288) to scale its value to a per-cell contribution. It is analogous to expanding one single resistor into 288 parallel resistors of equal value; the parallel resistors represent the contribution of each cell and are the values used in the thermal network.

One thing to note is that  $R_{side}$  represents the resistance from the fluid to the outer side frame. Obtaining precise measurements along this thermal chain in order to quantify the individual components contained inside the modules would require the disassembly of entire battery pack. Such work being done by another student in the research group. The general procedure presented forms the basis for all of the thermal resistance measurements. The remaining heat flow paths are described in detail in section 5.2.

### ***Uncertainty Analysis***

The uncertainty analysis for the thermal resistance measurements requires additional steps to the procedure described in Section 4.2.1 since multiple direct measurements ( $\Delta T$  and  $\dot{Q}$ ) are used to make a compound measurement. The effect of the error on each direct measurement must be considered to account for the total uncertainty on the multivariate measurement or result. The resulting total uncertainties are used to define the tolerance range associated with each thermal resistance in the thermal circuit.

The uncertainty in the result,  $U_R$ , is made up of a bias and a precision term, similar to the measurement uncertainty:

$$U_R = \sqrt{B_R^2 + (tS_R)^2} \quad (4.10)$$

The result bias limit ( $B_R$ ) and precision index ( $S_R$ ) are determined using Equations (4.11) and (4.12), respectively.

$$B_R = \sqrt{\sum_{i=1}^n \left( \frac{\partial R_{M_i}}{\partial M_i} B_{M_i} \right)^2} \quad (4.11)$$

$$S_R = \sqrt{\sum_{i=1}^n \left( \frac{\partial R_{M_i}}{\partial M_i} S_{M_i} \right)^2} \quad (4.12)$$

The partial derivative term (sometimes denoted as  $c$ ) is a sensitivity coefficient of the result from a change in each individual measurement,  $M_i$ . This coefficient can be determined analytically through differentiation, or numerically by evaluating the relation using an incremental change in the measurement. The RSS of the sensitivity coefficient multiplied by the bias (or precision) of  $n$  direct measurements is taken to obtain the total bias limit and precision index on the resultant measurement. Equation (4.10) is then applied to determine the total uncertainty on the thermal resistance measurement.

The uncertainty propagates further as multiple resistance measurements are used together in a calculation, as in the case of the addition of parallel paths. To quantify the spread of uncertainty in a calculation, the methods outlined in [97] are used. The error in a sum of two measurements (or results) is calculated by the RSS of the uncertainties in each measurement:

$$U_{sum} = \sqrt{U_{R1}^2 + U_{R2}^2} \quad (4.13)$$

The error in a product of two measurements is calculated by the RSS of the fractional uncertainties in each measurement ( $\pm\%$  of nominal):

$$U_{product} = \sqrt{\left(\frac{U_{R1}}{R1}\right)^2 + \left(\frac{U_{R2}}{R2}\right)^2} \quad (4.14)$$

The most likely maximum error in a quotient of two results can be estimated also using the RSS of the fractional uncertainties of each result as per Equation (4.14).

### ***Side Frame Example***

The inlet side frame will be used as an example to illustrate the process estimating the level of uncertainty in a thermal resistance measurement. The following measured values taken from a single experiment will be used to carry out the analysis. The notation used to label the measurement points in Figure 4.11 is maintained.

#### Measured values:

$$\dot{Q}_1 = \dot{q}_1 A_{side} = \mathbf{6.012 \text{ W}}, \quad \Delta T_1 = T_{avg} - T_1 = \mathbf{1.0 \text{ }^\circ\text{C}}$$

The direct measurements of temperature difference ( $\Delta T_i$ ) and heat flow ( $\dot{Q}_i$ ) are used to calculate a thermal resistance value ( $R_i$ ) with Equation (4.7), which is the compound measurement or result.  $A_{side}$  is the area of the surface which the measured heat flux is said to emanate from; in this example, it is the surface area of the inlet side frame for the entire pack. It is important to note that heat flow and resistance are representative of the full pack; the per-cell conversion is carried out at the end of the analysis.

#### From Equation (4.7):

$$R_1 = \frac{\Delta T_1}{\dot{Q}_1} = \frac{1.0 \text{ }^\circ\text{C}}{6.012 \text{ W}} = \mathbf{0.1663 \frac{^\circ\text{C}}{\text{W}}}$$

The following bias ( $B_M$ ) of each direct measurement are taken from Table 4.1; the table is said to contain total uncertainty values, but as noted earlier, the total uncertainty converges to the bias limit for large sample sets.

$$B_{\Delta T} = \mathbf{0.1097^\circ C}, \quad B_{\dot{Q}_1} = \mathbf{0.7428 W}$$

The precision index ( $S_M$ ) is determined by applying Equation (4.3) to each measurement signal. The following values are obtained by analyzing the measurement signals: Here,  $S_{\dot{q}_1}$  was determined from 3559 measurement samples from a heat flux sensor placed at the location of  $\dot{q}_1$  from Figure 4.11.

$$S_{\Delta T} = \mathbf{0.1097^\circ C}, \quad S_{\dot{Q}_1} = S_{\dot{q}_1} A_{side} = \left(0.06061 \frac{W}{m^2}\right) (0.2472m^2) = \mathbf{0.01499 W}$$

In order to apply Equations (4.10) - (4.12), which determine the total uncertainty, the sensitivity coefficients ( $\partial R_{M_i}/\partial M_i$ ) must also be calculated. In this analysis, the partial derivative terms are determined numerically. Since the compound measurement is made up of two direct measurements, the sensitivity coefficients to be determined are  $\partial R_{\Delta T_1}/\partial \Delta T_1$  and  $\partial R_{\dot{Q}_1}/\partial \dot{Q}_1$ . The denominator represents an infinitesimal change in the direct measurement. In practical terms, it is the smallest measurement increment, which turns out to be the bit resolution of the DAQ. Bit resolutions for all measurement types have already been presented in Table 4.1. For the measurement system employed here, the following resolutions are achieved:

$$\partial \Delta T_1 = \mathbf{0.1097^\circ C}, \quad \partial \dot{Q}_1 = \partial \dot{q}_1 * A_{side} = \left(1.5 \frac{W}{m^2}\right) (0.2472m^2) = \mathbf{0.3708 W}$$

The numerator ( $\partial R_M$ ) is evaluated using a finite-difference approach. It can be seen as the change in the compound measurement due to the smallest detectable change in a direct measurement. The following equation evaluates this term:

$$\partial R_{M_i} = R_{M_i} - R_{M_i + \partial M_i} \quad (4.15)$$

Where  $R_{M_i + \partial M_i}$  is the compound measurement evaluated at a direct measurement value of  $M_i + \partial M_i$ . Applying this method to the direct measurements in this example:

$$\partial R_{\Delta T_1} = R_{\Delta T_1} - R_{\Delta T_1 + \partial \Delta T_1} = R_1 - \frac{\Delta T_1 + \partial \Delta T_1}{\dot{Q}_1} = 0.1663 \frac{^\circ\text{C}}{\text{W}} - \frac{(1.0 + 0.1097) ^\circ\text{C}}{6.012 \text{ W}}$$

$$\partial R_{\Delta T_1} = -0.01828 \frac{^\circ\text{C}}{\text{W}}$$

$$\partial R_{\dot{Q}_1} = R_{\dot{Q}_1} - R_{\dot{Q}_1 + \partial \dot{Q}_1} = R_1 - \frac{\Delta T_1}{\dot{Q}_1 + \partial \dot{Q}_1} = 0.1663 \frac{^\circ\text{C}}{\text{W}} - \frac{1.0 ^\circ\text{C}}{(6.012 + 0.3708) \text{ W}}$$

$$\partial R_{\dot{Q}_1} = 0.009629 \frac{^\circ\text{C}}{\text{W}}$$

The sensitivity coefficients can now be evaluated fully:

$$\frac{\partial R_{\Delta T_1}}{\partial \Delta T_1} = \frac{\left(-0.01828 \frac{^\circ\text{C}}{\text{W}}\right)}{0.1097 ^\circ\text{C}} = 0.1666 \frac{1}{\text{W}}$$

$$\frac{\partial R_{\dot{Q}_1}}{\partial \dot{Q}_1} = \frac{\left(0.009629 \frac{^\circ\text{C}}{\text{W}}\right)}{0.3708 \text{ W}} = 0.02597 \frac{^\circ\text{C}}{\text{W}^2}$$

Continuing with Equations (4.10) - (4.12), and using the previously determined bias ( $B_M$ ) and precision ( $S_M$ ) values, the uncertainty of the inlet side resistance measurement is determined as follows:

$$B_{R_1} = \sqrt{\left(\frac{\partial R_{\Delta T_1}}{\partial \Delta T_1} B_{\Delta T}\right)^2 + \left(\frac{\partial R_{\dot{Q}_1}}{\partial \dot{Q}_1} B_{\dot{Q}_1}\right)^2}$$

$$B_{R_1} = \sqrt{\left[\left(0.1666 \text{ W}^{-1}\right) * (0.1097 ^\circ\text{C})\right]^2 + \left[\left(0.02597 \frac{^\circ\text{C}}{\text{W}^2}\right) * (0.7428 \text{ W})\right]^2}$$

$$\therefore B_{R_1} = 0.02659 \frac{^\circ\text{C}}{\text{W}}$$

$$S_{R_1} = \sqrt{\left(\frac{\partial R_{\Delta T_1}}{\partial \Delta T_1} S_{\Delta T}\right)^2 + \left(\frac{\partial R_{\dot{Q}_1}}{\partial \dot{Q}_1} S_{\dot{Q}_1}\right)^2}$$

$$S_{R_1} = \sqrt{[(0.1666 \text{ W}^{-1}) * (0.001085^\circ\text{C})]^2 + \left[\left(0.02597 \frac{^\circ\text{C}}{\text{W}^2}\right) * (0.01499 \text{ W})\right]^2}$$

$$\therefore S_{R_1} = \mathbf{0.0004304 \frac{^\circ\text{C}}{\text{W}}}$$

$$U_{R_1} = \sqrt{(0.02659)^2 + (1.96 * 0.0004304)^2} = 0.02661 \frac{^\circ\text{C}}{\text{W}}$$

$$\therefore U_{R_1} = \left(0.02661 \frac{^\circ\text{C}}{\text{W}}\right) * 288 \text{ cells} = \mathbf{7.66 \frac{^\circ\text{C}}{\text{W}} \text{ per cell}}$$

The calculations are carried out using heat flow measurements, which is the heat flux divided by the surface area. The uncertainty value is dependent on the testing temperature. At higher temperatures, the signal to noise ratio is higher and the uncertainty is decreased. To account for this, the mean of the uncertainty of all the runs is taken as the average uncertainty, or approximately 4.98 °C/W for the inlet side frame resistance. This calculation process is repeated for every individual resistance measurement using a spreadsheet. This summary is presented in Appendix A.

The total side frame resistance  $R_{side}$  is calculated to be 29.1 °C/W using Equation (4.8) on page 46. Equations (4.13) and (4.14) are used to estimate this uncertainty, along with those of both side resistance measurements. These uncertainties are calculated to be 5.61% in the numerator (sum) and 13.4% in the denominator (product), which yields a total uncertainty of 14.5% from a measurement value of 29.1 °C/W, yielding an uncertainty of 4.2 °C/W. This process is repeated whenever parallel paths are added together. The uncertainty estimates for each resistor in the network are shown later in Section 5.2.3.

### **4.2.3 Effect of emissivity on measurements**

Measuring temperature and heat flux on the outside of the cover proved to be difficult due to its low emissivity. The issue was first detected when the level of heat flowing out of the cover was recorded as approximately twice the measurement of heat escaping from the modules. After thoroughly investigating every possible path of heat leakage around the modules with no success, the only avenue remaining was to investigate the behaviour of the sensors themselves. Heat flux sensors were placed on the inside surface of the cover and provided similar heat flux readings as found with the module sections. This confirmed that the heat flux and temperature measurements taken on the outside cover were somehow incorrect. The aim of this section is to shed light on an issue that appears to be easily overlooked and to help others in gathering meaningful measurements.

#### ***Mechanism***

The effect of thermocouple emissivity on slow moving gas temperature measurement is well-known and discussed in almost every heat transfer and instrumentation textbook. The thermocouple “reads” a lower temperature than that of the gas since it emits more radiation due to its relatively high emissivity. The temperature measurement of reflective surfaces is almost never discussed. Thermocouples are generally cemented into place (semi-permanent) or taped onto the surface (removable). In this work, tape is used to prevent damage to the surfaces and to easily reuse the sensors in different locations. This mounting method is very reliable on most surfaces, but introduces errors when employed on a reflective surface.

The discrepancy comes from the difference in emissivity between the sensors and the surface being measured. The emissivity of the sensors (thermocouples and heat flux) is similar to that of common opaque painted surfaces, which lie around 0.9. The outside of the battery pack enclosure is covered in reflective film similar in emissivity to aluminum foil (~0.1-0.3). Radiation heat transfer is facilitated on a high emissivity surface, resulting in higher heat flux and ultimately lower temperature readings. This

effect also causes heat to be conducted from the surrounding film and funneled through the high emissivity sensors.

### ***Correction Method***

The measurement issue was discovered after the majority of the tests were completed, thus a correction method for the existing data needed to be developed rather than repeating several months of testing. A mathematical correction based on heat transfer theory could be developed but would be complex and time consuming. An additional set of experiments was devised to extract an appropriate correction method.

The idea of the experiment was to mimic the cover's reflective surface on a controlled heat source in order to calibrate the heat flux sensors and thermocouples for this situation. Methods of mitigating the errors were also investigated. A silicone heating pad (Omegalux SRFG-607/2 from Omega), shown in Figure 4.12 was wrapped in aluminum foil with the dull side out in an attempt to best match the surface of the battery pack cover.

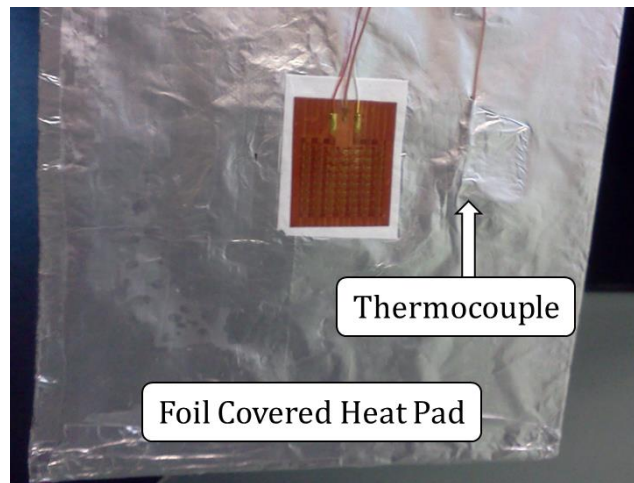


Figure 4.12 – Foil-covered heat pad experiment

The heat pad was suspended vertically, with a thermocouple and heat flux sensor fixed to the centre of the pad. Assuming uniform heat generation through the pad, the surface heat flux is calculated and compared to the sensor reading. A thin

thermocouple wire is pierced through the foil in order to best capture the temperature of the metallic surface, and compared with the built-in thermocouple on the heat flux sensor.

The voltage to the electrical heat pad was increased from 0-30 V in increments of 5 V to obtain of different heating rates. The steady-state heat flux and temperatures were recorded for each heating power level. Figure 4.13 shows the relationship between the heat flux sensor readings to the calculated heat flux from the pad. A linear best fit is taken, with the slope being the correction factor.

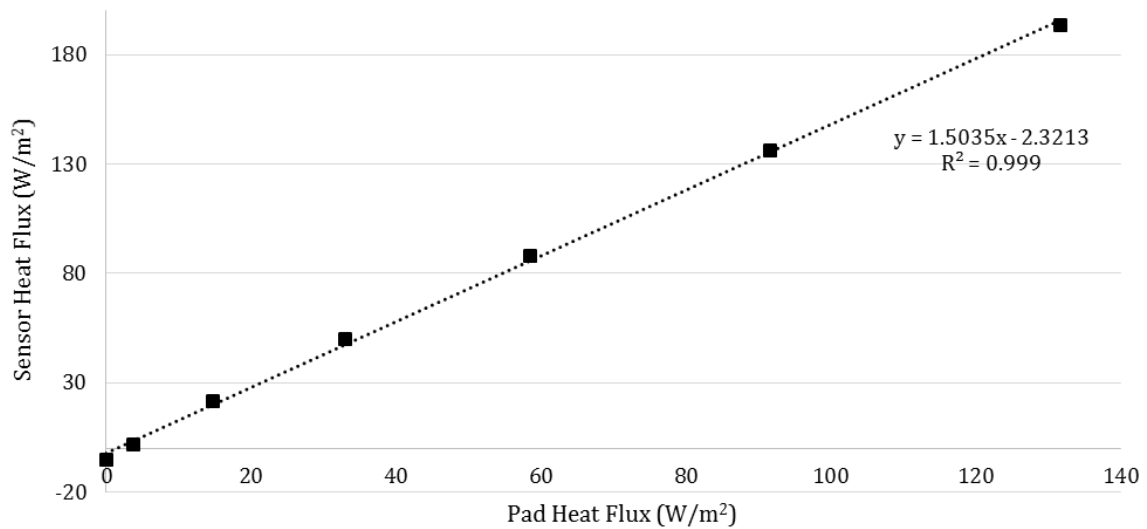


Figure 4.13 - Sensor heat flux with varying pad heat flux

The difference between the heat flux sensor's thermocouple (sensor) and the embedded thermocouple (foil) is shown in Figure 4.14. A second order polynomial is used as it provides the best fit in the span of temperatures seen in the lab tests. From Figure 4.13, it can be seen that the sensor effectively channels approximately 50% more heat due to its high emissivity relative to the foil.

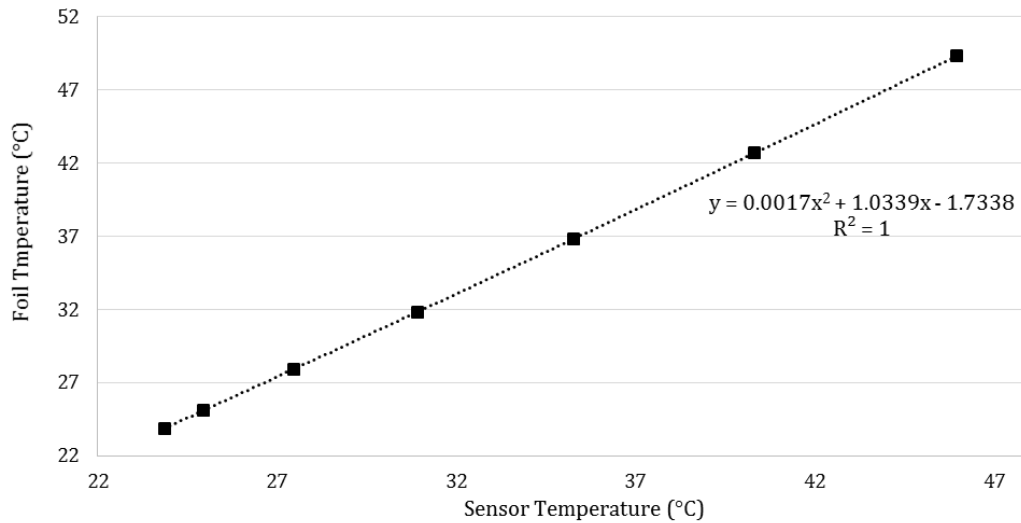


Figure 4.14 - Foil and sensor temperatures at varying heating rates

Figure 4.14 confirms that the foil attains a slightly higher temperature than the heat flux sensor. Temperatures below 22 °C cannot be extrapolated using this fitting method but this is not an issue during the lab tests. Since multiple sensors needed to be corrected, the same test was run using a different heat flux sensor, and the previously computed correction factors were applied. The results from this test indicated that the correction factors obtained were sufficient. The error in heat flux did not exceed 5% and the maximum temperature error was 0.11 °C. With satisfactory variation between sensors, the corrections were then verified in relation to the outside of the battery pack enclosure. Two heat flux sensors were mounted normally on the cover and four thermocouples were mounted using the method shown in Figure 4.15. The insulating tape that was previously used to cover the thermocouples was replaced with aluminum foil and a temporary adhesive, in attempt to match the surface emissivity and capture the correct foil temperature.

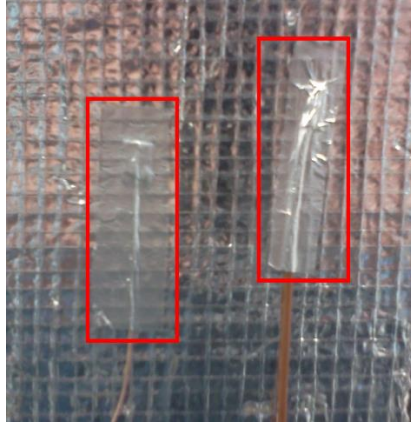


Figure 4.15 - Outside cover thermocouples covered in foil (outlined)

The battery pack was internally heated as in all previous testing, and the thermocouple readings were compared to the temperature of the heat flux sensors. The temperature of the heat flux sensors was approximately 2 °C off, with the error shrinking to 0.2 °C after the correction factors were applied. With a reasonable error level attained for temperature on the cover's outer surface, the correction method was deemed acceptable.

### ***Suggestions for similar applications***

Should similar experiments be run in the future, a few techniques are recommended to increase the reliability of these measurements. Surface-mounted thermocouples ought to be covered in a thin material with properties similar to the surface to be measured. The insulating tape should be replaced with reflective aluminum foil tape, or alternatively a piece of aluminum foil with adhesive. Thermopile type heat flux sensors need to be calibrated based on the emissivity of the surface to be measured similar to what was done using the foil covered heat pad. Here, the sensors cannot be covered in foil (unlike the thermocouples) due to thermal bridging occurring between the surface and the top of the sensor (i.e. no temperature difference = no sensor signal). The built-in thermocouple would therefore not be used and should instead be replaced by a foil-covered thermocouple.

If possible, forced convection can be introduced (uniformly) which greatly reduces the relative effect of radiation. The heat pad experiment was also run with a fan blowing over the setup and with this change, heat flux readings did not require any correction. If the methods discussed would have been employed from the beginning, the experimentation process could have ran more smoothly, thus saving time and reducing frustration when the requisite energy balance did not work out. This insight should be valuable to anyone attempting similar types of measurements.

#### 4.2.4 Heat Flux Measurement Validation

In order to verify that other serious errors were not present in the heat flux measurements, a heat flow balance analysis was performed. Heat flow through the modules (not connected to the baseplate), the inside of the cover, and the outside of the cover were compared to one another. Heat emanates from the module frames and endplate, into the air gap enclosed by the cover, and then flows through the cover. A balance between the three measurements would indicate that the heat flow measurements are valid. Table 4.2 shows the total heat flow in {W} through the three paths for all fluid temperatures and flowrates.

Table 4.2 - Heat flow balance through cover path for all tests

Fluid ↓	Out of Module {W}			Into Cover {W}			Out of Cover {W}		
	3 Lpm	6 Lpm	9 Lpm	3 Lpm	6 Lpm	9 Lpm	3 Lpm	6 Lpm	9 Lpm
30 °C	16.7	16.8	20.9	17.0	16.8	17.8	17.8	18.0	18.4
37 °C	39.0	39.7	39.0	39.0	40.5	40.1	41.8	41.6	42.1
45 °C	68.4	71.4	75.4	71.8	74.2	73.6	71.1	73.5	74.2
50 °C	90.2	93.1	89.7	83.9	86.4	88.9	91.9	93.3	97.4
55 °C	109.5	114.6	113.8	114.2	118.5	121.0	110.9	114.7	113.8

Comparing the three paths for each test, 3 Lpm at 30 °C for example, the standard deviation is 0.57 W which is 3.3% of the total value. The largest deviation occurs at 30 °C / 9 Lpm but does not exceed 9%. This variation is deemed acceptable since there is no set pattern, and is most likely caused by day-to-day variations in lab temperature and circulation rather than sensor error. This comparison helps reassure that the heat flux corrections and measurement method are fundamentally sound.

## 5 MODEL DEVELOPMENT AND VALIDATION

---

This section describes the development and refinement process for the external portion of the thermal network model. Electrical circuit simulation software (OrCAD PSpice) was used to build, simulate, and analyze the performance of the thermal network compared to the lab tests. PSpice has a graphical interface that allows the user to visually construct and simulate a circuit made up of common electrical components. The refinement process was carried out in two steps: steady-state, and transient. The resulting thermal network model is presented at the end of the section.

### 5.1 CHANGES TO ORIGINAL MODEL

The laboratory model being developed in this chapter has several differences from the original circuit described in Section 4.1.3. In the lab, the input sources from the engine, chassis, road, and underbody are first removed since the battery pack is not on the vehicle but is stationary. The input current source representing cell heat generation is also eliminated since the cells remain electrically dormant during lab testing. Eliminating these sources allows for heat to flow in only one direction, from fluid to the environment. The second difference is the representation of the components contained within the frames. These components are not accessible without having to completely dismantle the battery pack and are modeled as equivalent resistors that represent the heat path from the fluid to the exterior surface of the module. These paths are explained in detail in Section 5.2.

The other set differences between the original model and the one being presented here lies in the layout and definition of the heat paths. In the lab model, the nodal points are defined only by measureable surface temperatures, and resistors are only placed where the heat flux can be measured. An example of this is the manifold to bulkhead resistance ( $R_8$  in Figure 4.2) defined in the original model. While this path may still exist, the heat flow between the two components cannot be quantified

experimentally and a resistance cannot be measured. The changes instigated will be described in the following section.

## 5.2 STEADY-STATE MODEL

A steady-state model was created by removing all of the capacitors in the circuit, leaving behind a resistance network. Eliminating the capacitors removes the transient behaviour and allows for very fast computation in PSpice. The steady-state currents (heat rates) and voltages (temperatures) are only affected by the resistances. Therefore, preliminary circuit testing at steady-state allows the most correct resistance paths to be identified for the final model. The preliminary lab circuit developed from experiments is shown in Figure 5.1.

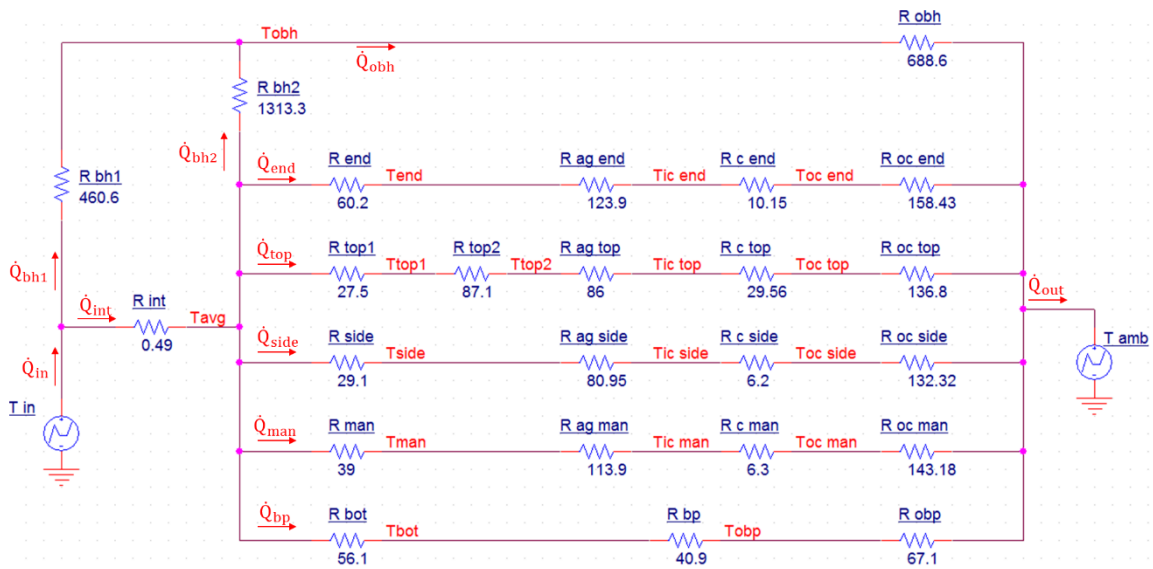


Figure 5.1 - Preliminary lab battery pack thermal model

The indicated node voltages, sources, and currents (heat flow) correspond to physical measurement points taken during the laboratory testing. There are only two voltage sources in the lab circuit: the inlet fluid temperature  $T_{in}$  and the lab ambient temperature  $T_{amb}$ . Temperature node labels and thermal resistance nomenclature are described in Table 5.1; this labelling convention remains consistent throughout this thesis unless otherwise stated.

Table 5.1 - Legend for Figure 5.1: temperature nodes and thermal resistance nomenclature

Temperature Nodes (°C)		Thermal Resistance (°C/W)	
Label	Physical Location	Label	Physical Location
$T_{in}$	Inlet fluid source	$R_{int}$	Inlet fluid to inside of cooling plate
$T_{avg}$	Mean fluid inside cooling plate	$R_{bh1}$	Inlet fluid to bulkhead
$T_{end}$	Endplate	$R_{bh2}$	Inside of battery pack to bulkhead
$T_{top1}$	Top of frame	$R_{end}$	Fluid to endplate surface
$T_{top2}$	Top of battery terminal cover	$R_{top1}$	Fluid to top of frame surface
$T_{side}$	Outer side frame surface	$R_{top2}$	Top frame to top of terminal cover
$T_{man}$	Outer manifold surface	$R_{side}$	Fluid to side frame surface
$T_{bot}$	Outer bottom frame surface	$R_{man}$	Fluid manifold surface
$T_{obh}$	Outside bulkhead surface	$R_{bot}$	Fluid to bottom frame surface
$T_{obp}$	Outside baseplate surface	$R_{bp}$	Bottom frame to outer baseplate surface
$T_{ic end}$	Inside cover – endplate	$R_{obh}$	Bulkhead to ambient
$T_{ic top}$	Inside cover – top	$R_{obp}$	Baseplate to ambient
$T_{ic side}$	Inside cover – side	$R_{ag end}$	Airgap – endplate to inside cover
$T_{ic man}$	Inside cover – manifold	$R_{ag top}$	Airgap – terminal cover to inside cover
$T_{oc end}$	Outside cover – endplate	$R_{ag side}$	Airgap – side frame to inside cover
$T_{oc top}$	Outside cover – top	$R_{ag man}$	Airgap – manifold to inside cover
$T_{oc side}$	Outside cover – side	$R_{c end}$	Cover – endplate section
$T_{oc man}$	Outside cover – manifold	$R_{c top}$	Cover – top section
$T_{amb}$	Ambient temperature source	$R_{c side}$	Cover – side section
		$R_{c man}$	Cover – manifold section
		$R_{oc end}$	Outside cover to ambient – endplate
		$R_{oc top}$	Outside cover to ambient – top
		$R_{oc side}$	Outside cover to ambient – side
		$R_{oc man}$	Outside cover to ambient – manifold

### 5.2.1 Model Description

This section describes the paths in the preliminary steady-state circuit (Figure 5.1) and how each resistance is measured. Drawings showing sensor placement and calculations are given to illustrate the computational process. The resistance values in the circuit are the result of the measurements taken over the series of ~105 test runs at different fluid temperature and flowrate conditions.

#### ***Bulkhead Path***

The fluid enters and exits the battery pack through the front bulkhead. During this process, heat from the fluid is lost to the conducting mass of the bulkhead, which is represented by  $R_{bh1}$  in Figure 5.2. This is a conductive/convective resistance between the fluid manifolds and the outer surface of the bulkhead. As the fluid circulates to the

cooling plates, its temperature drops near to the mean of inlet and outlet; this temperature drop is represented by  $R_{int}$ .  $R_{bh2}$  links the inside of the pack to the outside of the bulkhead, and  $R_{obh}$ , is the convective/radiative resistance from the bulkhead's outer surface to the room.

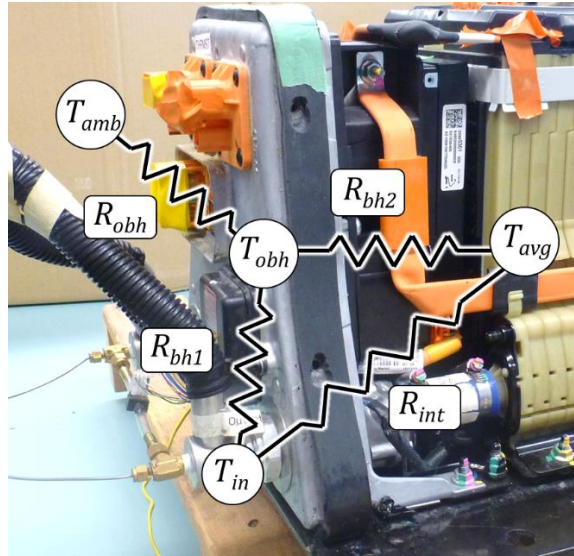


Figure 5.2 - Bulkhead resistances

In order to calculate the three bulkhead resistors, the heat flowing out of the bulkhead ( $\dot{Q}_{obh}$ ), and the heat flowing from the inside of the pack into the bulkhead ( $\dot{Q}_{bh2}$ ), are measured using the sensor placement shown in Figure 5.3.

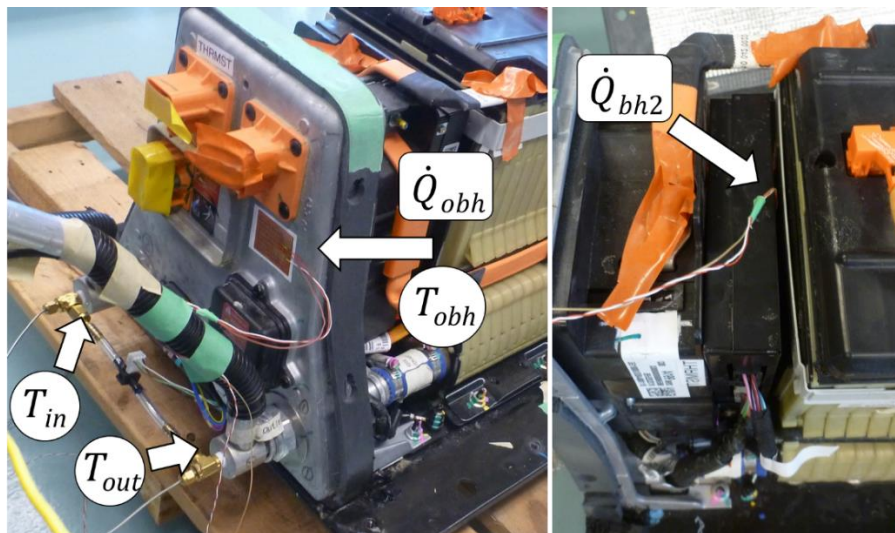


Figure 5.3 - Bulkhead measurement points: outside (left), inside (right)

The  $\dot{Q}_{bh2}$  heat flux sensor is mounted on an electronic module case that is in contact with the internal face of the bulkhead. The bulkhead has an irregular shape (unlike the other components) and its heat flux is difficult to measure as a result. The sensor placements for  $\dot{Q}_{obh}$  and  $\dot{Q}_{bh2}$  are presumed to represent average locations for the exterior and interior of the bulkhead, respectively. This assumption increases the uncertainty of such measurements, but this additional source of error will be excluded from the tolerance of resistors  $R_{bh1}$ ,  $R_{bh2}$ , and  $R_{obh}$  in order to remain conservative during the “tuning” process carried out as described in Section 5.2.3.

The bulkhead path resistances are calculated as follows:

$$R_{modules\ to\ bulkhead} = R_{bh2} = \frac{T_{avg} - T_{obh}}{\dot{Q}_{bh2}}$$

$$R_{fluid\ to\ bulkhead} = R_{bh1} = \frac{T_{in} - T_{obh}}{\dot{Q}_{bh1}}$$

$$R_{outside\ bulkhead} = R_{obh} = \frac{T_{obh} - T_{amb}}{\dot{Q}_{obh}}$$

$$R_{inlet\ fluid\ to\ inner\ cooling\ plate} = R_{int} = \frac{T_{in} - T_{avg}}{\dot{Q}_{int}}$$

$$\dot{Q}_{fluid\ to\ bulkhead} = \dot{Q}_{bh1} = \dot{Q}_{obh} - \dot{Q}_{bh2}$$

$$\dot{Q}_{fluid\ to\ cooling\ plates} = \dot{Q}_{int} = \dot{Q}_{in} - \dot{Q}_{bh1}$$

### **Module Paths**

The fluid enters the modules at the inlet manifold, passes through the cooling plates, and exits the outlet manifold. While the fluid circulates through the cooling plates, heat transfers to the surface of the cells, and out to the plastic frames. The innermost details of this path cannot be discerned directly with this experimental setup alone, but are instead lumped into resistors  $R_{end}$ ,  $R_{top1}$ ,  $R_{side}$ ,  $R_{man}$ , and  $R_{bot}$ . This result is achieved by measuring the resistance from the fluid to the exterior surface of the

module frames which are split into six parts as shown earlier in Figure 4.10. The only module path not shown in the figure is  $R_{end}$  which represents the steel endplate used to compress the modules together.

### Manifold Path

Fluid enters the inlet manifold, passes through the cooling plates and exits through the outlet manifold. The manifolds are therefore the first (inlet) and last (outlet) components to come into contact with the fluid. The manifold frame resistance,  $R_{man}$ , is the resistance from the fluid (denoted as  $T_{avg}$ ) to the exterior surface of the manifolds as shown in Figure 5.4. The dashed lines delineate the manifold section. Temperature nodes are depicted by red circles and heat flux readings are taken on the surface of the manifold and inside or outside of the cover. The resistors shown in the figure are parallel equivalents between the inlet and outlet sides of the pack, and were derived by taking measurements on both sides of the pack.

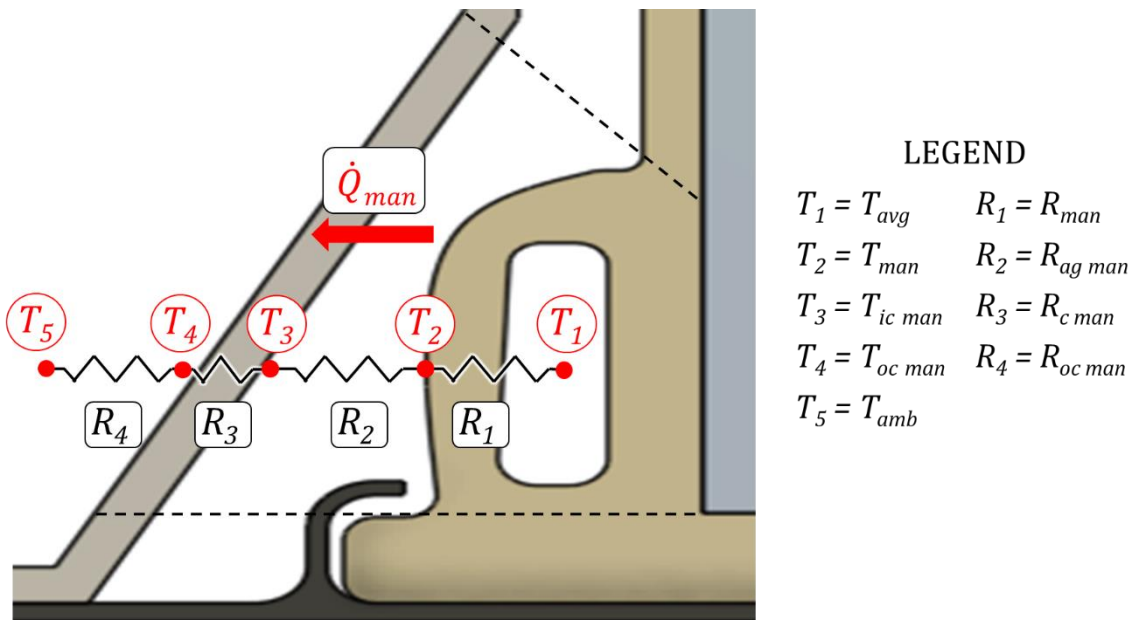


Figure 5.4 –Manifold resistance chain

The manifold path consists of the frame resistance  $R_{man}$ , the airgap resistance  $R_{ag\ man}$ , the cover resistance  $R_{c\ man}$ , and the ambient resistance  $R_{oc\ man}$ . Based on the sensor

placement outlined in Figure 5.4, the following procedure is used to measure the resistances in the manifold path:

$$R_{man} = \left( \frac{1}{R_{man\ in}} + \frac{1}{R_{man\ out}} \right)^{-1} = \left( \frac{\dot{Q}_{man\ in}}{T_{in} - T_{man\ in}} + \frac{\dot{Q}_{man\ out}}{T_{out} - T_{man\ out}} \right)^{-1}$$

$$R_{ag\ man} = \left( \frac{\dot{Q}_{man\ in}}{T_{man\ in} - T_{ic\ man\ in}} + \frac{\dot{Q}_{man\ out}}{T_{man\ out} - T_{ic\ man\ out}} \right)^{-1}$$

$$R_{c\ man} = \left( \frac{\dot{Q}_{cover\ man\ in}}{T_{ic\ man\ in} - T_{oc\ man\ in}} + \frac{\dot{Q}_{cover\ man\ out}}{T_{ic\ man\ out} - T_{oc\ man\ out}} \right)^{-1}$$

$$R_{oc\ man} = \left( \frac{\dot{Q}_{cover\ man\ in}}{T_{oc\ man\ in} - T_{amb}} + \frac{\dot{Q}_{cover\ man\ out}}{T_{oc\ man\ out} - T_{amb}} \right)^{-1}$$

Subscripts in and out refer to the inlet and outlet sides of the pack, respectively.

### Side Path

Like the manifold path, the side is made up of parallel inlet and outlet paths. The resistances found in the path are illustrated in Figure 5.5 along with sensor placements.

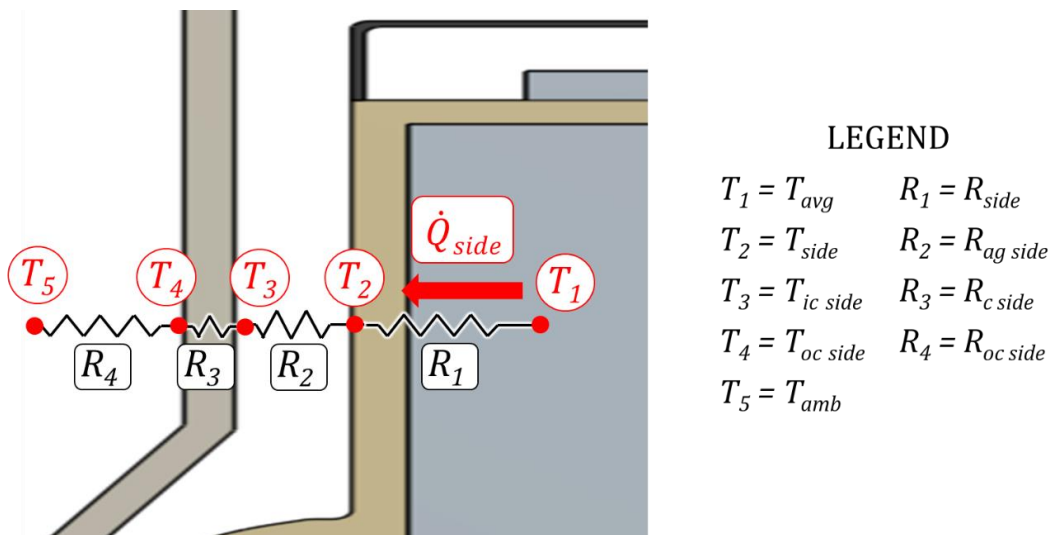


Figure 5.5 - Side path resistances

The side path contains resistance from the frame ( $R_{side}$ ), the airgap ( $R_{ag\ side}$ ), the cover ( $R_{c\ side}$ ), and the air around the cover ( $R_{oc\ side}$ ). The same method of calculating the resistances described for the manifold path apply to the side path.

### Top Path

In the original model, the top and side frames were joined into a single path. Initial testing showed that the behaviour of the top and side frames were quite different and needed to be separated. The top path begins with the fluid to frame resistance  $R_{top1}$ , which represents the resistance to the top of the frames where the battery tabs are secured to each other. A second top resistance,  $R_{top2}$ , represents the battery terminal cover and its contained airgap. Figure 5.6 shows the front view cross-section schematic of a module with the terminal cover on.

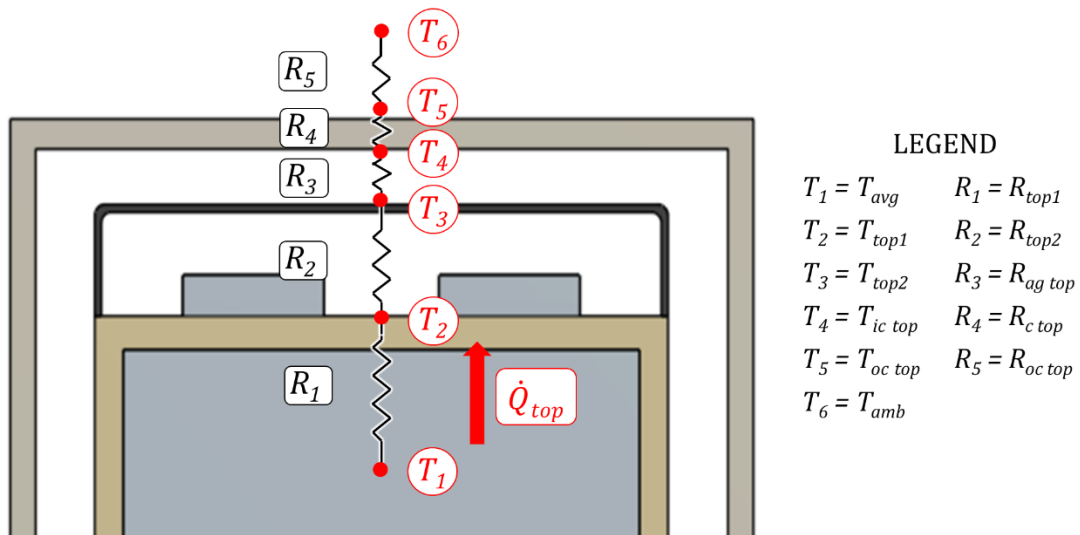


Figure 5.6 – Top resistance chain

The two top resistors are kept separate to provide better dynamics and accuracy due to the increased number of elements and to allow for the addition of another heat source. In future versions of the model, the heat generation caused by the tab contact resistance can be estimated and included as a current source (heating element) connected at the top of the frames. Like the other parts of the frame, the top portion

has an airgap resistance ( $R_{ag\ top}$ ), a cover resistance ( $R_{c\ top}$ ), and an outside air resistance ( $R_{oc\ top}$ ). The resistances are calculated as follows:

$$R_{top\ frame} = R_{top1} = \frac{T_{avg} - T_{top1}}{\dot{Q}_{top}}$$

$$R_{terminal\ cover} = R_{top2} = \frac{T_{top1} - T_{top2}}{\dot{Q}_{top}}$$

$$R_{top\ airgap} = R_{ag\ top} = \frac{T_{top2} - T_{ic\ top}}{\dot{Q}_{top}}$$

$$R_{top\ cover} = R_{c\ top} = \frac{T_{ic\ top} - T_{oc\ top}}{\dot{Q}_{cover\ top}}$$

$$R_{outside\ top} = R_{oc\ top} = \frac{T_{oc\ top} - T_{amb}}{\dot{Q}_{cover\ top}}$$

### ***Endplate Path***

At the ends of each module there are black painted steel compression plates which axially compress the modules. Figure 5.7 shows a side view of a module and the thermal resistances present in this path.  $R_{end}$  represents the path of heat flowing from the fluid out of the endplates. There is also an airgap ( $R_{ag\ end}$ ), a cover portion ( $R_{c\ end}$ ), and an outside radiation/convection resistance ( $R_{o\ end}$ ). There are only four endplate sections as shown in Figure 5.7 in the entire battery pack. This means that the resistance measurements for this path are scaled by a factor of 288/4 in order to obtain the circuit value, which represent their respective influence on a per average cell basis.

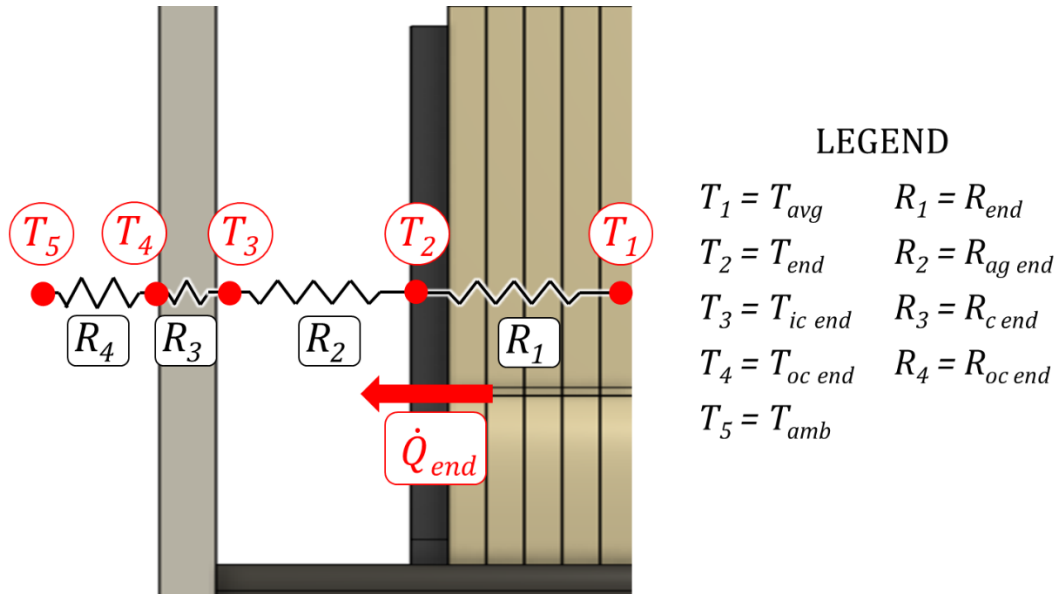


Figure 5.7 - Endplate path resistances

The following equations were followed to calculate the endplate path resistances:

$$R_{endplate} = R_{end} = \frac{T_{avg} - T_{end}}{\dot{Q}_{end}}$$

$$R_{endplate\ airgap} = R_{ag\ end} = \frac{T_{end} - T_{ic\ end}}{\dot{Q}_{end}}$$

$$R_{endplate\ cover} = R_{c\ end} = \frac{T_{ic\ end} - T_{oc\ end}}{\dot{Q}_{c\ end}}$$

The endplate sections of the cover are subjected to different environmental conditions and are measured separately as a result. Figure 5.8 demonstrates the difference between the middle and rear parts of the endplate section of the cover. The major difference is that the middle is free of reflective shielding. This changes the radiative properties of the surface which has an effect on the ambient resistance. The other minor difference lies in their location and orientation. The rear pieces protrude out from the center acting as exposed faces, whereas the two middle pieces face each other. The local differences in air circulation and temperature alter the heat transfer between the middle and rear. To mitigate any errors caused by this, the outside

endplate resistance is split up into a middle and rear portion, then added in parallel to get the equivalent resistor  $R_{oc\ end}$ .

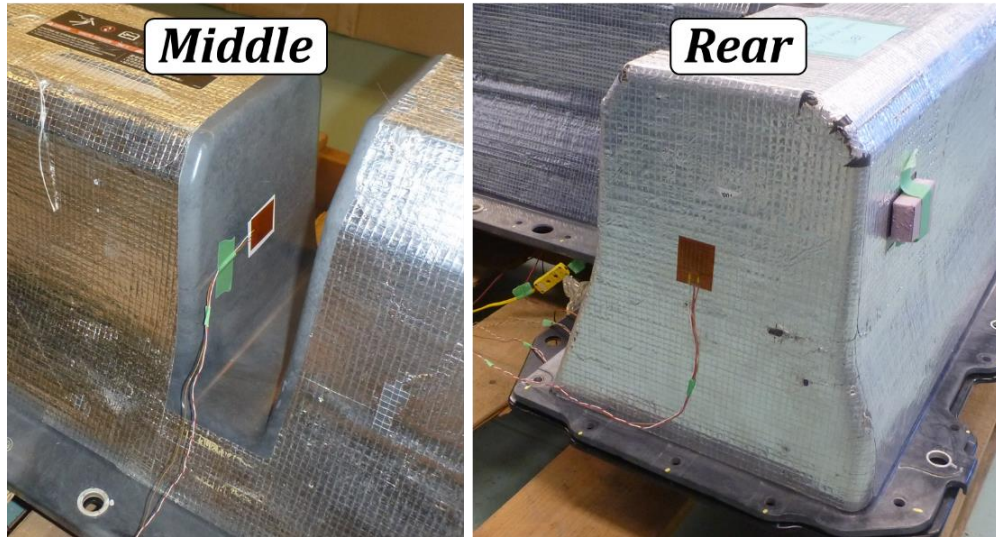


Figure 5.8 - Endplate cover sections

### **Bottom Path**

The bottom part of the frame is clamped down to the baseplate in order to secure the modules in place and the schematic arrangement is shown in Figure 5.9.  $R_{bot}$  is the resistance from the fluid to the bottom of the frame, which comes into contact with the inner surface of the baseplate. The heat exits through the baseplate resistor  $R_{bp}$ , and out to the environment through  $R_{obp}$ .

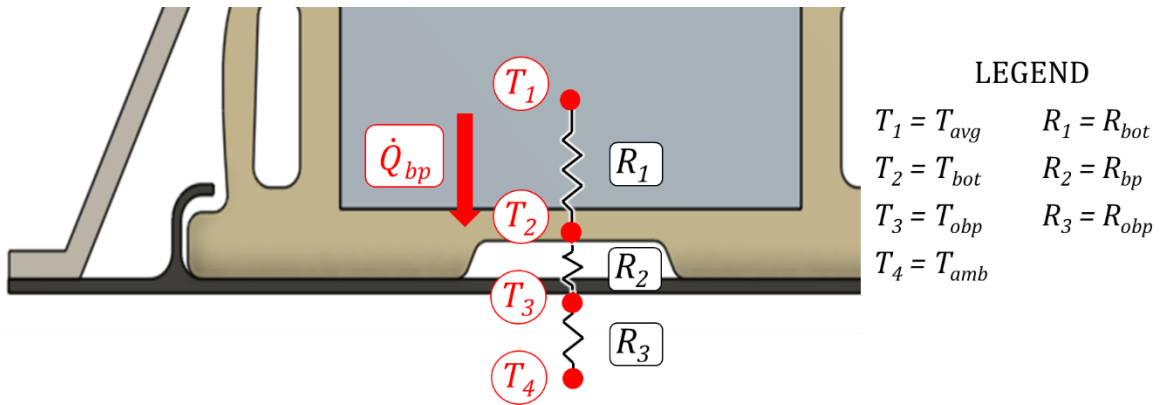


Figure 5.9 - Bottom heat flow path

The bottom frame temperature ( $T_{bot}$ ) could be measured by inserting thermocouples between the baseplate and the frame. The heat flux exiting the bottom frame could not be measured due to its mounting constraints, and had to be estimated based on the assumption that all of the heat entering the baseplate came through the bottom part of the frame. From this assumption, the bottom frame resistance is calculated as follows:

$$R_{bottom} = R_{bot} = \frac{T_{avg} - T_{bot}}{\dot{Q}_{bp}}$$

The baseplate and outside air resistors are calculated as follows:

$$R_{baseplate} = R_{bp} = \frac{T_{bot} - T_{obp}}{\dot{Q}_{bp}}$$

$$R_{outside\ baseplate} = R_{obp} = \frac{T_{obp} - T_{amb}}{\dot{Q}_{bp}}$$

### ***Summary of Heat Flow***

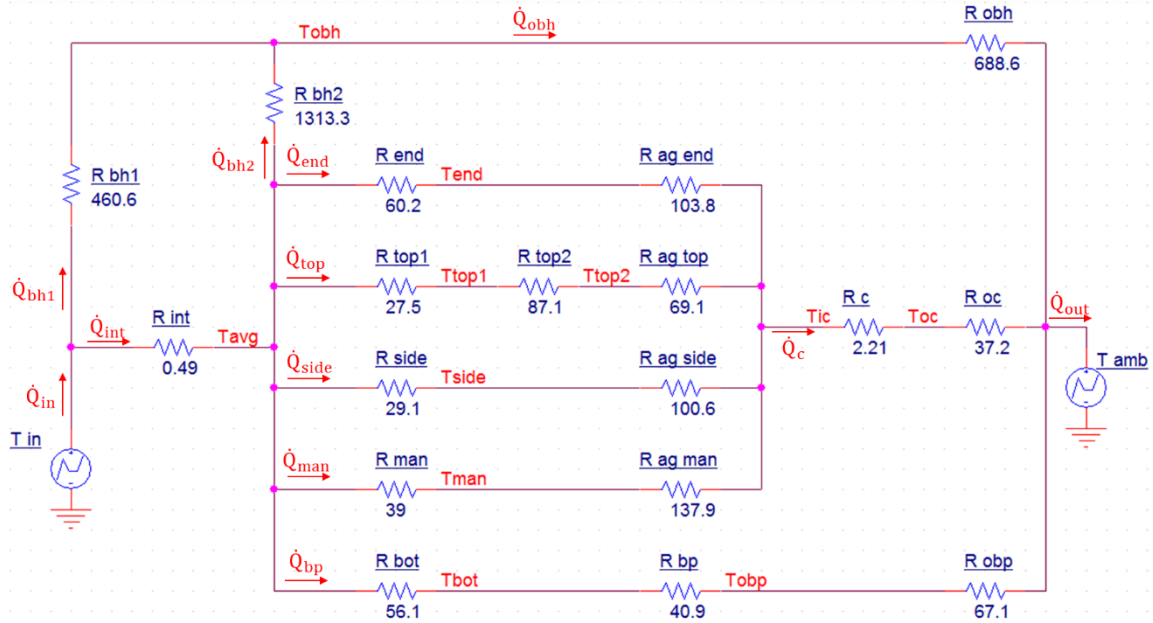
In the lab setting, heat flows from the fluid to the room, which represents a flow from left to right in the circuit shown in Figure 5.1 on page 59. The fluid enters the pack through the front bulkhead and loses some heat in the process. It then progresses to the module assembly through the entry-side manifold, through the cooling plates, and out the exit-side manifold. From the manifold surfaces, the heat also flows through the air and cover, and out to the room. Simultaneously, heat flows from the cooling plates to the cell surface (and interior) and propagates out to the rest of the cell retention frames (top, sides, bottoms, and endplates). Most of this heat enters the local air mass enclosed by the cover, and then flows out through the cover. The heat from the bottom frame portion flows directly into the baseplate, which subsequently exits to the room.

### 5.2.2 Simplification Process

The preliminary lab thermal network described in the previous section was simplified to reduce complexity and simulation time. The main method of simplification involves identifying parallel heat flow paths and reducing them accordingly. Due to the symmetrical nature of the battery pack, the inlet and outlet sides of the pack are considered to shed heat in parallel. Starting from the module, both manifolds are grouped into a single equivalent manifold and the two side frame pieces are also grouped into one. The bottom and top are not symmetrical and are treated as separate pieces.

The cover is made up of the four parts described in the previous section, with each part also having an ambient resistor. These eight resistors can be reduced down to two: the cover, and convection/radiation resistance from the cover to the environment. By redefining the inside and outside cover surface temperatures to their respective average surface temperatures, the individual cover and ambient resistors can be added in parallel to get the equivalent resistors  $R_c$  and  $R_{oc}$ . Figure 5.10 shows the resultant circuit with a single cover resistor  $R_c$  and a single ambient cover resistance  $R_{oc}$ .

It is important to note that for pack redesign purposes, the expanded circuit from Figure 5.1 should be utilized in order to properly assess any design changes relating to local cover sections (inside and outside). For example, if extra insulation was added on the outside of the endplate section of the cover, only the value of  $R_{oc\ end}$  from Figure 5.1 would increase, ultimately leading to an increase in  $R_{oc}$  from Figure 5.10.



### LEGEND

- $T_{ic}$  Average interior cover temperature
- $T_{oc}$  Average exterior cover temperature
- $R_c$  Cover thermal resistance
- $R_{oc}$  Resistance from outer cover to ambient
- $\dot{Q}_c$  Heat flow through cover

Figure 5.10 – Steady-state thermal network with reduced cover path (with legend)

To maintain the same proportionate steady-state heat flow through the four parallel branches now connected to the average inside cover temperature, the airgap resistors need to be adjusted since the potential across them is no longer related to the local inside cover temperature. The changes in circuit value resistances caused by these simplifications are shown in Table 5.2. The airgap resistances remain close to their original values. An increased resistance in the simplified circuit implies that the local cover temperature was originally higher than the average, and a lower resistance implies the opposite.

Table 5.2 - Changes to resistances from the simplification of the airgap, cover, and ambient paths

Expanded		Simplified	
Resistor	Value {°C/W}	Resistor	Value {°C/W}
$R_{ag\ end}$	123.9	$R_{ag\ end}$	103.8
$R_{ag\ top}$	86.0	$R_{ag\ top}$	69.1
$R_{ag\ side}$	81.0	$R_{ag\ side}$	100.6
$R_{ag\ man}$	113.9	$R_{ag\ man}$	137.9
$R_{c\ end}$	10.2	$R_c$	2.21
$R_{c\ top}$	29.6		
$R_{c\ side}$	6.2		
$R_{c\ man}$	6.3		
$R_{oc\ end}$	217.2	$R_{oc}$	37.2
$R_{oc\ top}$	167.8		
$R_{oc\ side}$	132.2		
$R_{oc\ man}$	142.8		

### Steady-state Errors

To quantify the errors in the model, experimental average steady-state nodal temperatures and heat rates are compared to the PSpice simulation output. Table 5.3 compares the nodal temperatures of the simulation (Sim) to the experiments (Exp) for each fluid temperature set point. The difference between the simulation and experiment (Diff) is also shown.

Keeping in mind that the resolution of a thermocouple reading is  $\sim 0.2$  °C, the steady-state errors in temperature are considered relatively low for the runs of 30-45 °C. These deviations increase at higher fluid temperature, which may indicate that some resistors are not entirely constant (contrary to what was assumed). Environmental noise, such as increased ventilation and fluctuating room temperature, also has a greater impact when the battery pack is warmer, which is a source of noise in the measurements. However, if the temperature error is compared to the temperature difference between the fluid and the room, the percent error decreases with increased fluid temperature. The same analysis was repeated for the heat flow through each component and the results are shown in Table 5.4. The values are in units of mW, scaled down to a per-cell basis akin to the resistors denoted in the circuit.

Table 5.3 – Steady-state nodal temperatures: experimental vs. simplified simulation

Run ↓		Nodal Temperature {°C}									
		$T_{obh}$	$T_{end}$	$T_{top1}$	$T_{top2}$	$T_{side}$	$T_{man}$	$T_{bot}$	$T_{bp}$	$T_{ic}$	$T_{oc}$
30 °C	Exp	26.7	27.5	28.0	26.7	27.8	27.8	26.6	25.0	25.3	25.3
	Sim	26.5	27.3	27.9	26.6	27.7	27.7	26.8	24.8	25.5	25.3
	Diff	<b>-0.2</b>	<b>-0.1</b>	<b>-0.1</b>	<b>-0.2</b>	<b>-0.1</b>	<b>0.0</b>	<b>0.2</b>	<b>-0.2</b>	<b>0.1</b>	<b>0.0</b>
37 °C	Exp	31.5	33.4	34.6	32.0	34.2	34.0	32.6	28.1	29.2	28.9
	Sim	31.4	33.2	34.5	31.6	34.0	34.1	32.1	27.9	29.3	28.9
	Diff	<b>-0.2</b>	<b>-0.1</b>	<b>-0.1</b>	<b>-0.4</b>	<b>-0.1</b>	<b>0.1</b>	<b>-0.5</b>	<b>-0.2</b>	<b>0.0</b>	<b>0.0</b>
45 °C	Exp	36.8	39.9	41.7	37.0	40.8	40.9	38.2	31.2	33.0	32.3
	Sim	36.7	39.7	41.7	37.0	41.0	41.0	37.9	31.1	33.3	32.7
	Diff	<b>-0.1</b>	<b>-0.2</b>	<b>0.1</b>	<b>0.0</b>	<b>0.2</b>	<b>0.2</b>	<b>-0.3</b>	<b>-0.1</b>	<b>0.3</b>	<b>0.4</b>
50 °C	Exp	40.0	43.7	46.0	40.2	45.2	45.2	42.0	33.3	35.5	34.6
	Sim	40.2	43.9	46.5	40.6	45.6	45.6	41.7	33.2	35.9	35.2
	Diff	<b>0.2</b>	<b>0.2</b>	<b>0.5</b>	<b>0.4</b>	<b>0.3</b>	<b>0.4</b>	<b>-0.3</b>	<b>-0.1</b>	<b>0.4</b>	<b>0.5</b>
55 °C	Exp	43.6	47.4	50.5	43.4	49.2	49.1	45.1	35.2	37.9	36.8
	Sim	43.6	48.1	51.1	44.1	50.0	50.0	45.4	35.4	38.6	37.7
	Diff	<b>0.0</b>	<b>0.6</b>	<b>0.6</b>	<b>0.7</b>	<b>0.9</b>	<b>0.9</b>	<b>0.3</b>	<b>0.1</b>	<b>0.7</b>	<b>1.0</b>

Table 5.4 - Steady-state heat flow: experimental vs. simplified simulation

Run ↓		Rate of Heat Flow {mW}								
		$\dot{Q}_{obh}$	$\dot{Q}_{ep}$	$\dot{Q}_{top}$	$\dot{Q}_{side}$	$\dot{Q}_{man}$	$\dot{Q}_{bot}$	$\dot{Q}_{bp}$	$\dot{Q}_c$	$\dot{Q}_{out}$
30 °C	Exp	4.4	14.1	13.9	19.7	15.4	33.2	29.5	64.5	98.4
	Sim	5.8	17.2	15.9	22.5	16.5	38.6	34.9	75.8	116.5
	Diff	<b>1.4</b>	<b>3.1</b>	<b>2.0</b>	<b>2.9</b>	<b>1.1</b>	<b>5.4</b>	<b>5.5</b>	<b>11.3</b>	<b>18.1</b>
37 °C	Exp	11.0	32.3	28.7	41.3	34.0	81.6	72.3	149.6	232.8
	Sim	12.2	36.2	33.4	47.4	34.7	81.4	73.6	159.5	245.3
	Diff	<b>1.2</b>	<b>4.0</b>	<b>4.8</b>	<b>6.1</b>	<b>0.7</b>	<b>-0.3</b>	<b>1.3</b>	<b>10.0</b>	<b>12.5</b>
45 °C	Exp	19.9	60.3	53.3	77.5	58.0	133.5	118.4	260.2	398.5
	Sim	19.7	58.7	54.1	76.9	56.2	131.8	119.2	258.5	397.5
	Diff	<b>-0.2</b>	<b>-1.6</b>	<b>0.8</b>	<b>-0.6</b>	<b>-1.8</b>	<b>-1.6</b>	<b>0.9</b>	<b>-1.7</b>	<b>-1.0</b>
50 °C	Exp	26.3	74.5	70.6	96.1	74.8	164.6	147.5	335.8	509.6
	Sim	24.7	73.3	67.6	96.0	70.2	164.7	148.9	322.9	496.4
	Diff	<b>-1.7</b>	<b>-1.2</b>	<b>-3.0</b>	<b>-0.1</b>	<b>-4.5</b>	<b>0.0</b>	<b>1.4</b>	<b>-12.9</b>	<b>-13.2</b>
55 °C	Exp	34.7	92.0	84.0	122.8	92.3	202.5	183.3	403.1	621.1
	Sim	29.2	86.7	80.0	113.6	83.1	194.8	176.2	382.0	587.4
	Diff	<b>-5.6</b>	<b>-5.3</b>	<b>-3.9</b>	<b>-9.3</b>	<b>-9.2</b>	<b>-7.7</b>	<b>-7.0</b>	<b>-21.0</b>	<b>-33.6</b>

The error in total system heat flow becomes more negative as the fluid temperature increases, which suggests that some resistances should be decreasing rather than remaining constant. The resistor values chosen for the circuit are made up of the average resistances over the five temperature runs, which is the reason the 45 °C run has the lowest error. The resistors which are dependent on convection and radiation ( $R_{bh1}$ ,  $R_{obh}$ ,  $R_{oc}$ , and  $R_{obp}$ ) are non-linearly dependent on the temperature difference between the surface and surrounding fluid (coolant or air).

Heat transfer through most components in the circuit is dominated by conduction, which is directly proportional to the temperature differential (i.e. constant resistance). The external resistors however, have emerging convection and radiation components. Radiation heat transfer is dependent on the 4<sup>th</sup> power of temperature, and convection is less than directly proportional to the temperature differential (case dependent) [49]. Therefore, over the temperature range of interest, the non-linearity caused by radiation and convection must be considered where applicable.

Table 5.5 - Resistance changes with temperature

	30 °C	37 °C	45 °C	50 °C	55 °C	AVG
$R_{bh1}$	520.8	511.8	459.3	436.7	374.3	<b>460.6</b>
$R_{obh}$	951.2	779.6	688.6	638.2	579.1	<b>727.3</b>
$R_{oc}$	49.8	43.5	40.2	37.8	34.9	<b>41.2</b>
$R_{obp}$	87.4	71.2	69.0	68.4	63.9	<b>72.0</b>

Table 5.5 shows the decrease in resistance of the components sensitive to convection and radiation for each temperature run. When the surface temperature is higher, convection and radiation are facilitated (higher temperature difference). This translates to a lower resistance and agrees with the trend shown in Table 5.5. The solution to correct this trend is presented in the following section.

### 5.2.3 Refinement

The simplified circuit from the previous section (Figure 5.10) produces results with reasonable temperature and heat rate errors at steady-state, but improvements are still possible. The lowest achievable error at steady-state will help ensure the model's

accuracy during transient periods. The refinement process consists of modifying resistor values within an acceptable range, and incorporating variable resistors.

**Variable Convective and Radiative Resistors**

One of the sources of error at steady-state was the effect that convection and radiation has on the outer resistance values. These resistors,  $R_{bh1}$ ,  $R_{obh}$ ,  $R_{oc}$ , and  $R_{obp}$ , should therefore be replaced with variable resistors. The issue is that the resistance is dependent on the temperature difference between the surface and its environment. These dynamic resistors thus need to be controlled by this temperature differential, which is known as a voltage-controlled resistor in electrical terms.

The PSpice software does not have a built-in voltage-controlled resistor predefined in its component libraries. Instead, a voltage-controlled current-source is used to mimic the behaviour of a variable resistor. The PSpice component used is called a GVALUE component, where G represents the source type and VALUE represents the output gain type.

The current output is related to the input voltage difference through a specified gain value and therefore Ohm’s law can be used to change the component’s behaviour to act like a resistor. The output current is simply made equal to the input voltage divided by the desired resistance. Figure 5.11 demonstrates how Ohm’s law can be applied to the GVALUE component on the right in order to mimic the simple resistor on the left, based on the voltage difference across the resistor. For the same voltage difference ( $V2 - V1$ ), both components experience the same current flow ( $I$ ).

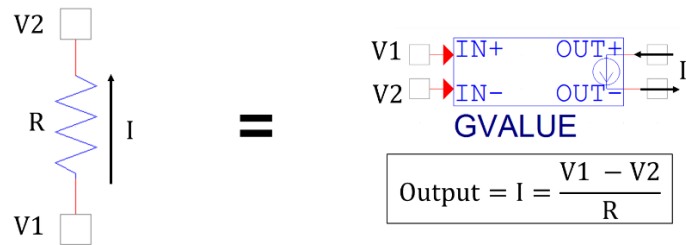


Figure 5.11 – Schematic showing the equivalency between a resistor and a modified GVALUE component

The output expression can be further modified to mimic a variable resistor by defining conditions for the desired value of R. The analog behavioural modelling (ABM) library in PSpice is used to mimic a voltage-controlled resistor; a lookup table relating voltage drop to resistance is programmed into the component's properties, which are used to define the change in resistance with voltage. Table 5.6 shows the lookup tables of  $\Delta T$  {V} and resistance { $^{\circ}\text{C}/\text{W}$ } for each variable resistor to be programmed into PSpice.

Table 5.6 - Voltage-controlled resistor lookup tables for  $R_{bh1}$ ,  $R_{obp}$ ,  $R_{oc}$ , and  $R_{obh}$ ,

Run ↓	Fluid to Bulkhead ( $R_{bh1}$ )		Outer Baseplate ( $R_{obp}$ )		Outer Cover ( $R_{oc}$ )		Outer Bulkhead ( $R_{obh}$ )	
	$\Delta T$	$^{\circ}\text{C}/\text{W}$	$\Delta T$	$^{\circ}\text{C}/\text{W}$	$\Delta T$	$^{\circ}\text{C}/\text{W}$	$\Delta T$	$^{\circ}\text{C}/\text{W}$
30 $^{\circ}\text{C}$	1.8	520.8	2.6	87.4	2.8	43.4	4.2	951.2
37 $^{\circ}\text{C}$	4.0	511.8	5.1	71.2	5.9	39.7	8.6	779.6
45 $^{\circ}\text{C}$	6.8	459.3	8.2	69.0	9.3	35.6	13.7	688.6
50 $^{\circ}\text{C}$	8.7	436.7	10.1	68.4	11.5	34.2	16.8	638.2
55 $^{\circ}\text{C}$	10.0	374.3	11.7	63.9	13.2	32.9	20.1	579.1

The output expression (EXPR) of the G component from the ABM library is modified to follow Ohm's law along with a lookup table that uses the voltage across the 'resistor' as input to determine the resistance, as per Figure 5.11. In other words, the  $\Delta T$  value (voltage difference) is used to determine the required resistance value { $^{\circ}\text{C}/\text{W}$ }, and Ohm's law is applied in the output expression to flow the correct amount of heat (current). Figure 5.12 shows how this method was used to define the properties of the  $R_{obh}$ . The left side depicts the component properties table in Pspice with the EXPR (expression) row selected. The right side of the figure depicts the component's output current expression that uses the voltage across the component and the lookup table based on the values in Table 5.6.

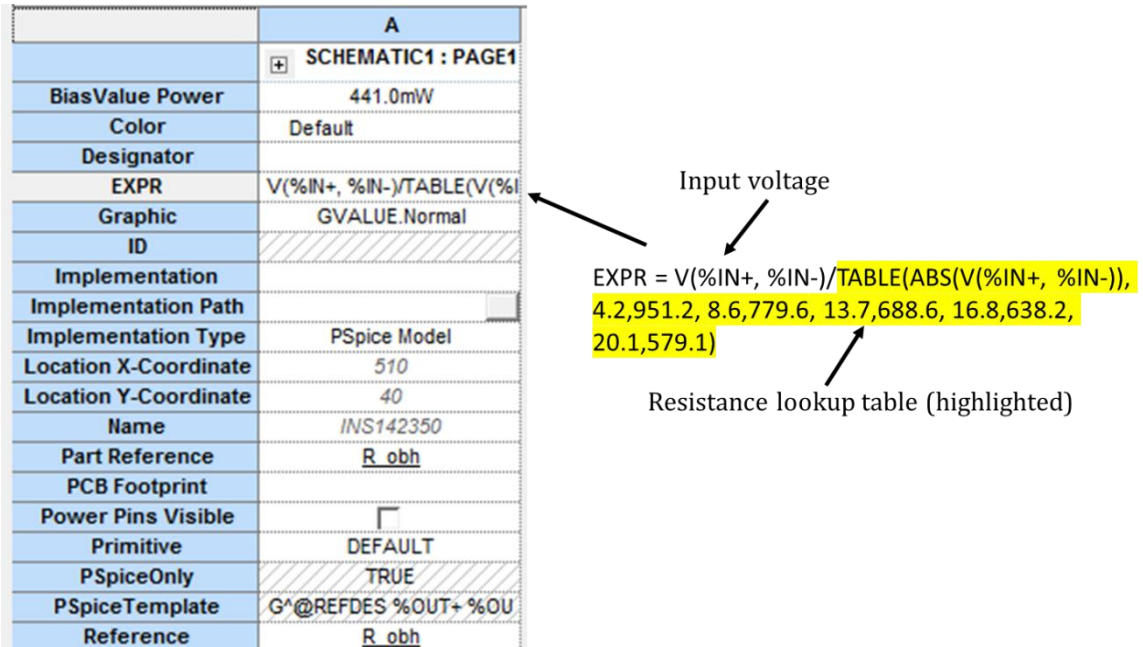


Figure 5.12 -  $R_{obh}$  PSpice component properties with output current expression

Figure 5.13 depicts how the G component is connected in the circuit. The positive and negative voltage inputs are shorted to their respective current outputs to complete the circuit and allow current to flow through the branch.

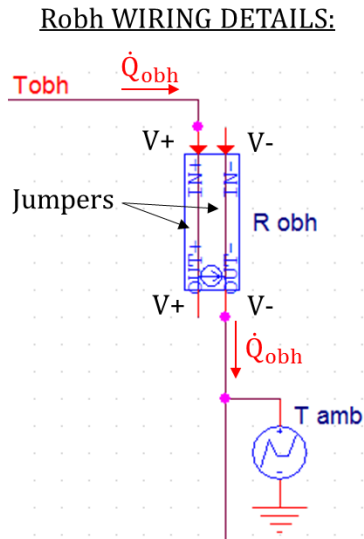


Figure 5.13 - Schematic detailing the electrical connections for  $R_{obh}$

PSpice linearly interpolates between the values in the table, and if an outer voltage limit is exceeded, the limit value is used. Using the bulkhead as an example, if the  $\Delta T$

is 26 °C (higher than 20.1), the resistance of 579.1 °C/W is used. The lookup table's range should therefore encompass the system's full temperature difference range. The ranges given in Table 5.6 are sufficiently wide to span the lab testing conditions.

The steady-state errors in nodal temperature and heat flow after implementing the variable resistors are shown in Table 5.7 and Table 5.8, respectively. Slight improvements in nodal temperatures are achieved, reducing the highest error to 0.7 °C. A marked improvement in heat rate is seen where the highest deviation is only 5.6 mW as compared to the 21 mW from the previous iteration. The total system heat flow is also much closer to the measured values, with 8% maximum error.

Table 5.7 – Steady-state nodal temperatures: experimental vs. simplified simulation with variable resistors

Run ↓		Nodal Temperature {°C}									
		$T_{obh}$	$T_{end}$	$T_{top1}$	$T_{top2}$	$T_{side}$	$T_{man}$	$T_{bot}$	$T_{bp}$	$T_{ic}$	$T_{oc}$
30 °C	Exp	26.7	27.5	28.0	26.7	27.8	27.8	26.6	25.0	25.3	25.3
	Sim	26.7	27.4	28.0	26.7	27.8	27.8	27.0	25.2	25.7	25.5
	Diff	<b>0.1</b>	<b>-0.1</b>	<b>0.0</b>	<b>0.0</b>	<b>0.0</b>	<b>0.0</b>	<b>0.4</b>	<b>0.1</b>	<b>0.4</b>	<b>0.2</b>
37 °C	Exp	31.5	33.4	34.6	32.0	34.2	34.0	32.6	28.1	29.2	28.9
	Sim	31.5	33.3	34.5	31.7	34.1	34.1	32.2	28.1	29.4	29.1
	Diff	<b>0.0</b>	<b>-0.1</b>	<b>0.0</b>	<b>-0.3</b>	<b>-0.1</b>	<b>0.1</b>	<b>-0.4</b>	<b>0.0</b>	<b>0.2</b>	<b>0.2</b>
45 °C	Exp	36.8	39.9	41.7	37.0	40.8	40.9	38.2	31.2	33.0	32.3
	Sim	36.7	39.7	41.8	36.9	41.0	41.0	38.0	31.2	33.1	32.5
	Diff	<b>0.0</b>	<b>-0.2</b>	<b>0.1</b>	<b>-0.1</b>	<b>0.2</b>	<b>0.2</b>	<b>-0.3</b>	<b>0.0</b>	<b>0.1</b>	<b>0.2</b>
50 °C	Exp	40.0	43.7	46.0	40.2	45.2	45.2	42.0	33.3	35.5	34.6
	Sim	40.0	43.7	46.4	40.3	45.4	45.5	41.7	33.3	35.4	34.7
	Diff	<b>0.0</b>	<b>0.0</b>	<b>0.4</b>	<b>0.1</b>	<b>0.2</b>	<b>0.3</b>	<b>-0.3</b>	<b>0.0</b>	<b>-0.1</b>	<b>0.0</b>
55 °C	Exp	43.6	47.4	50.5	43.4	49.2	49.1	45.1	35.2	37.9	36.8
	Sim	43.5	47.7	50.9	43.6	49.8	49.8	45.2	35.0	37.7	36.8
	Diff	<b>-0.1</b>	<b>0.3</b>	<b>0.5</b>	<b>0.2</b>	<b>0.7</b>	<b>0.7</b>	<b>0.1</b>	<b>-0.2</b>	<b>-0.1</b>	<b>0.1</b>

Table 5.8 - Steady-state heat rates: experimental vs. simplified simulation with variable resistors

Run ↓		Rate of Heat Flow {mW}								
		$\dot{Q}_{obh}$	$\dot{Q}_{ep}$	$\dot{Q}_{top}$	$\dot{Q}_{side}$	$\dot{Q}_{man}$	$\dot{Q}_{bot}$	$\dot{Q}_{bp}$	$\dot{Q}_c$	$\dot{Q}_{out}$
30 °C	Exp	4.4	14.1	13.9	19.7	15.4	33.2	29.5	64.5	98.4
	Sim	4.5	16.0	14.8	20.9	15.3	34.9	31.3	70.6	106.4
	Diff	<b>0.1</b>	<b>1.9</b>	<b>0.9</b>	<b>1.3</b>	<b>-0.1</b>	<b>1.6</b>	<b>1.8</b>	<b>6.1</b>	<b>8.0</b>
37 °C	Exp	11.0	32.3	28.7	41.3	34.0	81.6	72.3	149.6	232.8
	Sim	10.9	35.2	32.5	46.1	33.7	79.4	71.9	155.1	237.9
	Diff	<b>-0.1</b>	<b>3.0</b>	<b>3.8</b>	<b>4.8</b>	<b>-0.2</b>	<b>-2.2</b>	<b>-0.4</b>	<b>5.6</b>	<b>5.1</b>
45 °C	Exp	19.9	60.3	53.3	77.5	58.0	133.5	118.4	260.2	398.5
	Sim	19.8	60.2	55.5	78.8	57.7	131.5	118.2	265.5	403.5
	Diff	<b>-0.2</b>	<b>-0.1</b>	<b>2.2</b>	<b>1.4</b>	<b>-0.3</b>	<b>-2.0</b>	<b>-0.2</b>	<b>5.4</b>	<b>5.0</b>
50 °C	Exp	26.3	74.5	70.6	96.1	74.8	164.6	147.5	335.8	509.6
	Sim	26.3	76.1	70.2	99.7	72.9	164.4	147.4	336.0	509.7
	Diff	<b>0.0</b>	<b>1.6</b>	<b>-0.4</b>	<b>3.6</b>	<b>-1.8</b>	<b>-0.2</b>	<b>-0.1</b>	<b>0.2</b>	<b>0.1</b>
55 °C	Exp	34.7	92.0	84.0	122.8	92.3	202.5	183.3	403.1	621.1
	Sim	34.5	91.6	84.6	120.0	87.8	199.0	178.5	404.5	617.5
	Diff	<b>-0.3</b>	<b>-0.4</b>	<b>0.6</b>	<b>-2.8</b>	<b>-4.5</b>	<b>-3.5</b>	<b>-4.7</b>	<b>1.5</b>	<b>-3.5</b>

Hence, the implementation of variable resistors which model convection and radiation effects using modified voltage-controlled current sources proved to be an effective and necessary means of improving the robustness and accuracy of the thermal circuit model.

### ***Modification within Tolerances***

Like any electrical resistor, the resistors in this thermal network can be assigned a tolerance value from which the actual resistance may deviate from a nominal value. In the case of the thermal resistance measurements, the tolerance is related to the uncertainty in the measurement. The tolerance associated with each resistance measurement is calculated using the uncertainty analysis method outlined in Section 4.2.2 and shown in Table 5.9 in the “Tolerance” column. The values are given in °C/W and ±% of nominal resistance.

By examining the steady-state errors in temperature and heat flow, the paths/components with the greatest errors are analyzed in order to pinpoint their root cause(s). The problematic resistors are then modified within their defined tolerances until the errors are minimized. This process also helps identify any issues with the determination of the resistance values themselves. For example, if a resistor (or set of resistors) is modified to the maximum allowable value and the errors are still significant, there is most likely an issue with the resistance calculation or the layout of the network itself in that particular branch. This method of analyzing the errors and identifying their root cause was also used in the early stages of development to help shape the network and cross-check the resistance calculations. The modified values along with their change in magnitude are listed in Table 5.9. The values in this table are treated as the final resistance values for the steady-state model. Variable resistor values are denoted by a range, and values in the “Change” column may represent midrange values.

Table 5.9 - List of resistor tolerances, changes, and final values

Resistor ↓	Tolerance		Initial Value {°C/W}	Final Value {°C/W}	Change {°C/W}
	°C/W	±%			
$R_{bh1}$	-	2.6	374.3 – 520.8	374.3 – 520.8	0
$R_{bh2}$	120.5	9.2	1313.3	1313.3	0
$R_{end}$	3.8	6.3	60.2	57.0	-3.2
$R_{top1}$	4.6	13.0	27.5	30.0	2.5
$R_{top2}$	8.3	9.5	87.1	89.0	2.9
$R_{side}$	4.2	14.5	29.1	32.5	3.4
$R_{man}$	5.1	13.2	39.0	42.5	3.5
$R_{bot}$	1.8	3.2	56.1	57.0	0.9
$R_{bp}$	3.3	8.0	40.9	41.0	0.1
$R_{ag\ end}$	7.8	7.7	103.8	102.0	-1.8
$R_{ag\ top}$	10.8	17.2	69.1	69.0	-0.1
$R_{ag\ side}$	6.6	8.2	100.6	100.0	-0.6
$R_{ag\ man}$	9.9	9.7	137.9	135	-2.9
$R_c$	0.38	17.1	2.21	2.2	-0.01
$R_{obh}$	-	3.1	579.1 – 951.2	579.1 – 951.2	11-18
$R_{oc}$	-	7.6	34.9 – 49.8	34.9 – 49.8	0.2
$R_{obp}$	-	5.6	63.9 – 87.4	66.8 – 89.3	1.3-2.9

The majority of the tolerances lie within 10% of their nominal value. The aim was to keep the changes in resistance minimal, while maintaining good agreement between the simulations and experiments throughout the testing range. The tolerance values serve as rational limits within which the resistance values may be modified, while remaining true to the measurement. As noted previously, some components have additional uncertainties based on difficulty of sensor placement that have been neglected in order to keep the tolerance estimates conservative.

Using the final resistance values from Table 5.9, the steady-state errors are summarized in Table 5.10 and Table 5.11.

Table 5.10 – Steady-state nodal temperatures: experimental vs. simplified simulation with variable resistors

Run ↓		Nodal Temperature {°C}									
		$T_{obh}$	$T_{end}$	$T_{top1}$	$T_{top2}$	$T_{side}$	$T_{man}$	$T_{bot}$	$T_{bp}$	$T_{ic}$	$T_{oc}$
30 °C	Exp	26.9	27.4	28.0	26.7	27.7	27.7	27.0	25.5	25.6	25.5
	Sim	26.9	27.5	27.9	26.7	27.6	27.6	27.0	25.5	25.8	25.6
	Diff	<b>-0.1</b>	<b>0.1</b>	<b>-0.1</b>	<b>0.0</b>	<b>0.0</b>	<b>-0.1</b>	<b>-0.1</b>	<b>0.0</b>	<b>0.2*</b>	<b>0.2*</b>
37 °C	Exp	32.2	33.4	34.4	31.6	34.0	34.0	32.2	28.9	29.4	29.0
	Sim	32.0	33.4	34.3	31.5	33.9	33.9	32.1	28.8	29.3	29.0
	Diff	<b>-0.2</b>	<b>0.0</b>	<b>-0.1</b>	<b>-0.1</b>	<b>-0.1</b>	<b>-0.1</b>	<b>0.0</b>	<b>-0.2</b>	<b>-0.1</b>	<b>-0.1</b>
45 °C	Exp	37.2	39.9	41.8	37.0	41.0	41.0	38.2	32.0	33.5	32.9
	Sim	37.1	39.9	41.8	37.1	41.0	41.0	38.3	32.0	33.4	32.9
	Diff	<b>-0.1</b>	<b>0.0</b>	<b>0.0</b>	<b>0.1</b>	<b>0.0</b>	<b>0.0</b>	<b>0.0</b>	<b>-0.1</b>	<b>-0.1</b>	<b>0.0</b>
50 °C	Exp	39.8	43.9	46.0	40.2	45.1	45.1	42.0	33.5	35.9	35.1
	Sim	39.7	43.9	46.2	40.3	45.1	45.1	42.0	33.2	35.7	35.0
	Diff	<b>-0.1**</b>	<b>0.0**</b>	<b>0.2</b>	<b>0.1</b>	<b>0.0</b>	<b>0.1</b>	<b>-0.1**</b>	<b>-0.3**</b>	<b>-0.2*</b>	<b>-0.1*</b>
55 °C	Exp	43.7	48.0	50.5	43.4	49.2	49.1	45.1	35.5	38.4	37.3
	Sim	43.4	47.8	50.7	43.5	49.5	49.5	45.3	34.7	37.8	37.0
	Diff	<b>-0.3**</b>	<b>-0.2**</b>	<b>0.2</b>	<b>0.1</b>	<b>0.4*</b>	<b>0.4*</b>	<b>0.2</b>	<b>-0.7**</b>	<b>-0.5*</b>	<b>-0.2*</b>

The resistance modifications helped keep the majority of temperature errors within the precision index of the thermocouples (0.2 °C), with a maximum error of 0.7 °C for the entire range of tests. Due to lack of foresight during the different testing periods, two major sources of error are still present in some measurements. The values denoted by a single asterisk (\*) are average measurements taken over multiple tests

due to the shortage of sensors. Values denoted with two asterisks (\*\*) represent individual tests where the ambient conditions in the lab were deemed significantly different. Some tests were affected by the air exchange in the room being turned off for several weeks during the summer months, allowing the stagnant air to become hot and humid. Another instance involved large warm air currents caused by other equipment running simultaneously in the lab. In both of these cases, the ambient conditions were altered which the model does not account for, unless the specific conditions are known. The environmental conditions primarily affect the outer exposed components such as the cover and baseplate. Despite errors caused by such environmental conditions, the steady-state temperature errors achieved in Table 5.10 are deemed quite acceptable.

Table 5.11 - Steady-state heat rates: experimental vs. simplified simulation

Run ↓		Rate of Heat Flow {mW}						
		$\dot{Q}_{obh}$	$\dot{Q}_{end}$	$\dot{Q}_{top}$	$\dot{Q}_{side}$	$\dot{Q}_{man}$	$\dot{Q}_{bp}$	$\dot{Q}_c$
30 °C	Exp	4.0	14.7	13.9	24.1	18.8	28.3	59.7
	Sim	4.2	14.9	13.8	25.6	19.3	29.3	63.7
	Diff	<b>0.2</b>	<b>0.2</b>	<b>0.0</b>	<b>1.5</b>	<b>0.6</b>	<b>1.0</b>	<b>4.0*</b>
37 °C	Exp	9.9	32.9	31.6	44.0	33.6	71.6	133.7
	Sim	10.1	33.5	32.3	44.7	33.7	67.0	136.7
	Diff	<b>0.2</b>	<b>0.6</b>	<b>0.7</b>	<b>0.7</b>	<b>0.1</b>	<b>-4.6</b>	<b>3.0</b>
45 °C	Exp	18.6	62.2	52.4	73.1	55.6	111.6	231.6
	Sim	19.0	60.5	53.9	76.2	57.4	116.2	234.0
	Diff	<b>0.4</b>	<b>-1.7</b>	<b>1.5</b>	<b>3.1</b>	<b>1.9</b>	<b>4.6</b>	<b>2.4</b>
50 °C	Exp	24.2	78.0	70.6	100.5	77.2	158.4	288.0
	Sim	25.9	77.1	67.4	104.3	78.6	150.0	297.2
	Diff	<b>1.7</b>	<b>-0.9**</b>	<b>-3.2</b>	<b>3.8</b>	<b>1.3</b>	<b>-8.4**</b>	<b>9.2*</b>
55 °C	Exp	34.8	95.1	84.0	122.8	92.3	182.0	401.0
	Sim	34.4	95.2	82.8	115.9	87.3	183.8	381.7
	Diff	<b>-0.3</b>	<b>0.1**</b>	<b>-1.2</b>	<b>-7.0*</b>	<b>-5.0*</b>	<b>1.8**</b>	<b>-19.3*</b>

Errors in the rate of heat flow at steady-state remain within 5% of the measured values with the majority falling well below that. The asterisks denote the same experimental issues as outlined for Table 5.10. It should be remarked that matching heat flow rates, more so than temperatures, represents a more sensitive measure of

model accuracy. The final steady-state model is shown in Figure 5.14. This is the resistance network that is used in the transient analysis covered next.

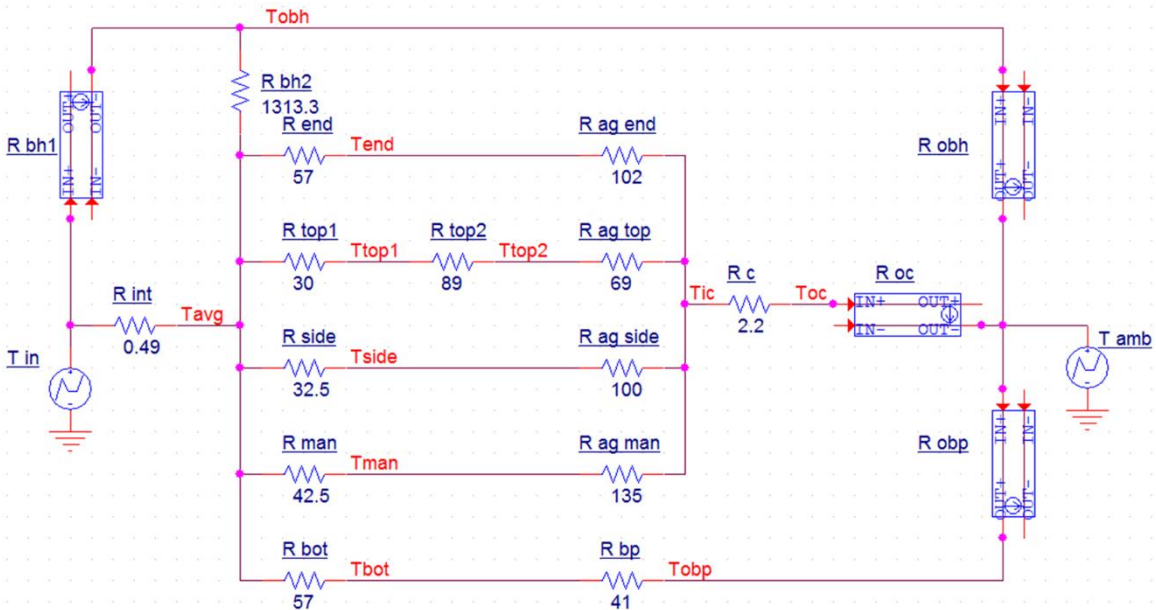


Figure 5.14 - Final reduced steady-state thermal network

### 5.3 DYNAMIC MODEL

The previous section detailed the methodology behind developing a resistance network that can mimic the steady-state temperature and heat flow for any particular component in the battery pack using fluid and ambient temperature inputs. The practicality of that type of model is limited but can be greatly improved by capturing the thermal dynamics of the system, which are introduced by modelling the thermal mass of each component in the form of capacitors. The methods of determining and implementing capacitors are discussed along with the addition of a more realistic heat source. The final lab-based dynamic model is then presented at the end of this section.

#### 5.3.1 Addition of Capacitors

In a thermal network where the resistors represent physical components, a capacitor represents the thermal mass (heat capacity) of a given component, which is appended

to its corresponding resistor. One end of the capacitor is connected to the resistor, and the other to ground. Capacitors charge up (components heat up) following a first-order system response and reach steady-state temperatures equal to those from the purely resistive network.

### ***Methodology***

The heat capacity of any object is obtained by multiplying its specific heat by its mass:

$$C = mc_p \quad (5.1)$$

Each component is weighed using a scale, and  $c_p$  is assigned based on known or published material properties. The component's individual mass is multiplied by the number of times the specific component appears in the battery pack assembly, representing the total mass ( $m$ ) of that component inside the battery pack. For example, the mass of each individual portion of the cell retention frame is multiplied by 144, which is the number of frames in the battery pack assembly. The circuit capacitor value is obtained by dividing  $C$  from Equation (5.1) by the number of cells (288); this calculates the "per cell" contribution of the component's thermal mass. Since the frame is a single piece divided into four paths, the mass of each portion is measured separately. The frame is hung from a scale and the desired section is submerged in water. The buoyancy of the submerged section reduces the force on the weigh scale. The mass of the submerged section is calculated as follows:

$$\text{mass of section} = (\text{change in scale reading}) * \frac{\text{density of object}}{\text{density of water}} \quad (5.2)$$

A capacitor is added to all resistors that represent physical components of the battery pack. The variable ambient resistors  $R_{obh}$ ,  $R_{oc}$ , and  $R_{obp}$  do not have associated capacitors since they are a part of the environment which is considered an infinite sink. Each capacitor's initial voltage must be set to that particular component's starting temperature; this defines the initial conditions for the simulation.

The capacitor values are validated by comparing the transient behaviour of the simulations to the experiments. Temperature and heat flow measurements are compared and the results are discussed in Section 5.5.

### 5.3.2 Modelling of a More Realistic Heat Source

Thus far, an ideal voltage source has been used as the input heat source from the fluid, which in PSpice is capable of outputting nearly infinite current in order to maintain the voltage set point. In reality, a standard power supply has a current limit that is dependent on the output voltage. Voltage sources in PSpice do not have a current (or power) limit parameter, warranting the need for another solution. One common method is to build a transistor-based current-limiting circuit that is tuned for a specific limit. Yu and Yuvarajan used this type of current limiter to mimic the effects of concentration polarization in their model of a fuel cell [98].

Jokinen and Saari [99] discussed the modelling of a coolant source using a heat flow-controlled temperature-source, which is analogous to a current-controlled voltage-source. The temperature value of the source is the coolant temperature, and the current limit is defined by the governing heat flow balance equations. They also discussed the determination of the source resistor ( $R_{int}$  in the case of this thesis), and noted that the second temperature (value after the resistor) can be approximated by the mean fluid temperature (taken between inlet and outlet) for small temperature differences. However they did not discuss how to directly implement the source. The approach utilized here, was to employ a voltage-controlled current-source (GVALUE component in PSpice) and a shunt resistor.

In normal operation, the GVALUE component reads the voltage drop across the shunt resistor and outputs the required current using Ohm's law. The current limit is set using the built-in lookup table function which linearly interpolates between the defined points, and if a limit is exceeded, the limit value is assumed. This way, hard limits for heating and cooling can be defined independently.

To simulate the behaviour of the fluid system in the lab, the current limit must be dependent on the temperature and flowrate of the fluid. The following relation is used to define the heating limit  $\dot{Q}_{max}$  based on the experimental test setup:

$$\dot{Q}_{max} = \dot{m}c_p(T_{in} - T_{amb}) = \rho\dot{V}c_p(T_{in} - T_{amb}) \quad (5.3)$$

Due to the nature of the tests, the fluid temperature cannot go below ambient, which defines the maximum  $\Delta T$  of the fluid. This relation is programmed into the GVALUE lookup table using fluid flowrate as an input into PSpice. The current limit responds dynamically with respect to fluid flow, inlet fluid temperature, and ambient temperature. Figure 5.15 compares the current limit (dashed lines) defined by Equation (5.3) to the measured heat flowing into the pack (solid lines) with 45 °C inlet fluid at the listed flowrates. The experimental input current (heat rate) is measured using the mass flowrate of the fluid and the temperature difference between inlet and outlet.

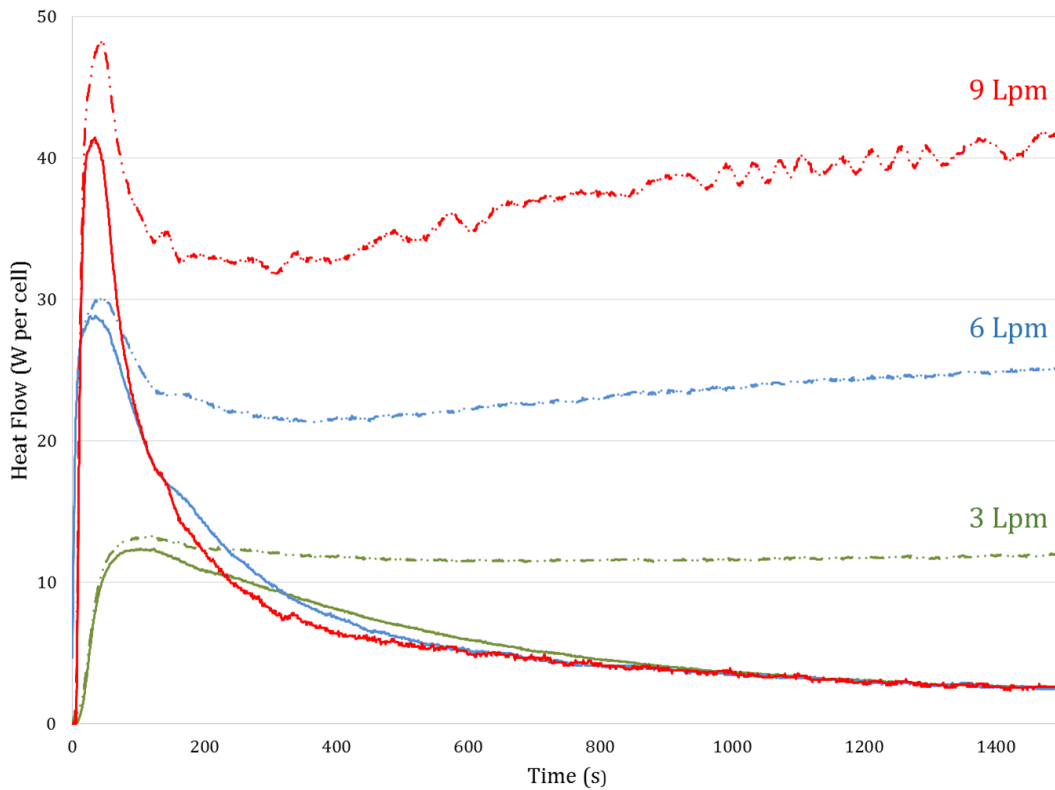


Figure 5.15 - Heat flow limit (W per cell) vs. input heat flow at 3, 6, and 9 Lpm

The rate of heat flowing into the pack during the initial period of the test varies greatly with flowrate. At low flow, the heating capability of the fluid is saturated for a longer period of time since the maximum heating power is reduced. At 9 Lpm, the maximum heating capacity of the circulating fluid is approached but never reached. This indicates that a current limit is only necessary for flowrates under 9 Lpm. For a fluid system where the heating/cooling input power is absolutely known, the level of heating or cooling available to the fluid in {W} would be set as the current limit. An example of the latter is an electric immersion heater embedded directly inside the pack's manifold.

### 5.3.3 Tuning of Interior Capacitor

The lumped capacitor  $C_{int}$  which represents the thermal mass of the interior of the modules, is the last component to be tuned in the thermal network. It is made up of cells, cooling plates, foam inserts, internal endplates, and fluid. In the original model (Figure 4.2), these capacitances are represented by  $C1$ ,  $C2$ , and  $C2^*$  which make up the thermal mass in "Section A"; the true heat capacity values of these components are to be determined through experiments being carried out by another student and will not be discussed here.

For the completion of this work, the value of  $C_{int}$  is manually tuned to achieve the correct system response. During the initial heating period, the majority of the heat is absorbed by the inner modules and little heat yet flows out through the frames; this is the response period that is used to tune  $C_{int}$ . As discussed in Section 3.3, it is common practice to extract RC parameters for complex geometries by minimizing the error in the system response. In this case, the value of  $C_{int}$  is manually modified in the PSpice environment until the simulation response matches the input heat flow profile (i.e. error is minimized). This is done manually for simplicity, rather than using an optimization algorithm since it is only a single value, and the process can be done rather quickly.

The original estimate of the cell thermal capacitance (main contributor to  $C_{int}$ ) was approximately 338 J/°C at room temperature, establishing a starting point for the tuning process. The lumped internal capacitance value  $C_{int}$  was determined to be approximately 450 J/°C using the aforementioned calibration technique. It is important to note that the heat capacity of a Li-ion cell is dependent on both temperature and state of charge [100], and that this phenomena is not captured by this model. In practice, recent finding by others have shown that C value of the cells rise appreciably with temperature [100].

Figure 5.16 compares the input heat flow profiles along with the absolute error during the first 600 s of a 9 Lpm @ 45 °C test.

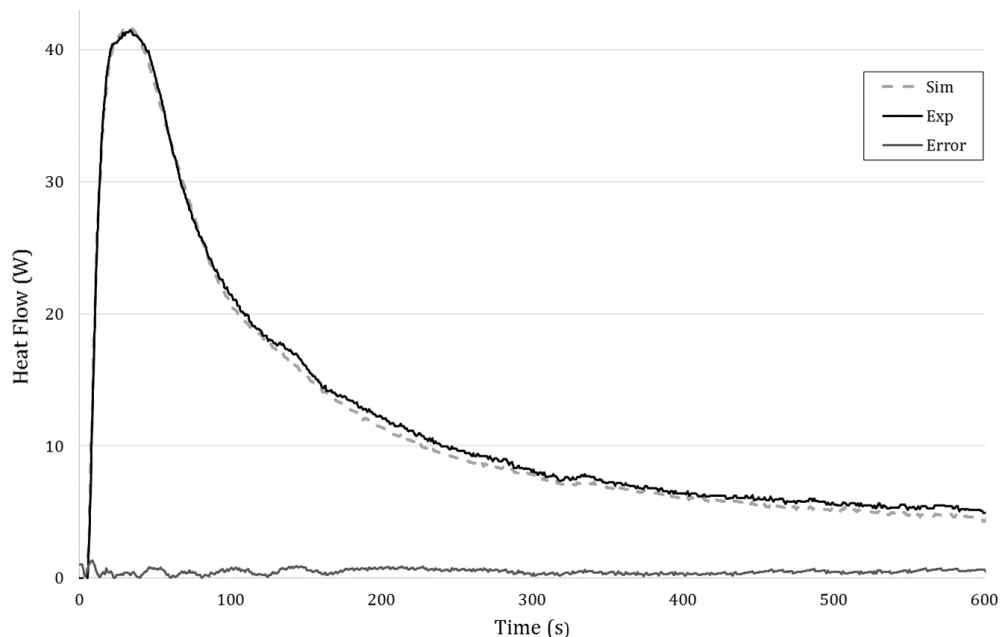


Figure 5.16 - Input heat rate: experimental vs simulation

9 Lpm is chosen as the flowrate since it does not require current limiting which itself has some inherent error. The simulation profile matches extremely well lying within 2% over the majority of the curve during the first 10 minutes. This indicates that the model is receiving the correct amount of heat at the beginning, which verifies the lumped capacitor is appropriate for the system as tested. The only drawback is that the capacitance and resistance of the cell are lumped with the components in its

immediate vicinity; hence “Section A” details in the original model (Figure 4.2) remain obfuscated.

## 5.4 SUMMARY AND FINAL LAYOUT

Thus far, thermal resistance values determined from temperature and heat flux measurements were assembled into a purely-resistive thermal network which accurately predicted steady-state temperature and heat flow for all components in the lab setting. Variable ambient resistances were implemented to account for changes in heat transfer due to the temperature differential between the battery pack and the room, which improved the accuracy of the model over a wider range of conditions. Capacitor values were determined and introduced to their respective resistors to provide the model with dynamics, and a heat limiting source model is included to account for changes in fluid flowrate and inlet temperature. The resulting thermal network shown in Figure 5.17 includes all of the features discussed and is considered to be the final laboratory model.

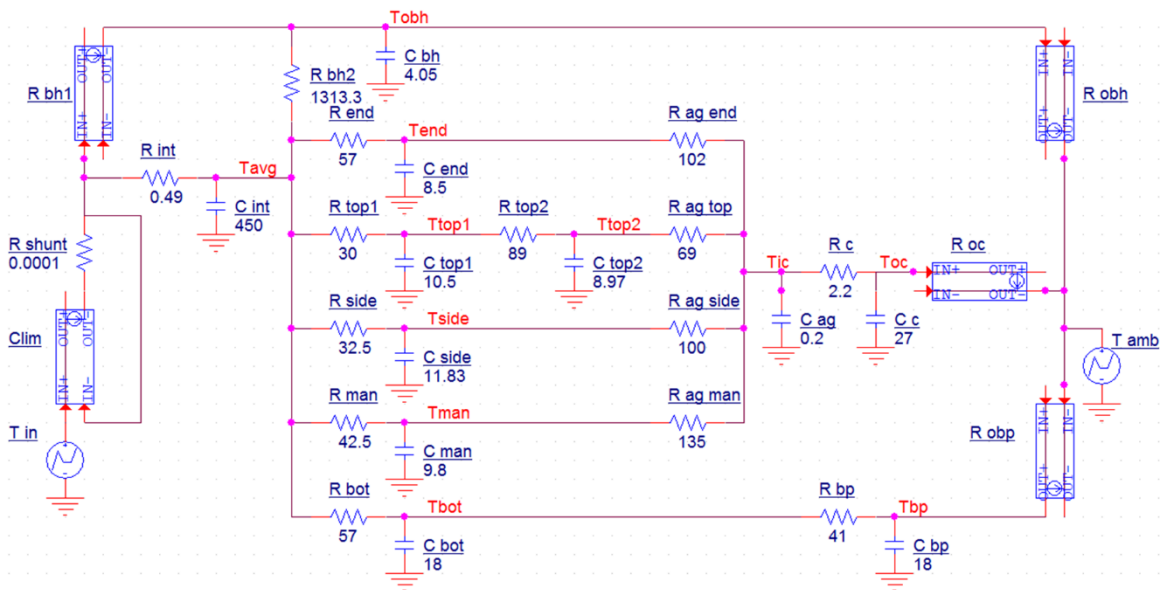


Figure 5.17 - Final transient lab model

## 5.5 RESULTS

The validity of the full laboratory model is tested by comparing the PSpice simulation results to experimental data derived under the same conditions. The temperature and heat flow responses are compared both visually and numerically, and the resulting errors are discussed. The section is concluded with a discussion on some insights gained during this process.

### 5.5.1 Simulation Validation

To relate the simulation to the experiments as accurately as possible, only tests with full sets of measurements are utilized for comparison. Any measurements denoted with asterisks in Table 5.10 and Table 5.11 are not used in the analysis since they are a result of combining multiple days of testing together. Differences in ambient temperature, starting temperatures, fluid bench behaviour, and air currents between testing days would introduce errors into the measurements. However, there are enough full test points to allow for a fair assessment of the model's performance. The measured ambient temperature ( $T_{amb}$ ) and inlet fluid temperature ( $T_{in}$ ) constitute the external conditions experienced by the battery pack. Simulations are run separately for every test with the correct external temperatures used as inputs. For demonstrative purposes, the set of tests run at 45 °C fluid temperature are compared in the body of the thesis and the other testing temperature results can be found in Appendix B.

#### 5.5.1.1 Temperature

The temperature profiles are separated into three plots (Figure 5.18 - Figure 5.20) in order to make visualization easier. Only the initial 7000 s are plotted since this covers the majority of the transient period of the test run. Most components have reached steady-state by this time but components that are more massive or farther away from the heat source are only at the cusp of steady-state.

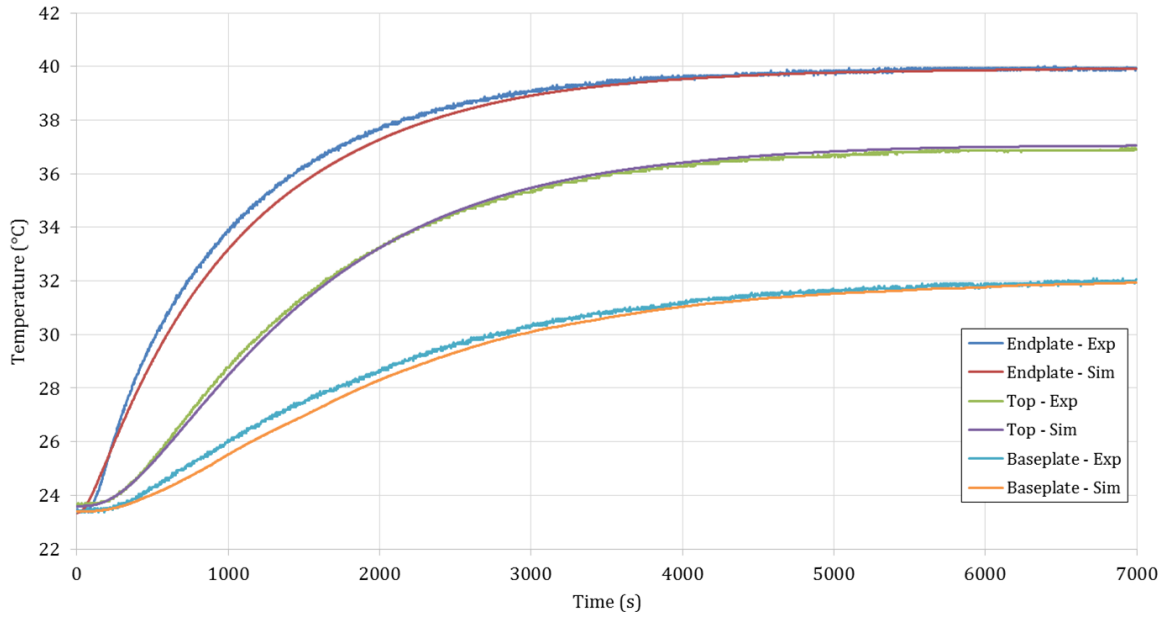


Figure 5.18 - Simulated vs. measured temperatures: endplate, top, and baseplate

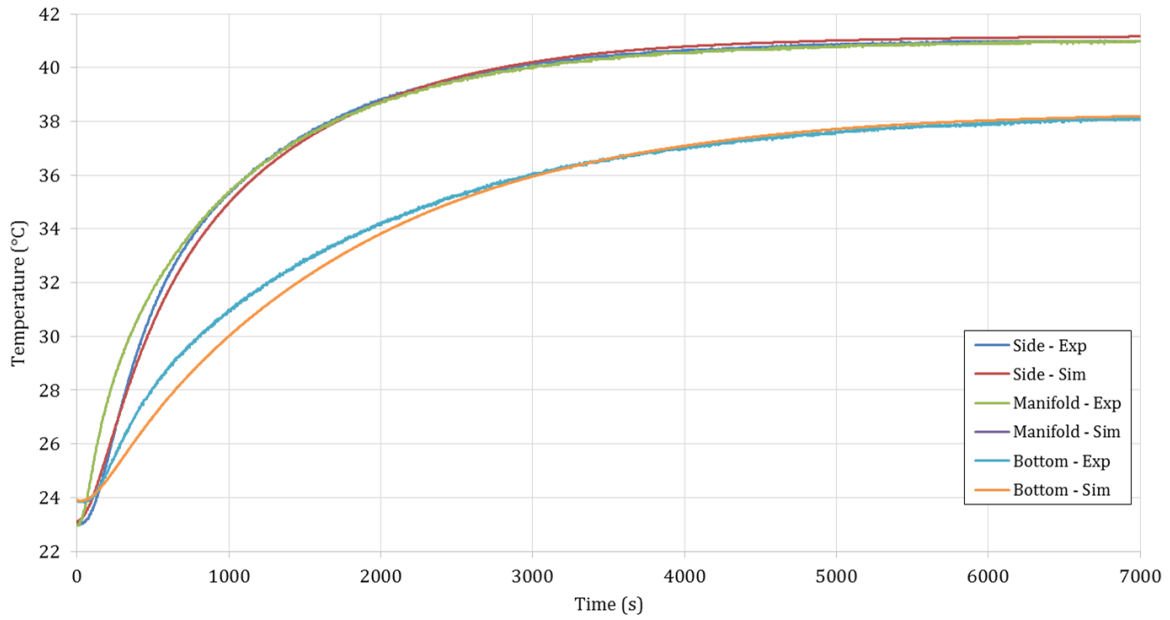


Figure 5.19 - Simulated vs. measured temperatures: side and manifold

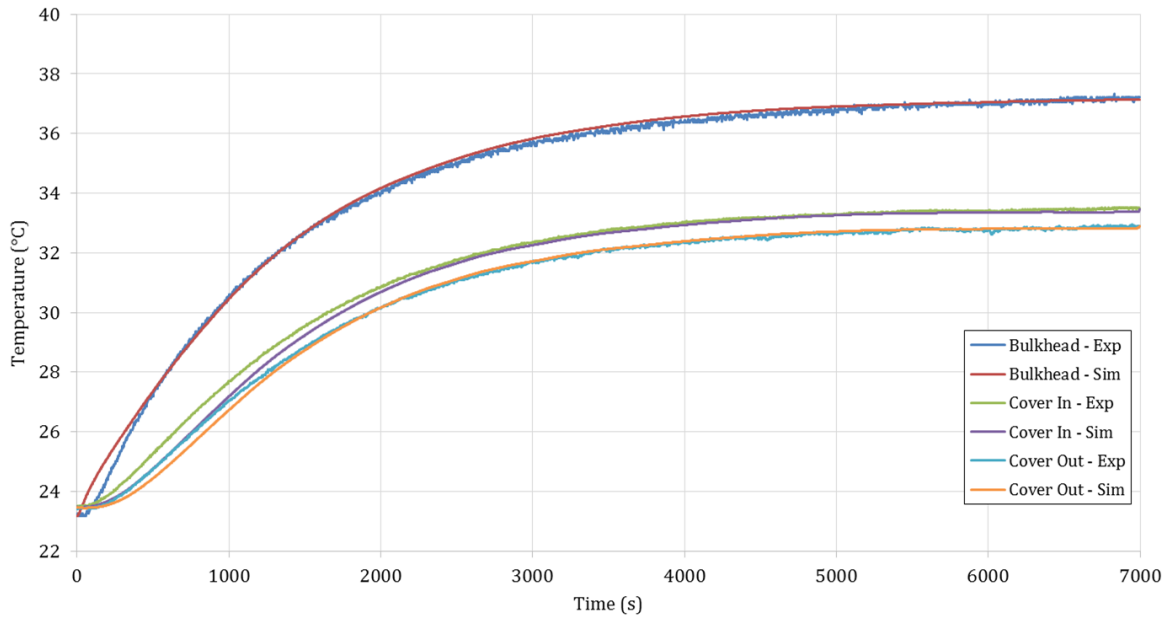


Figure 5.20 - Simulated vs. measured temperatures: bulkhead, inside cover, and outside cover

The temperature errors from the three previous figures are summarized in Table 5.12 in the form of absolute maximum error, RMS error {°C}, and RMS error as a percent of temperature rise. Maximum absolute error of 1.5 °C, and RMS error of 0.5 °C are targets established based on the performance of other similar experimental thermal network models [89] and anything below this value is deemed acceptable.

The RMS value aims to represent the “average” error in {°C} over the transient period. Here, the “transient period” is defined as the time elapsed up until the fifth time constant ( $5\tau$ ); where  $1\tau$  is defined as the time required to reach 63.2% of total temperature rise. After  $5\tau$ , the temperature will have risen to  $\sim 99.4\%$  of its final value, which is considered to be the point when steady-state begins. The benefit to this approach is that each component has a different transient period over which the RMS error is calculated. This way, the RMS error is weighed equally amongst all components, and decreases in RMS error caused by the steady-state are not present.

It is very common in the literature to “overstate” the accuracy of results by presenting temperature errors as a percent of an absolute value. A more appropriate method is to express the error as a percent of temperature change experienced during the test.

In this case, Equation (5.4) is used to compare RMS error in relation total temperature change.

$$RMS \{ \% \Delta T \} = 100 * \frac{RMS \{ ^\circ C \}}{T_{steady-state} - T_{initial}} \quad (5.4)$$

Table 5.12 - Absolute maximum and RMS errors in temperature during transient heating

<b>Component ↓</b>	<b>Absolute Max Error {°C}</b>	<b>RMS Error {°C}</b>	<b>RMS Error {% ΔT}</b>
<b>Endplate</b>	0.87	0.39	2.4
<b>Top</b>	0.36	0.14	1.0
<b>Side</b>	0.60	0.23	1.3
<b>Manifold</b>	2.30	0.60	4.2
<b>Bottom</b>	1.17	0.42	3.0
<b>Baseplate</b>	0.65	0.26	3.0
<b>Bulkhead</b>	0.87	0.18	1.3
<b>Inside Cover</b>	0.59	0.22	2.2
<b>Outside Cover</b>	0.39	0.12	1.3

Most components lie well below the maximum absolute limit of acceptance, with the manifold being the only outlier. The majority of RMS errors also lie within a reasonable limit of 0.5 °C, except for the manifold. In terms of percent error, values lie well below 5% including the manifold. Errors in the other full set of measurements (37 °C) are slightly lower in magnitude due to the lower temperature span but are nonetheless comparable to the figures presented here.

Too much or not enough lag during the initial minutes of the test causes large errors during the heating period, which is where the maximum errors occur. The amount of lag experienced at any node in the network is affected by the components that precede it. Once a component begins to heat up, its own capacitor dictates the response and capacitors down the line begin to affect the behaviour once the rate of heating starts to decrease. The simplification of the complex construction within the inner workings of the modules (“Section A”) into a single resistor and capacitor constitutes the main source of error at the beginning of the simulation. This forces all of the components to behave similarly in the initial minutes, which in reality is not exactly the case. The amount of heat flowing into each section of the frames differs based on geometry which is not accounted for in the single lumped capacitor and

resistor. The manifold is affected the most by this approximation since it is primarily in contact with the fluid rather than physical hardware such as the cooling plates, cells, and frames. Nonetheless, these simulation results are deemed acceptable since the errors are more likely caused by such simplifications rather than the detailed scope of work presented.

### 5.5.1.2 Heat Flow

The same procedures are followed to compare simulated heat flow to experimental data. The profiles are also separated into three figures for ease of visualization. It is clear from the plots of Figures Figure 5.21 - Figure 5.23 that the heat flux sensors have greater fluctuations than the thermocouples, especially on the outer surfaces such as the baseplate, cover, and bulkhead.

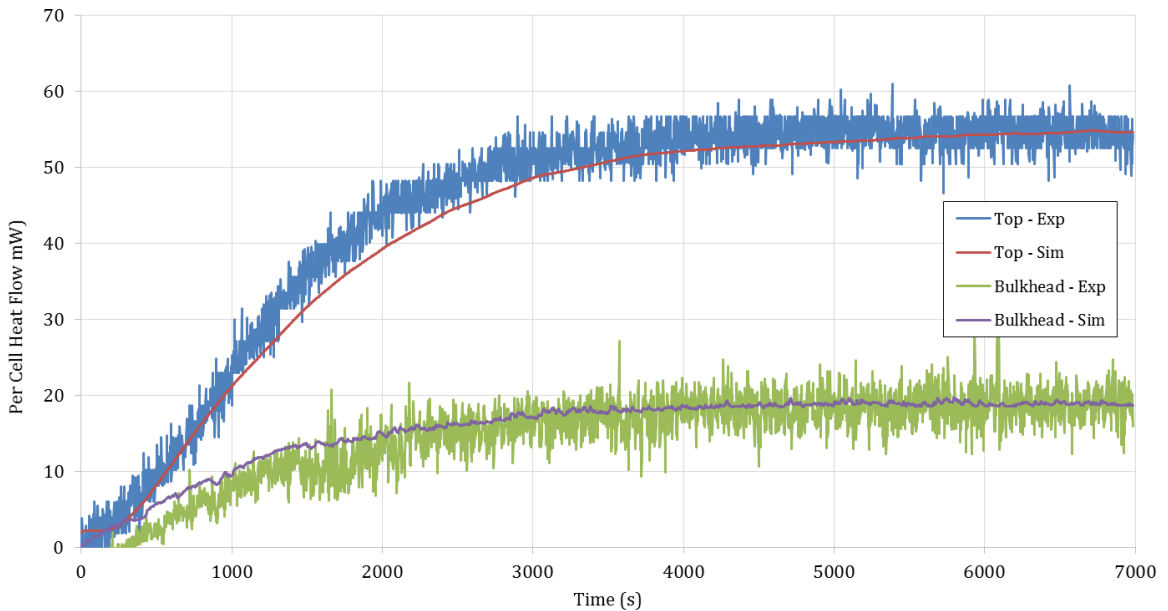


Figure 5.21 - Simulated vs. measured heat flow: top and bulkhead

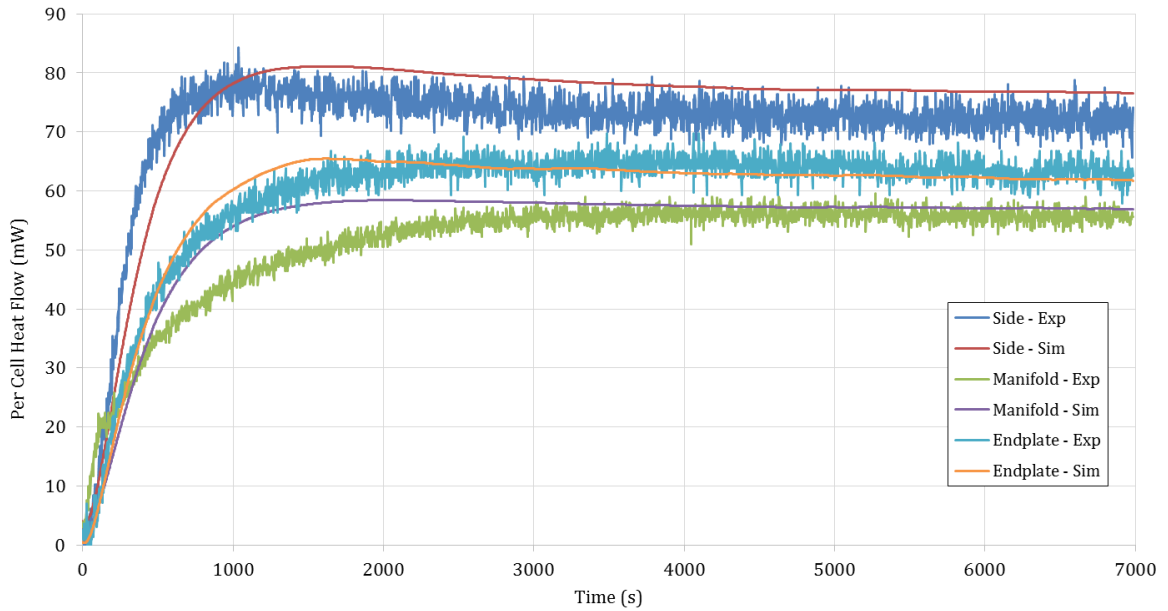


Figure 5.22 - Simulated vs. measured heat flow: side, manifold, and endplate

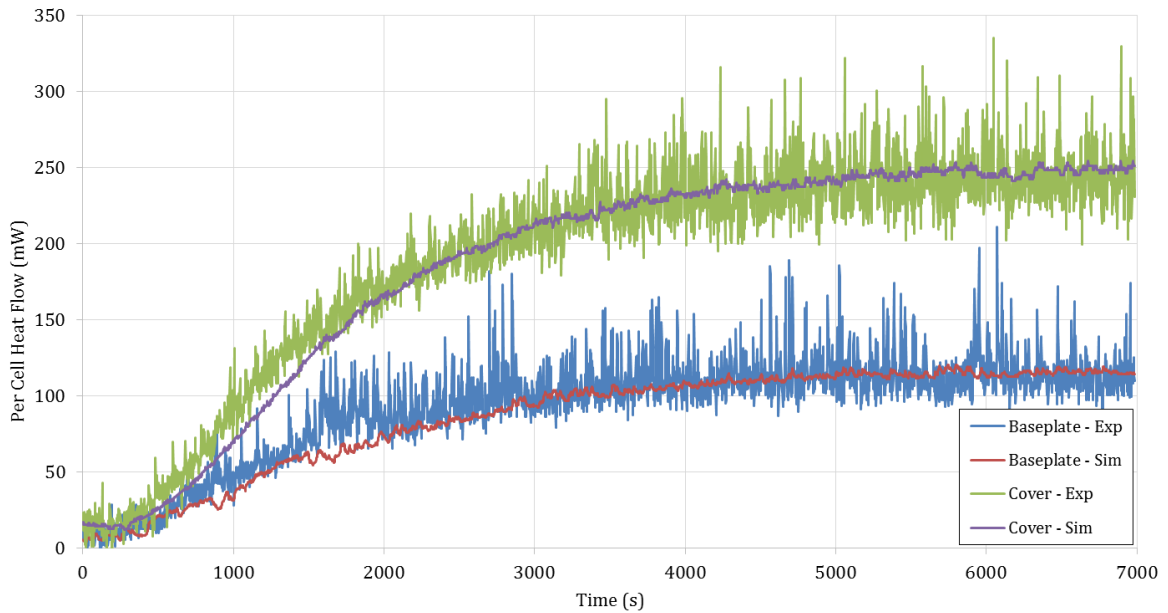


Figure 5.23 - Simulated vs. measured heat flow: baseplate and cover

The absolute maximum and RMS errors are shown in Table 5.13. The error values are highly influenced by the level of apparent sensor noise which gives a falsely high impression. No “acceptable” range of heat flow accuracy has been established from the literature since the main focus is always temperature without acknowledgement of heat flow. The results shown were visually inspected to assess the model’s

performance, with the values from Table 5.13 being used as confirmation. The level of measurement signal noise is included for comparison purposes.

Table 5.13 - Absolute maximum and RMS errors in heat flow during transient heating and signal noise levels

<b>Component ↓</b>	<b>Max absolute error (mW)</b>	<b>RMS Error (mW)</b>	<b>Signal Noise (mW)</b>
<b>Endplate</b>	8.61	2.47	1.15
<b>Top</b>	9.94	3.05	1.99
<b>Side</b>	15.69	5.43	1.96
<b>Manifold</b>	15.44	4.64	1.09
<b>Baseplate</b>	97.66	15.98	14.33
<b>Bulkhead</b>	13.44	2.65	2.32
<b>Cover</b>	88.68	16.88	18.24

Inspection reveals that the simulated heat rates do represent the experimental measurements fairly accurately. The discrepancies at the beginning of the tests arise from differences in initial conditions between the experiment and simulation. The bulkhead for example is in close proximity to the hot fluid reservoir of the test bench, which radiates heat into the bulkhead, resulting in a negative experimental heat flow at the beginning. These errors do not have a significant effect on the overall response and are thus seen as negligible.

There is a relatively high level of environmentally-caused fluctuation on exposed surfaces (cover and baseplate) due to mild forced convection currents caused by the lab HVAC system and other natural convection disturbances arising. Convection heat transfer increases with temperature difference, and as a result, so does the level of convection-induced fluctuation in the heat flux measurement signal. Additionally, horizontal surfaces with cooler air beneath are more susceptible to variations caused by air disturbances from the surroundings. As someone walks near the battery pack, the relatively stagnant pocket of warm air under the baseplate is disturbed by the oncoming cool air currents, temporarily increasing the heat flux reading. This results in larger calculated error values, but as shown in Table 5.13, the RMS error values are comparable to the level of signal variation and are therefore still deemed acceptable due to the nature of the measurement background.

The manifold exhibits a laggard time response, in practice due to its greater local capacitance not being captured by the simplification of the inner components of the modules. For the same reasons stated earlier, this discrepancy is still deemed acceptable for the purposes of this endeavour.

## **5.6 SUMMARY AND CONCLUSIONS**

### **5.6.1 Summary**

A goal of the lab work was to provide a thermal network that accurately describes the dynamic temperature and heat flow for the components outward from the modules; while the work of another student in the research group is to characterize the heat transfer of the innards of these modules. An experimental setup was devised to uncover the thermal properties and characteristics of the battery pack using temperature and heat flux measurements. A resistance framework was developed and verified based on steady-state measurements taken during a series of  $\sim 105$  tests conducted over a period of 14 months. Capacitors were added to the network to create a transient model, which was shown to be accurate considering the simplifications made in the process. The simulation is most accurate after approximately 500 s when the thermal mass of the exterior portion of the modules yields the greatest influence. This shows that the method presented is sound. Once the lumped components  $R_{int}$  and  $C_{int}$  are replaced by the thermal network representing the interior of the modules, the initial transient behaviour is expected to improve significantly. A unique method of representing variable resistances and the modelling of a current limited heat source were also introduced to improve the robustness of the simulation.

### **5.6.2 Recommendations**

The nature of the experiments performed called for multiple days of testing to produce a single set of measurements. Lumping multiple components into a single resistor and capacitor (manifold, sides, and cover) requires an average temperature

profile to be measured which is only accurate for the specific ambient conditions during that test. It is important to capture the average correctly in a single test in order to prevent difficulties while processing the data. Many measurement errors could have been reduced by ensuring other surrounding equipment (with integrated cooling fans) remained off during the testing period. This often affected the cover, bulkhead, and baseplate measurements which had to be omitted during the analysis. Taking redundant measurements helped mitigate this problem but due to a limited number of sensors, some errors remained in the data set.

### **5.6.3 Conclusions**

The laboratory model mimics the thermal behaviour of a stationary battery pack in a relatively constant environment (lab). This type of model can be useful in analyzing the physical construction of the battery pack in isolation from the effects of a vehicle. Heat soaks can be used to analyze low resistance paths, and the influence of potential structural design changes can be assessed rather quickly. This model is modified in the next chapter allowing it to mimic the battery pack's thermal behaviour while mounted to the vehicle.

## 6 THERMAL MODEL ADAPTATION TO THE FULL VEHICLE

---

### 6.1 INTRODUCTION

#### *Intent*

Extending the functionality of the existing battery pack thermal model to better represent the environmental conditions present on a real vehicle is required. This allows for progressing to the full vehicle simulation with confidence.

In the lab, the only heat sink present is the room in which the experiments are conducted, and heat is transferred mainly through natural convection and radiation. This is a limited case that must be expanded upon in order to improve the functionality and robustness of the thermal model. On the production vehicle, the battery pack is fastened through the baseplate to the underbody along the vehicle's centreline. Everything above the baseplate (i.e. cover and cell modules) is situated inside of a central cavity in the vehicle's chassis. As a result of this construction, the baseplate experiences convection currents from the wind and due to the vehicle being in motion. In addition, radiation from the road is also absorbed by the baseplate. The front bulkhead of the battery pack is located behind the engine, and the top cover is separated from the chassis by a small airgap. This emplacement results in four environmental conditions (sources and variable resistances) that were assessed through a series of road tests and inserted in place of  $T_{amb}$ ,  $R_{oc}$ ,  $R_{obp}$ , and  $R_{obh}$  from the model developed in the previous chapters.

#### *Objectives*

The following goals were set for the vehicle battery pack thermal model:

- The appropriate external sources should be included in the thermal network
- The model should adapt dynamically to environmental conditions such as vehicle speed, wind speed, and road radiation

- Results should be verifiable using road testing data

### ***Road Testing***

The thermal conditions experienced by the battery pack in real world driving were relatively unknown at the beginning of this work and thus a series of road tests were conducted to capture these conditions. The tests were conducted over a period of four days on a rented vehicle during the month of August 2015. Heat flux sensors and thermocouples were installed where possible, and the vehicle's CAN bus was monitored to provide data such as vehicle speed and battery pack coolant temperature. Several different driving scenarios were created to expand the range of data collection. These road tests are discussed in greater detail in Section 6.3.2.

## **6.2 AIRFLOW MEASUREMENT**

One of the major differences between the battery pack in the lab and on the vehicle is motion, hence the need for air velocity measurements. This section describes the process of selecting and employing air speed sensors to analyze the convection under the vehicle during normal operation. The implementation of the sensors is discussed later in Section 6.3.

### **6.2.1 Requirements and sensor selection**

Measuring air speed under the baseplate, which is situated between the road and the vehicle's underbody, requires a sensor that can handle extreme conditions. The sensor should be able to withstand fluctuating temperatures, road dust, small debris, and water. The sensor should be accurate over the entire air speed range that exists under the baseplate during normal driving conditions. The sensor should also be easily mountable in tight locations and remain secure over long distances in order to successfully measure air flow under the baseplate and in other difficult to access locations. The original intended purpose was to understand the airflow characteristics around the entire battery pack. This includes crosswind effects and

local convection currents around the bulkhead, cover, and baseplate. Air velocities around the more sheltered components (bulkhead and cover) are assumed to be relatively low, requiring adequate low-speed calibration. Due to test vehicle limitations however, air flow under the baseplate is the main are of focus.

Traditionally, air speed measurements are taken in wind tunnels using devices such as pitot tubes, vane anemometers or hot-wire anemometers [101], [102]. Handheld pitot tubes and vane anemometers are convenient and easy to use in a wind tunnel, but are cumbersome and costly to mount under a vehicle for road testing. Hot-wire anemometers are much smaller and easier to place in multiple locations but are extremely fragile due to the very thin wire used as the sensing element. Hot-film anemometers are similar to hot-wires in operation but are more physically robust since the sensing “wire” is deposited onto a substrate rather than being fully exposed. These sensors are the most practical for the purpose of measuring underbody air speeds during road tests with unknown conditions.

### **6.2.2 Hot-film Anemometer Operation and Circuit Implementation**

Thermal type anemometers (hot-wire and hot-film) use the change in convective heat transfer between the fluid medium and the sensor to determine the fluid’s velocity. A current passes through a conductor of known properties, which heats up due to its internal resistance. An electrical circuit is used to compensate for the loss of heat of the conductor due to convection, and provides the measurement signal. The two most common compensation methods are constant temperature and constant current. In a constant current anemometer (CCA), the electrical current is held constant by the compensation circuit. As air flows over the wire, its temperature and resistance change. The change in voltage required to keep a constant current becomes the measurement signal. In a constant temperature anemometer (CTA), the compensation circuit aims to keep the wire’s resistance, and thus temperature, constant by varying the current passing through the wire. The voltage required to keep a constant temperature is the measurement signal.

Thermal anemometers are great for measuring fluctuating velocities and turbulence due to their fast time response, and are convenient for taking point measurements. One of the main issues with operating thermal anemometers in either CTA or CCA modes is the dependence on fluid temperature. In both cases, the sensors need to be calibrated at their operating temperature, which is not practical for use in road tests where environmental temperatures are unknown and fluctuate significantly. Several different methods of temperature compensation have been developed [103]–[105] for thermal anemometers but a simpler approach was desired.

A slightly different type of thermal anemometer was selected for the purposes of this work. The chosen device was the FS5 thermal mass flowmeter from Innovative Sensor Technology, which is a constant temperature difference (CTD) hot-film anemometer [106]. This CTD anemometer maintains a constant temperature difference between the hot wire and the base of the sensor by the means of an electronic circuit. The sensor signal is the voltage required to maintain the set temperature difference which is independent of fluid temperature. The left side of Figure 6.1 depicts the sensor's electrical structure, and the right side shows the relative size of an FS5 sensor. The heater (hot wire) and the RTD are essentially two resistive film patterns that are deposited onto a ceramic substrate as shown below.

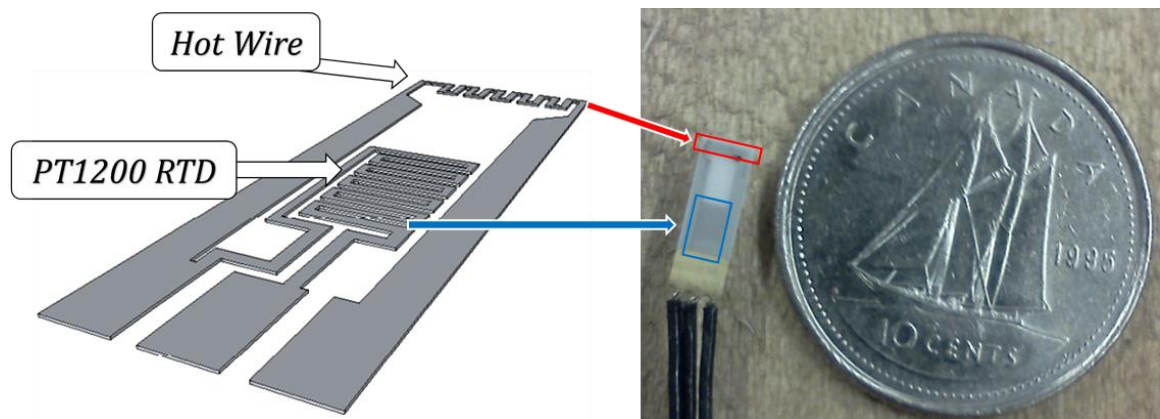


Figure 6.1 - Hot-film airflow sensor construction [106] (left) and sensor with size comparison (right) Current is sent through the hot wire located at the tip, which heats up the sensor and the built-in PT1200 RTD (1200  $\Omega$  platinum RTD) measures the temperature at the

base of the ceramic substrate. The positive and negative (common junction) sides of each resistor is connected to a compensation circuit, which is available for purchase from the sensor manufacturer. Each sensor requires one circuit board module to operate. This becomes costly when multiple sensors are required. As a result, a custom circuit board was designed and assembled based on the sensor manufacturer's published schematics for a recommended compensation circuit. The left side of Figure 6.2 shows one of the manufacturer's recommended compensation circuits for the FS5 sensor, and a physical representation of the circuit is shown on the right in the form of a custom designed board.

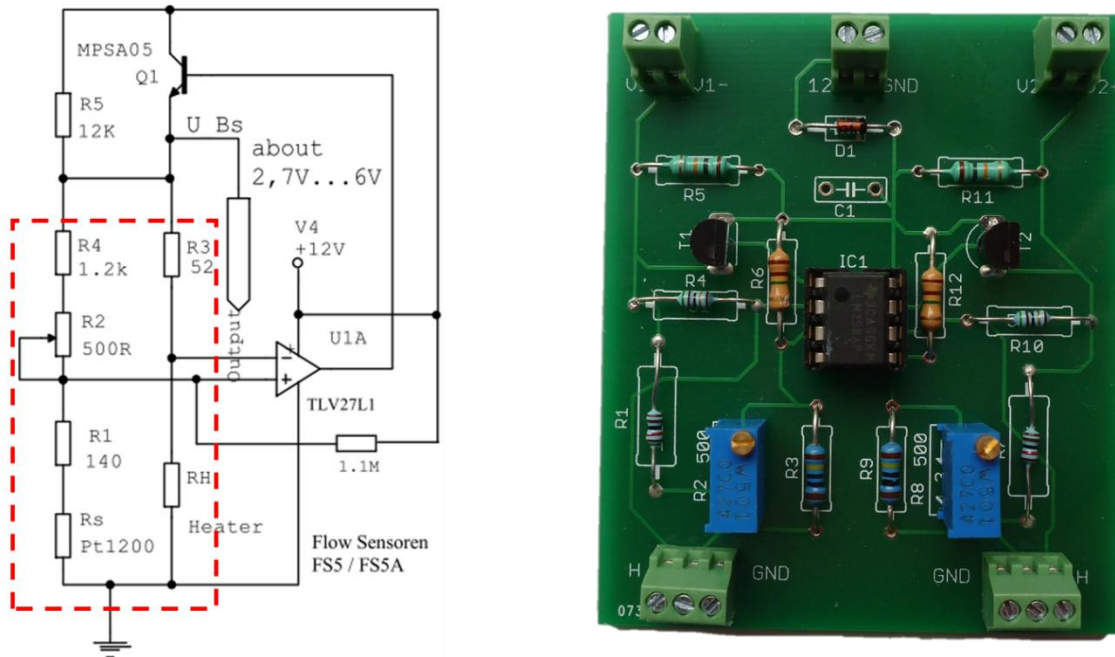


Figure 6.2 - Manufacturer recommended circuit for FS5 [106] (left) and custom sensor board (right)

The circuit has two parallel resistance branches. The first branch inside the dashed outline on the left side of the schematic is the temperature sensor branch, which begins at R4 and ends at the RTD (Rs). The second branch is the heater branch, which begins at R3 and ends at RH (hot wire). The operation amplifier (op-amp) U1A monitors the voltage difference between both branches, which represents the temperature difference between the heater and the RTD. The output of the op-amp feeds into the base of the NPN transistor Q1, which sends current to the heater. As air

flows over the sensor, the RTD's resistance decreases, which increases the voltage output of the op-amp, thus also increasing the current output of the transistor. This sends more current through the heater relative to the RTD, thus increasing the temperature at the tip of the sensor where the heater is located. This feedback loop establishes an equilibrium between the two resistance branches. The voltage at the emitter of the transistor is output and recorded. It indirectly indicates the amount of heat required to keep a constant temperature difference and is used for air speed calibration. The potentiometer R2 is used to set the baseline voltage output which also represents the temperature difference between the two branches. Que et al. investigated a very similar type of sensor and have claimed to reduce the error caused by varying air temperatures from 30% down to only 2% [107].

The circuit boards were created based on the manufacturer's circuit using an IC containing two separate op-amps. This allows two sensors to be connected to a single board which is roughly the size of a credit card. The cost of custom circuit boards with all components was low enough to allow multiple units and sidestep financial limitations. Resistors with low tolerances (temperature and resistance) were selected to reduce any differences between boards and changes caused by fluctuations in temperature. A diode was included at the power input in order to prevent damage to the op-amp and sensor due to reverse polarity, and a capacitor was added to filter input voltage noise (absent in Figure 6.2). The circuit boards were double layered with the bottom layer of acting as a ground plane. This reduces the complexity of the traces, allows for higher currents, and shields the circuit from electrical noise. The boards were designed to be connected to a vehicle's 12 V power system via a lighter receptacle plug. Many boards may be connected in parallel from a single 12 V plug since the current draw is minimal ( $\sim 200$  mA per 2 sensors).

### **6.2.3 Hot-film Anemometer Calibration**

Thermal anemometers require calibration since their response is dependent on the compensation circuit being utilized. The general procedure is to run the sensor inside a wind tunnel over a range of air speeds, and matching the output voltage to air

velocity. For this purpose, a low-cost, 2.5 m long, open-ended benchtop wind tunnel was constructed using a yard leaf blower that pulled air through 89 mm diameter ducting, which was controlled by a variable DC power supply capable of outputting 60 V. The intent was to construct an inexpensive wind tunnel suitable for calibration of the purchased airflow sensors. Figure 6.3 depicts the basic setup of the calibration tunnel, including direction of air flow and sensor positioning,

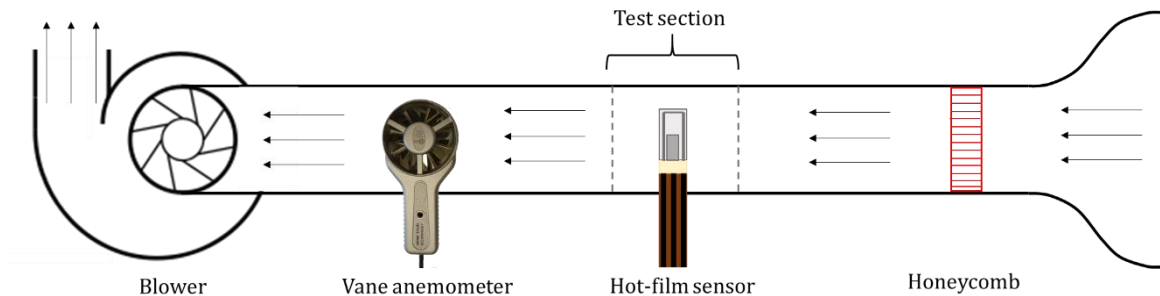


Figure 6.3 - Calibration tunnel setup (not to scale)

Basic design criteria for low speed wind tunnels as outlined by Bradshaw and Pankhurst [108] were considered during the process. A bell-shaped opening and honeycomb were installed at the entrance of the tunnel in order to improve airflow quality. The honeycomb was constructed from plastic straws and had a depth of approximately 6 times the diameter of each straw in order to reduce lateral velocity variations. A diffuser was also installed on the exit to help improve the efficiency of the blower. A transparent test section, located approximately 1 m from the entrance, was created by replacing a section of aluminum ducting with clear plastic. Slits were cut into the plastic which served as a means to insert the sensors and secure them in place. A calibrated handheld vane anemometer (Extech SDL300) was placed at the centre of the tunnel downwind from the test section in order to capture the mean air velocity. A calibrated handheld pitot tube was initially considered as the reference meter but due to its inaccuracy below  $\sim 3$  m/s and its high directional sensitivity, it was replaced by the vane anemometer. This calibration setup resembled the one used by Ardekani and Farhani [109] which they used to calibrate a hot-film anemometer based on a reference thermal mass flowmeter.

The sensor leads were connected to the circuit board via screw terminals, and the board was powered from a separate supply set to mimic the vehicle's 12 V system. An excitation voltage of 12.6 V was chosen based on road testing; this is different than the ~14 V from a conventional vehicle and will be detailed later. The circuit board voltage outputs were monitored in real time using an IPEtronik M-SENS block along with its IPEmotion software. The voltage to the blower was monitored with a digital multi-meter. The handheld vane anemometer was also monitored visually (digital display), and the values were simultaneously recorded onto an SD card using the software that came with the meter.

The airflow sensor calibration runs were conducted as follows:

- Ensure the vane is centred inside the tunnel and adjust if needed
- Position the sensor in the centre of the tunnel and line up the axis of the sensor perpendicular to the direction of airflow using the markings on the viewing window
- Power up sensor boards and wait 5 minutes to let the circuit and sensor stabilize
- Adjust the sensor base voltage (@ zero flow) to 3.0 V by turning the potentiometer (R2, Figure 6.2)
- Start recording vane anemometer velocity and hot-film sensor voltage
- Increase the blower voltage in increments of 5 V
  - Start at 7 V which is the air speed required to overcome the vane anemometer's static friction (~0.2 m/s)
- Apply a curve fitting method to match sensor voltage to air speed

One of the most popular curve fitting methods in thermal anemometry involves the use of King's Law to relate sensor output voltage to fluid velocity [103], [105]. This is also the method suggested by the film sensor manufacturer. King's Law is based on convective heat transfer over a cylindrical rod (i.e. wire) and is written as follows:

$$E^2 = A + BU^n \quad (6.1)$$

In this equation,  $E$  is the sensor output voltage,  $U$  is the fluid velocity in m/s, and  $A$ ,  $B$ , and  $n$  are constants. The empirical exponent  $n$  lies between 0.3 and 0.5 but is most often assumed to be 0.5. Both  $A$  and  $B$  are fluidic dependent constants which are determined from the calibration data. This dependency on fluid properties introduces errors, especially as fluid properties (temperature, pressure, humidity) vary from calibration conditions.

Another common method of calibration is to employ a polynomial fit. Ardekani and Farhani [109] and Manshadi and Esfeh [105] used a 5<sup>th</sup> order polynomial curve fit while George et al. insist that there is no need to exceed a 4<sup>th</sup> order polynomial [103]. Figure 6.4 shows the data from a typical sensor calibration run and compares 3 different polynomial curve fits. Sensor voltage is related to the mass flow rate rather than air velocity; convective heat transfer is affected by fluid density and is therefore fundamentally mass flow dependent. The corresponding air velocity scale is shown on the right hand side, and the calibration equation of the third order polynomial fit (mass flow rate) is displayed on the graph.

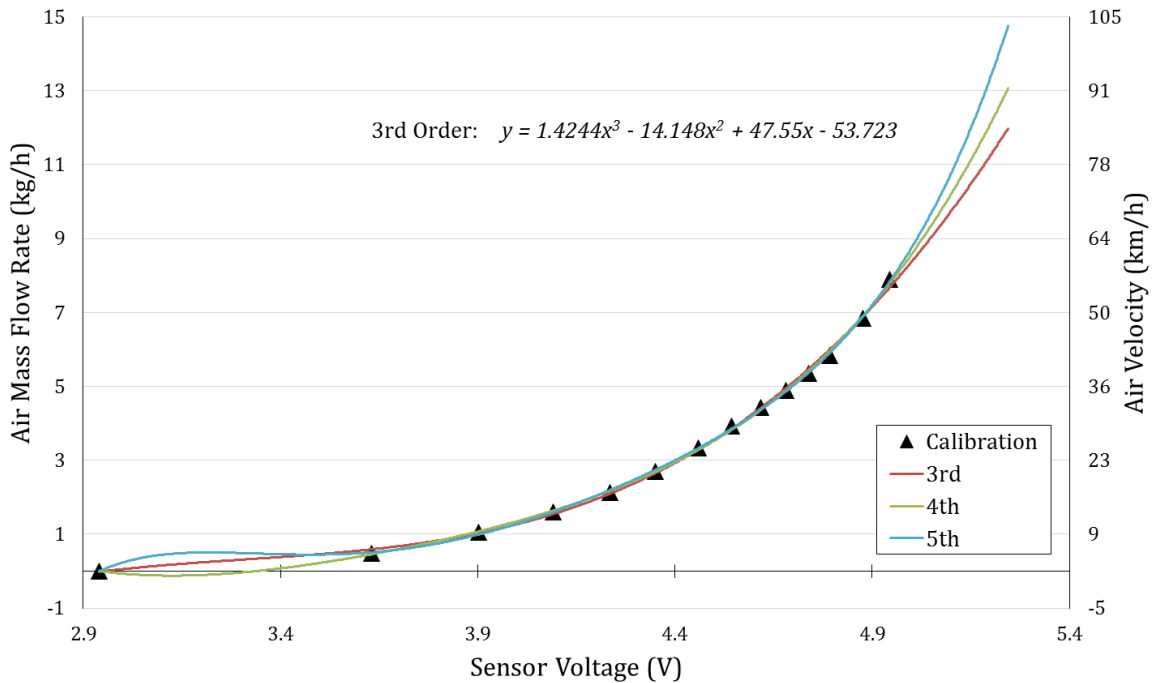


Figure 6.4 – Calibration data for hot-film sensor voltage to mass flow rate (kg/h) with 3<sup>rd</sup>, 4<sup>th</sup>, and 5<sup>th</sup> order polynomial curve fits

The mass flow based polynomial approximations compared are of 3<sup>rd</sup>, 4<sup>th</sup>, and 5<sup>th</sup> order. At speeds below 5 km/h, the higher order polynomials are inaccurate, with the 4<sup>th</sup> order even predicting a speed below zero. This issue is insignificant during driving but becomes important during low speed testing such as in a parking lot or in traffic where the only convection is due to the wind. For this reason, a 3<sup>rd</sup> order polynomial calibration curve is settled upon which eliminates the low speed uncertainty and conforms best to the calibration data.

Normal driving speeds in cities and rural areas can exceed 80 km/h and hence is a desirable target for the airflow sensor's operating range. Due to the speed limitations of the wind tunnel, the maximum calibration velocity was 57 km/h. Some extrapolation was required to extend the airflow sensor's range to correlate with air velocities around 80 km/h. Extrapolating higher order polynomials is risky since an inflection point might exist on the operative side of the curve beyond the extent of calibration data; whereas a 3<sup>rd</sup> order curve normally exhibits its only inflection point near the origin. The inflection point of the 3<sup>rd</sup> order curve occurs at 3.31 V, which is determined by finding the zero(s) of its second derivative as per the analysis below.

*Mass flow calibration equation:*

$$y(x) = 1.4244x^3 - 14.148x^2 + 47.55x - 53.723$$

*First derivative:*

$$y'(x) = 4.2732x^2 - 28.296x + 47.55$$

*Second derivative:*

$$y''(x) = 8.5464x - 28.296$$

@  $y''(x) = 0$ :

$$x = \frac{28.296}{8.5464} = 3.3109 \text{ V}$$

For the reasons provided, the third order polynomial fit was deemed adequate for relating mass flow rate of air {kg/h} to sensor voltage.

#### 6.2.4 Complications and limitations

##### *Directional Sensitivity*

The output of the FS5 sensor is sensitive to the direction of airflow due to its construction and its principle of operation. Figure 6.5 depicts air flowing over the hot-film sensor in two directions. On the left side, air flows parallel to the heating element, which is the orientation used in calibration ( $0^\circ$ ).

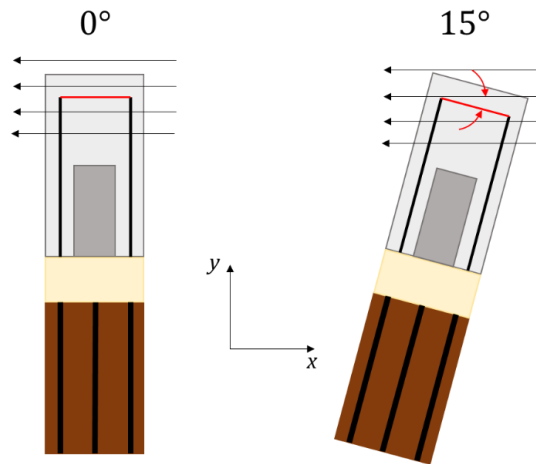


Figure 6.5 - Depiction of air flow over the hot-film sensor at yaw angles of  $0^\circ$  and  $15^\circ$

The right side of Figure 6.5 depicts the sensor at a yaw angle (about z axis) of  $15^\circ$ . It is evident that by varying the yaw angle of the sensor, the heat transfer conditions change accordingly. As the hot wire (coloured red) is oriented increasingly perpendicular to the flow (larger yaw angle), the efficiency at which heat is removed from the wire increases, thus augmenting the output signal. This phenomena is noticeable at angles greater than  $15^\circ$ , and the deviation increases with angle and air speed. Errors in air velocity of approximately 15% were recorded during preliminary tests at speeds of 30 km/h. These issues are normally solved by using a 3-dimensional hot-wire anemometer, but as discussed earlier, such sensors are not practical for the purposes of this work due to their delicate construction and high cost. The simple

solution was to house the film sensor inside of a small plastic tube in order to reduce the effects of varying angles. The tube also allows for mass flow rate of air to be calculated.

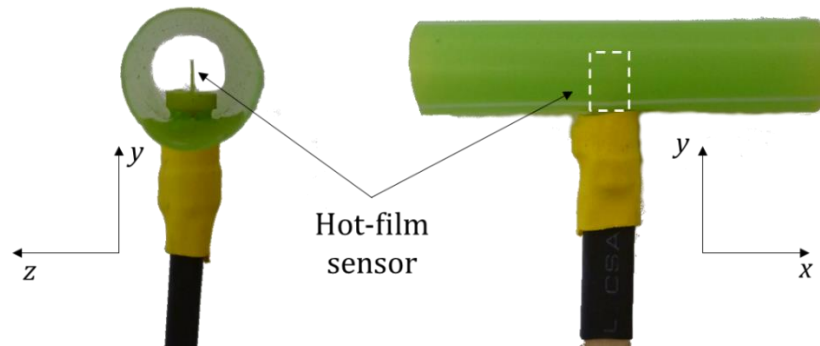


Figure 6.6 - Flow sensor placement inside of tube with corresponding directions

The sensor is inserted into the tube in the orientation shown in Figure 6.6, with the axis of the tube oriented parallel to the air flow direction ( $x$ ). The idea is that the air will flow in the desired direction over the sensor (parallel to the heater wire) because of the tube. Using this method, the velocity error at a  $30^\circ$  incidence angle of the tube to the flow stream was reduced to less than 1 km/h for a wind tunnel air speed of 30 km/h. As the vehicle travels forward, it is presumed that air will be flowing parallel to the direction of travel except in the event of heavy crosswinds. In any case, the tubular shroud greatly decreases sensitivity due to the angle of incidence. Rigidly fixing the sensor/tube assembly to the underbody of the vehicle and aligning the tube with the direction of travel was deemed to provide adequate longitudinal air speed measurements.

### ***Vane Anemometer Correction Factor Based on Wind Tunnel Cross-sectional Area***

The blockage effect of the handheld anemometer on the calibration wind tunnel was initially overlooked. This situation was discovered after analyzing air speed data taken during the road tests (Section 6.3). The air speeds registered by the hot-film anemometer were in excess of the vehicle's forward speed, which seemed unlikely. One possibility was that the sensor became contaminated by road dust, hence lost

calibration. A post road testing calibration confirmed that the sensor had not drifted out of calibration. The follow-up investigation suggested that the reference meter was incorrect. The error in the vane meter reading was attributed to a venturi effect caused by wind tunnel blockage due to the size of vane's housing; Figure 6.7 depicts the vane anemometer inside of the calibration tunnel. Subsequently, a correction factor was applied to the meter readings to obtain the air speed in the calibration tunnel ahead of the vane anemometer:

$$U_{tunnel} = U_{meter} * \frac{A_{tunnel} - A_{housing}}{A_{tunnel}} \quad (6.2)$$

$$U_{tunnel} = 0.8059 * U_{meter}$$

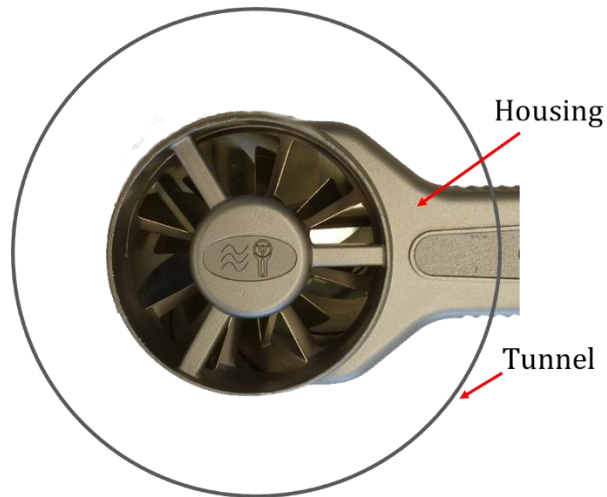


Figure 6.7 - Vane anemometer placement inside of calibration tunnel

The correction is based on the continuity condition ahead of, and through the vane. It is assumed that the vane itself blocks a negligible amount of air, and that only the ducted vane housing area contributes to the venturi effect. The correction shows that the air speed inside the unobstructed tunnel is approximately 20% lower than the reading on the vane anemometer, and applying this correction to the road test data yields more sensible results.

### ***Sensor Board Excitation Voltage***

The original airflow sensor calibration was carried out with the circuit board being powered at 14 V, in order to mimic the voltage output of a typical vehicle's 12 V power outlet. This is based on voltage readings taken in a conventional vehicle, where a 12 V battery is being charged by the alternator. The road tests showed that the voltage output of the test vehicle varied between 14 V and 12 V depending on the operating mode of the powertrain. Since the vehicle being studied is an EREV, when the vehicle enters charge-depleting mode, the output of the 12 V socket fluctuates to around 12.6 V (maintained by an inverter), but swings back to approximately 13.8 V when the engine is running and the vehicle is in charge-sustaining mode. Decreasing the circuit board voltage also decreases the heating power sent through the sensor, thus decreasing the circuit's output voltage. The 1.4 V difference between vehicle's output and the calibration voltage was too high to neglect, and recalibration needed to be performed again at the correct voltage. Most of the airflow measurements were taken while the vehicle was in charge-depleting mode, and thus a sensor board excitation voltage of 12.6 V was utilized for calibration.

### **6.3 ROAD TESTING**

As noted previously, a test vehicle was rented for a period of five days. The first day was spent picking up the vehicle, driving it back to the university, and setting up the instrumentation. Use of a rental vehicle limited the locations available for sensor placement. A five day booking realistically allowed for only three full days of testing. Nonetheless, as many different testing scenarios as possible were conducted over the three day period. Thermal measurements and vehicle data were recorded using a single laptop and combined to make up the full data set. This section describes the experimental setup and the road testing methods.

### 6.3.1 Instrumentation and Sensor Setup

All data was collected using a laptop which was powered through the vehicle's 12 V receptacle using a 120 V power inverter. Powertrain and battery pack data was recorded from the vehicle's CAN bus via two OBD-II ports located under the dash. A neoVI FIRE diagnostic scan tool was used to relay the CAN messages to the laptop, which were decoded using Vehicle Spy software at a rate of 10 Hz. The following data signals were among those recorded through this interface: vehicle speed, battery SOC, battery voltage, battery current, coolant temperatures, motor speeds, engine speed, battery temperatures and more. Since two separate OBD-II ports are required to obtain both battery system and general vehicle information, a custom cable capable of reading two ports simultaneously was created. Two OBD-II extension cables were modified into a Y-cable with the single end connected to the scan tool, and the double end connected to each OBD-II port. The pins on the double end were carefully mapped to separate input channels on the scan tool interface, which allowed for simultaneous monitoring of both ports.

Thermal measurements were gathered using IPEtroniks thermocouple and voltage modules, which were recorded by the laptop running the IPEmotion software. The 12 V power cable designed to power the airflow sensor circuit boards was also used to power the IPEtroniks sensing modules. K-type thermocouples were used for temperature measurement, HFS-4 sensors for heat flux measurement and the FS5 hot-film anemometer was used to measure local air speed.

One of the few accessible areas for sensor placement was the bottom of the baseplate. Heat flux was measured on the baseplate since it was the only practical surface on which to attach a delicate sensor. A series of thermocouples were mounted to several different points on the bottom surface of the baseplate, and two heat flux sensors were pasted to the centre of the baseplate. The heat flux sensor and thermocouple placements are shown in Figure 6.8. These sensors were attached in the same manner as in the lab tests (Section 4.2.1) to help ensure consistency in the measurements.



Figure 6.8 - Underside of baseplate with thermocouples and heat flux sensors attached

The fibre-reinforced plastic debris shield was reinstalled onto the baseplate which helped protect the sensors from any dangers on the road. In retrospect, it would have been beneficial to have had temperature measurements on the surface of the shield to help broaden the data set.

One of the objectives in performing road tests was to capture the actual ambient source temperatures to be used as inputs to the thermal model. The underbody air temperature was measured by two hanging thermocouples, the vehicle's chassis temperature above the battery pack cover was recorded, and the bulkhead ambient source was determined by placing a thermocouple between the bulkhead and the engine. Road surface temperature could not be measured during driving but was determined in a separate test where the vehicle was parked. These measurements are expanded upon in Section 6.4. Though it was planned to record airflow at additional locations, the logistics and timeline did not permit the installation of these sensors.

### **6.3.2 Road Testing Overview**

The road tests were designed mainly to analyze and better understand the operation of the vehicle's systems. This information was extracted from the CAN bus data and

used to refine the custom powertrain model in Autonomie for a different all-encompassing thesis project. Thermal measurements were taken during these tests in attempt to map out the external influences on the battery pack in day-to-day driving. Before renting the vehicle, goals were set which were then used to form ideas for different types of testing. A log book was kept for several purposes. Each log entry contained the time and a comment, which was generally a location used for mapping purposes. Additionally, notes were taken based on any events taking place such as the cooling system turning on or the vehicle switching power modes. Most of this information was not utilized for this work but was rather useful for the other project. The following general procedure was employed to carry out every test:

- Map out a route that would allow a specific test goal/target to be reached
- Visually inspect the sensors and measurement systems
- Start the vehicle and ensure all DAQ signals are functioning correctly
- Start logging data on Vehicle Spy and IPEmotion simultaneously
- Co-pilot starts manual time log
- Proceed by driving the test route, then return to campus

The following list describes all of the road tests that were conducted:

### ***Run #1: Rush hour city driving***

This test run consists of approximately three hours of stop-and-go driving during peak traffic hours. The vehicle was in charge-sustaining mode which allowed for the engine's effects on the battery pack to be noticed when stopped in traffic.

### ***Run #2: Rural commute***

This test run simulates an average rural-type commute of approximately 30 minutes in a single direction. This is a combination of urban driving in traffic and highway driving at speeds of around 80 km/h. The vehicle was in charge depleting mode.

### ***Run #3: Parking lot heat soak***

This test was conducted immediately after completing Run #2. The main objective was to capture the effects of the sun on the battery and vehicle interior. The run lasted approximately three hours when the sun was at its peak (around noon). An additional thermocouple was added to measure the temperature of the pavement under the vehicle.

#### ***Run #4: Airflow sensor test***

This was the first run with the hot-film anemometer attached under the vehicle. This was a short run with the sole purpose of ensuring that the airflow sensor remained secure and was operating correctly (it was not). Final adjustments were made before the next test run.

#### ***Run #5: Highway driving***

This test run consists of driving at high speeds on a large highway for approximately 100 km, which is the type of commute that many people in the Greater Toronto Area experience every day. The airflow sensor was attached and recording for the majority of the test. The vehicle was also operating in charge-sustaining mode.

#### ***Run #6: Urban driving***

Everyday urban driving is simulated in this run with the vehicle in charge depleting mode. The route and driving style are typical of a few hours of running errands during the day. The airflow sensor was not installed on this day because of rain.

#### ***Run #7: Hill climbing***

A series of hill runs were conducted in different selected driving modes such as “mountain” or “sport”. The vehicle was still in charge depleting mode since the previous run did not fully drain the battery.

#### ***Run #8: Country road driving***

In this run, a series of different country roads were travelled at varying speeds. These roads also had many hills with different gradients.

#### ***Run #9: Rush hour city driving in sport mode***

As in Run #1, this test was conducted during rush hour following a similar type of route in charge-sustaining mode. The vehicle was put into “sport mode” and driven more aggressively than in Run #1.

#### ***Run #10: Returning the vehicle***

The drive to return the vehicle was recorded. This was a high-speed highway run in charge-depleting mode. All of the thermal sensors were removed prior to the test run since the vehicle was being returned, so only the CAN based data was recorded.

## **6.4 ENVIRONMENTAL SOURCE ADAPTATIONS**

The single environmental source  $T_{amb}$  used in the lab based calibrations needs to be replaced by four separate sources representing the road, underbody air, vehicle chassis, and engine compartment. The modelling of each source’s respective resistor is also presented. The objective is to mimic the environment that the battery pack is exposed to when installed on the vehicle.

### **6.4.1 Front Bulkhead**

The front section of the vehicle’s underbody is show in Figure 6.9. Some main components such as the engine, transmission and steering rack are labelled to provide a frame of reference.

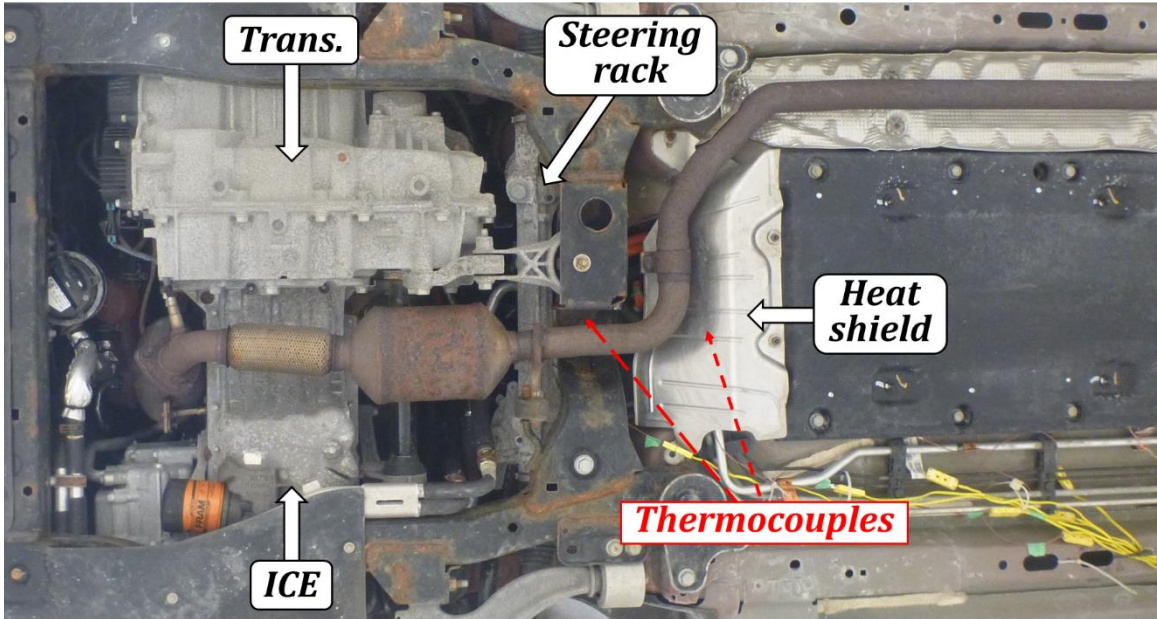


Figure 6.9 - View of vehicle underbody depicting major components and general thermocouple locations

The front bulkhead is where the plumbing from the battery cooling system connects to the pack, and is situated behind the internal combustion engine. There is a heat shield installed between the exhaust pipe and the bulkhead in an attempt to reduce heat transfer into the fluid pipes. These complex installation conditions require the outer bulkhead resistance,  $R_{obh}$ , to reflect such changes. A new temperature source  $T_{eng}$  is defined to represent local air temperature in the engine compartment ahead of the bulkhead. Figure 6.10 depicts the new bulkhead heat path which includes the new temperature source  $T_{eng}$ .

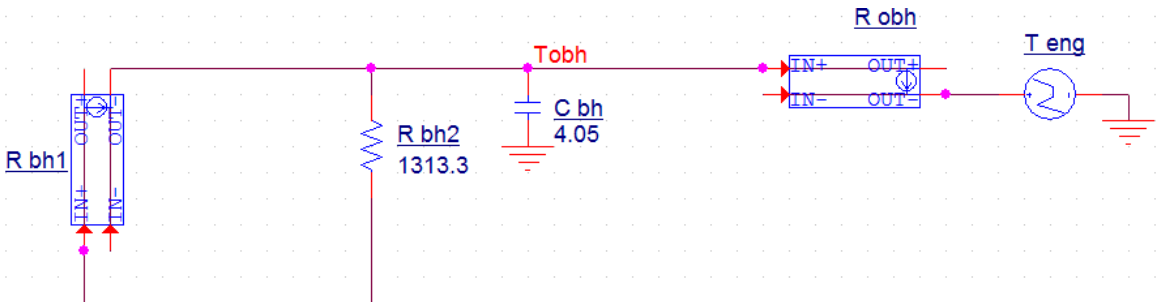


Figure 6.10 - Bulkhead heat flow path schematic modified to represent the vehicle's environment

Since the battery pack's front bulkhead was essentially inaccessible without the removal of several components, the best attempt to capture the bulkhead's environmental conditions was made by installing two thermocouples in its vicinity. The general transverse locations of these thermocouples are outlined in Figure 6.9. The rearmost thermocouple measures the air temperature between the bulkhead and the heat shield (picture unavailable). The frontmost sensor measures the air temperature between the engine and the firewall as shown in Figure 6.11. It was difficult to photograph these sensors clearly due to obstructions such as the steering rack and sub-frame crossmember. Both thermocouples were positioned at approximately the same vertical height along the vehicle's centreline.

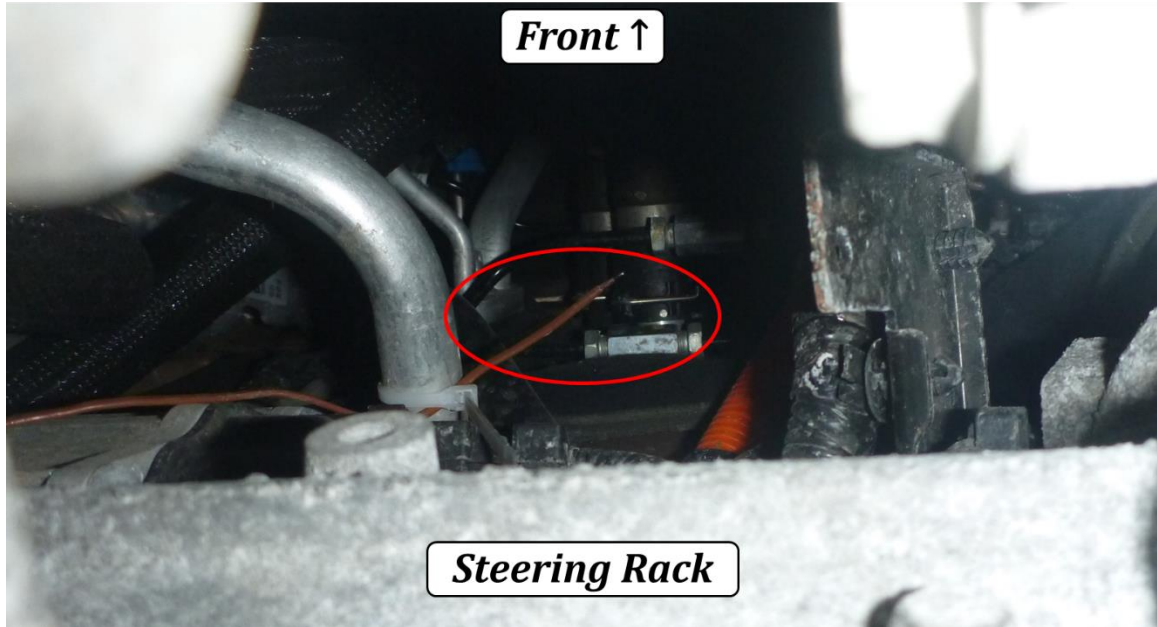


Figure 6.11 - Exact location of the front thermocouple between the engine and firewall

The bulkhead, firewall, and underbody air temperatures during Run 9 (sport mode city driving, charge-sustaining) are displayed in Figure 6.12. Figure 6.13 compares the engine power (in kW) and vehicle speed for the same test run. The heating effects from the engine ought to be noticeable since the powertrain was operating in charge-sustaining mode. Additionally, the stop-and-go driving in this test run were useful in indirectly observing the effects of convection on the bulkhead by analyzing the

thermocouple readings. The bulkhead air temperature was measured behind the heat shield.

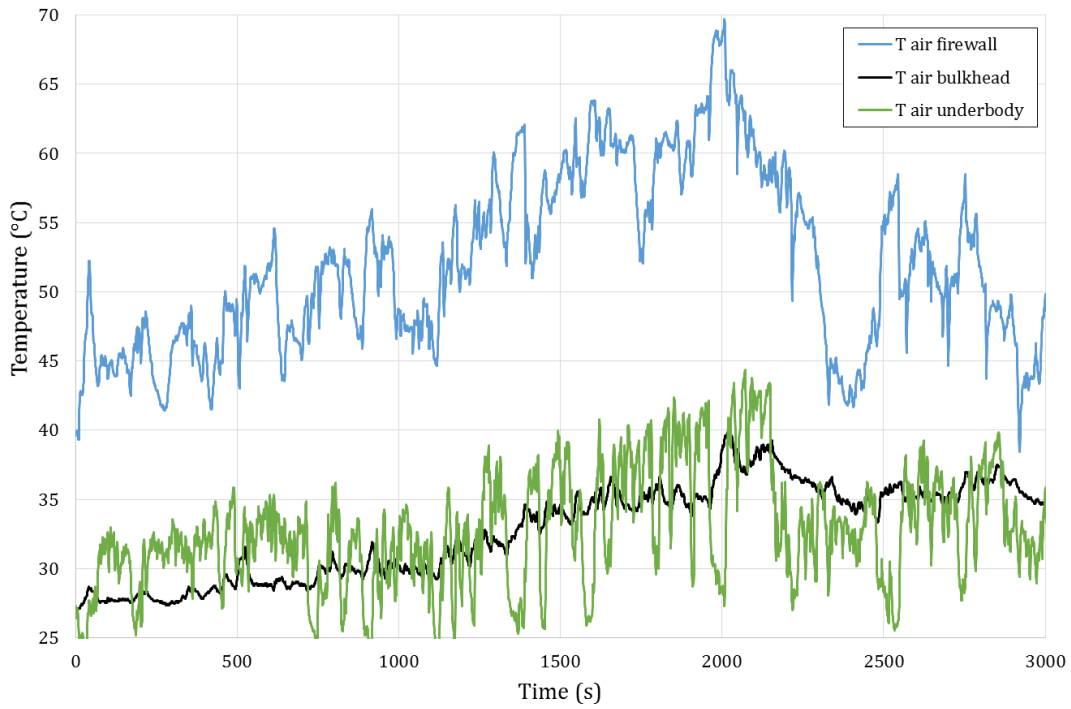


Figure 6.12 - Comparison of firewall, bulkhead, and underbody air temperatures during test run #9

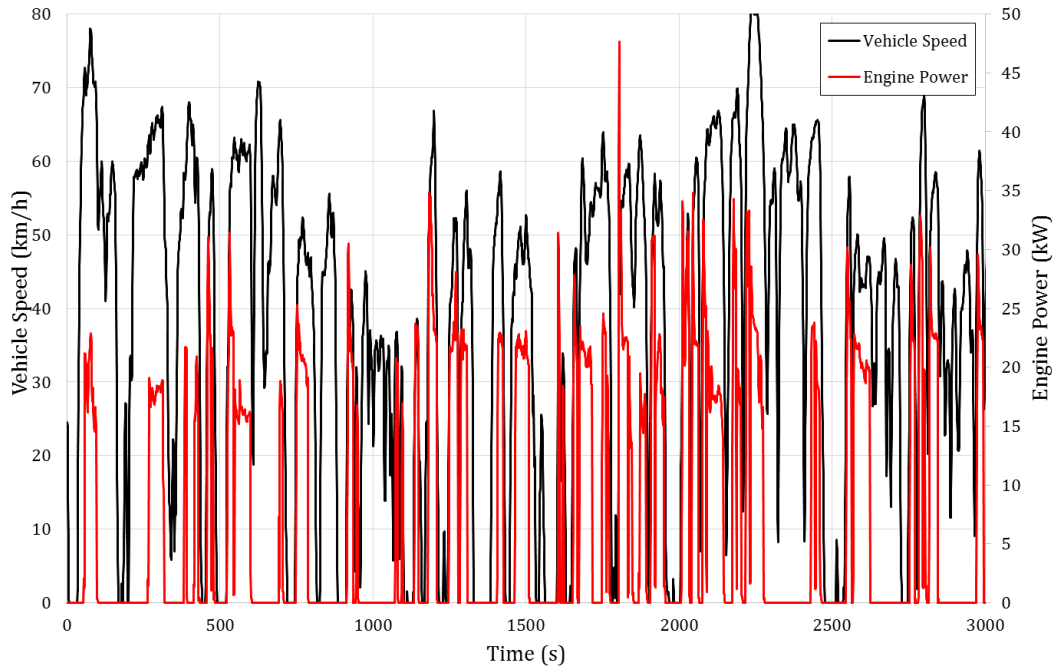


Figure 6.13 - Vehicle speed (km/h) and engine power (kW) profiles for road test #9

From Figure 6.12, it can be deduced that temperature variations behind the heatshield (i.e. bulkhead temperature) are very slight when compared to the other two thermocouple readings. This indicates that the level of convection in front of the bulkhead is minimal. The short term fluctuations in the bulkhead sensor lie within the resolution of the measurement system (less than  $\pm 0.1\text{ }^{\circ}\text{C}$ ) which are similar to the air temperature fluctuations as measured in the lab. The other two sensors on the other hand, fluctuate at levels around  $0.4\text{ }^{\circ}\text{C}$  between readings recorded at 1 Hz, indicating turbulence.

Another indication of low convection levels in front of the battery pack bulkhead is the correlation between vehicle speed and local temperature variations. Figure 6.14 shows the correlation between the air temperatures and vehicle speed during a stop-and-go portion of the same road test in order to more closely examine the effects of engine heat on the surrounding air.

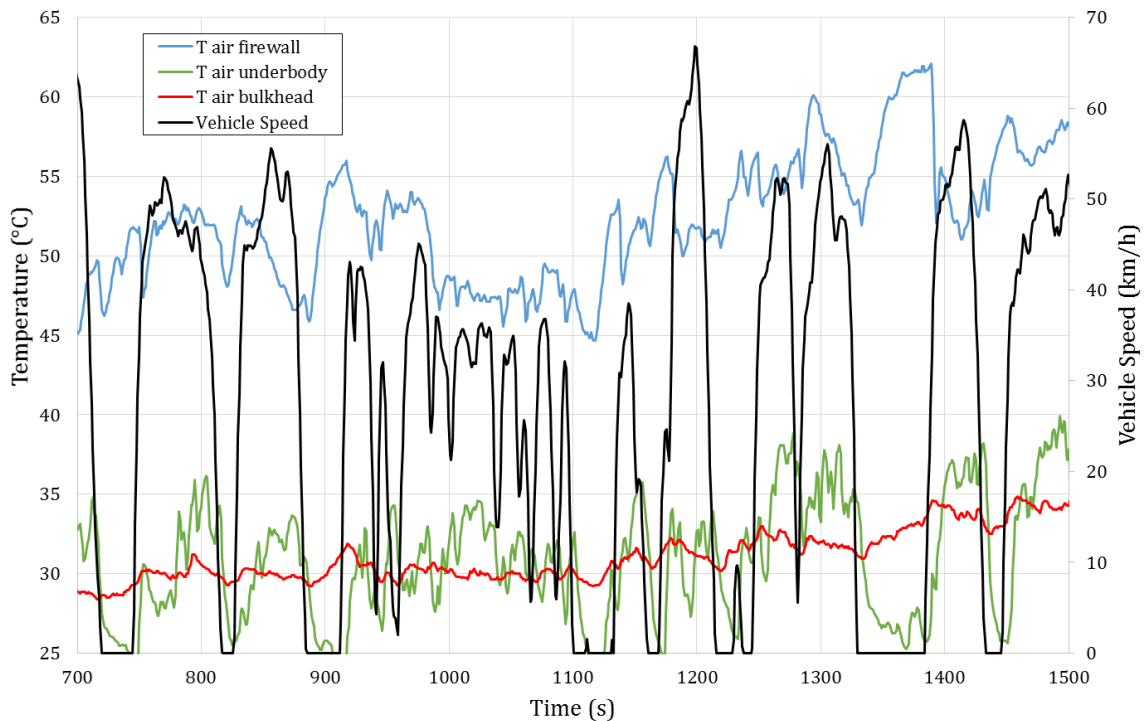


Figure 6.14 - Air temperatures and vehicle speed during road test #9

As the vehicle comes to a stop, the engine warms the air inside its compartment, causing a noteworthy increase in firewall air temperature; this effect is noticeable at

900 s for example. The underbody temperature experiences the opposite trend since the warm air remains relatively stagnant at the front of the vehicle. As the vehicle moves forward, the engine bay experiences ventilation and the firewall temperature lowers as a result. Conversely, the heat from the engine now travels rearward, causing a rise in underbody air temperature.

While the effect of vehicle motion on the underbody and firewall air temperatures is evident, the bulkhead air measurements remain relatively stable. From such observations, it is reasonable to assume that airflow is minimal in front of the bulkhead due to the heatshield and surrounding structures. This assumption suggests that the bulkhead's environmental conditions are similar to what is seen in the laboratory setting. Additionally, the temperature difference seen between the bulkhead itself and the surrounding air is similar to lab conditions (less than 10 °C). Therefore, based on these observations, the laboratory-based values for  $R_{obh}$  are deemed suitable for use in the vehicle battery pack thermal model.

#### 6.4.2 Cover

As described earlier, the battery pack fits into a recessed tunnel on underside of the vehicle chassis. Inside this tunnel, there is an airgap that separates the cover from the chassis. The thermal resistance of this air will replace  $R_{oc}$  from the lab battery pack model. The temperature of the chassis,  $T_{chassis}$ , is the environmental source that connects to the cover as shown in Figure 6.15.

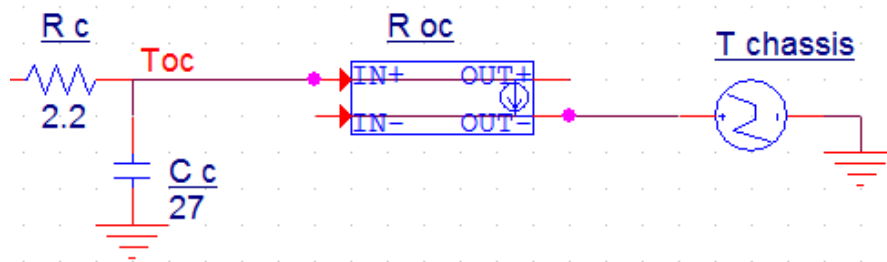


Figure 6.15 - Thermal network schematic of the cover path as modelled for the vehicle

During the road tests, the chassis temperature was measured in three different locations. One surface measurement was taken on each side of the vehicle in the manner depicted in Figure 6.16, and another thermocouple was inserted into the middle of the central cavity but not taped due to the small size of the gap. Because of this, the exact location of the middle sensor is unknown but is assumed to lie inside the gap near the centre of the vehicle as illustrated in Figure 6.17.

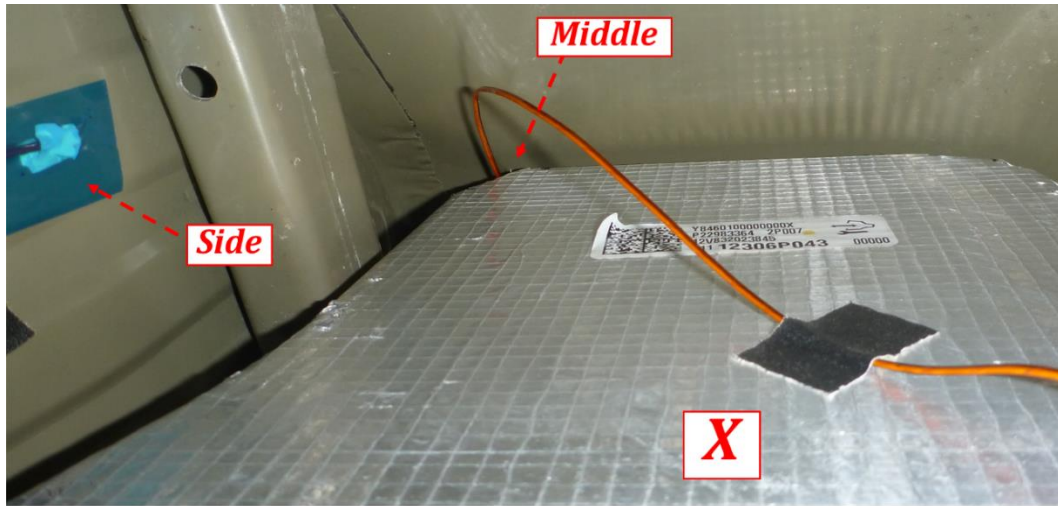


Figure 6.16 - View from the rear driver side of two chassis temperature thermocouples

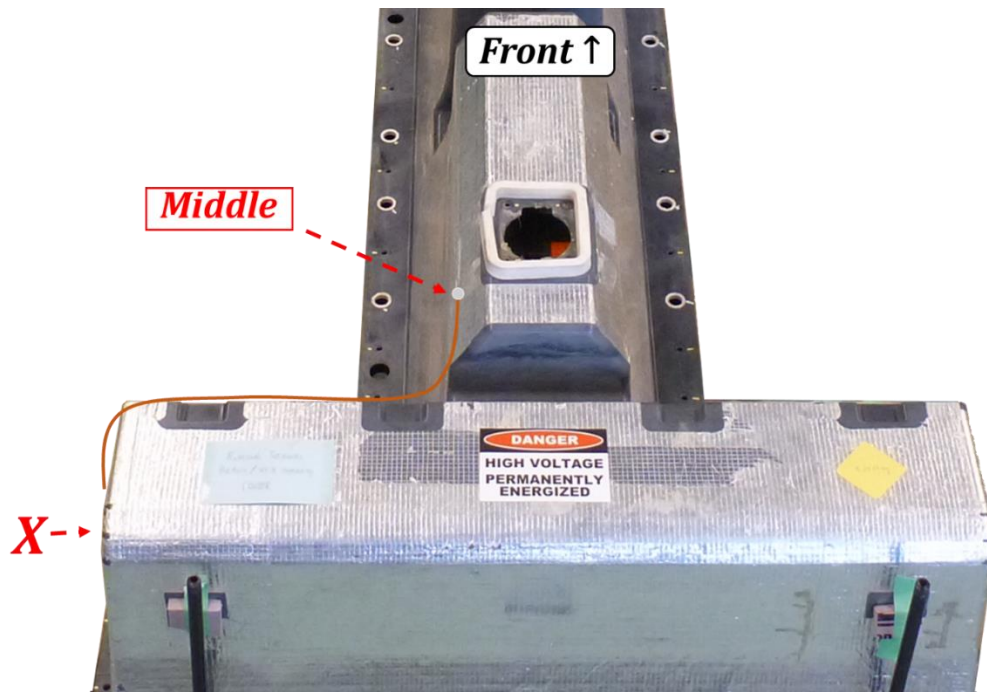


Figure 6.17 - Top view of the pack rear showing the approximate location for the middle sensor

The cover face labelled as “X” is shown in both figures in order to better visualize the pack orientation and sensor locations. The environment of the middle sensor should be more representative of the majority of the cover since the side sensors are located above the openings nearer to the rear wheels.

Other than these exposed rear portions of the battery pack, it is assumed that there is minimal air convection inside the gap between the chassis and the cover. Inside the tunnel, there is a crossmember that divides the battery pack lengthwise almost in half. This would additionally restrict the air from circulating to the rear of the pack through the gap. The outer cover resistance,  $R_{oc}$ , can therefore be approximated by a combined radiative and conductive resistance between the cover and the chassis.

The radiation heat transfer is modelled as two parallel plates of equal size and the heat flow from the battery pack cover to the vehicle’s chassis is expressed by Equation (6.3) [52]:

$$\dot{Q}_{rad} = \frac{A_1 \sigma (T_1^4 - T_2^4)}{\frac{1}{\epsilon_1} + \left(\frac{A_1}{A_2}\right) \left(\frac{1}{\epsilon_2} - 1\right)} \quad (6.3)$$

Where subscript 1 represents the cover, subscript 2 is the chassis, and  $\sigma$  is the Stefan-Boltzmann constant. The heat transfer coefficient  $h_{rad}$  can be re-written as:

$$h_{rad} = \frac{\sigma (T_1^2 + T_2^2) (T_1 + T_2)}{\frac{1}{\epsilon_1} + \left(\frac{A_1}{A_2}\right) \left(\frac{1}{\epsilon_2} - 1\right)} \quad (6.4)$$

The heat transfer coefficient for conduction through the small airgap ( $l_{gap}$ ) is:

$$h_{cond} = \frac{k_{air}}{l_{gap}} \quad (6.5)$$

The equivalent thermal resistance is thus:

$$R_{oc} = R_{gap} = \frac{1}{h_{tot} A_1} = \frac{1}{A_1 (h_{rad} + h_{cond})} \quad (6.6)$$

The resistance lookup table values for  $R_{oc}$  are numerically estimated by evaluating Equation (6.6) at different temperatures. The average gap length is estimated to be 20 mm and the emissivity of the chassis and cover are estimated to be 0.9 and 0.3, respectively. The conductivity of air is also evaluated at the mean temperature. From the road tests, the temperature difference between the cover and chassis at the exposed end sections rarely exceeds 3 °C. Since the end pieces are extreme cases due to convection, the temperature differential across the airgap will be much smaller than what is experienced at the ends. The resistance is evaluated for a range of cover temperatures from 10 to 40 °C, using a temperature difference of 3 °C. The average resistance at each cover temperature is presented in Table 6.1. For the approximate temperature range experienced during the road tests (20 – 40 °C), there is a change in radiative resistance of approximately 15% which suggests that a variable resistor is required.

Table 6.1 – Outer cover resistance  $R_{oc}$  evaluated at different outer cover temperatures  $T_{oc}$

$T_{oc}$ (°C)	10	15	20	25	30	35	40	45	50
$R_{oc}$ (°C/W)	68.0	65.6	63.4	61.8	59.1	57.1	55.2	53.4	51.6

Since the radiative resistance value remains relatively constant with respect to the temperature difference between the cover and chassis over the temperature range seen, the variable resistor’s behaviour is modified to respond to changes in absolute cover temperature rather than the difference between the cover and the chassis. This is achieved by changing the negative reference voltage of the voltage-controlled current-source (that mimics a variable resistor) to 0 V, rather than  $T_{chassis}$ . The values from Table 6.1 are then used directly to govern the variable resistance behaviour.

### 6.4.3 Underbody Convection and Road Effects

The baseplate is the final path to be adapted, but is arguably the most important and complex path. In the laboratory, the battery pack remains static on top of a wooden pallet, leaving natural convection and radiation to be the key modes of heat transfer out of the baseplate. On the vehicle, the baseplate is in contact with the underbody air

and is highly exposed to the elements. This requires adapting its external conditions to consider radiation heat transfer from the pavement, as well as external convection from the underbody air currents. An extra resistor is also added after the baseplate resistance which represents the underbody debris shield installed on the vehicle. These new components are successfully validated using real-life road tests.

#### ***6.4.3.1 Addition of Plastic Baseplate Shield***

The fibre reinforced plastic shield shown in Figure 6.18 is attached to the bottom of the baseplate to reduce drag, add isolation and physical protection [20]. During the majority of the lab testing, this shield was removed in order to facilitate the placement of sensors on the baseplate. As a result, the lab model does not include the effects the shield has on the pack's heat transfer.

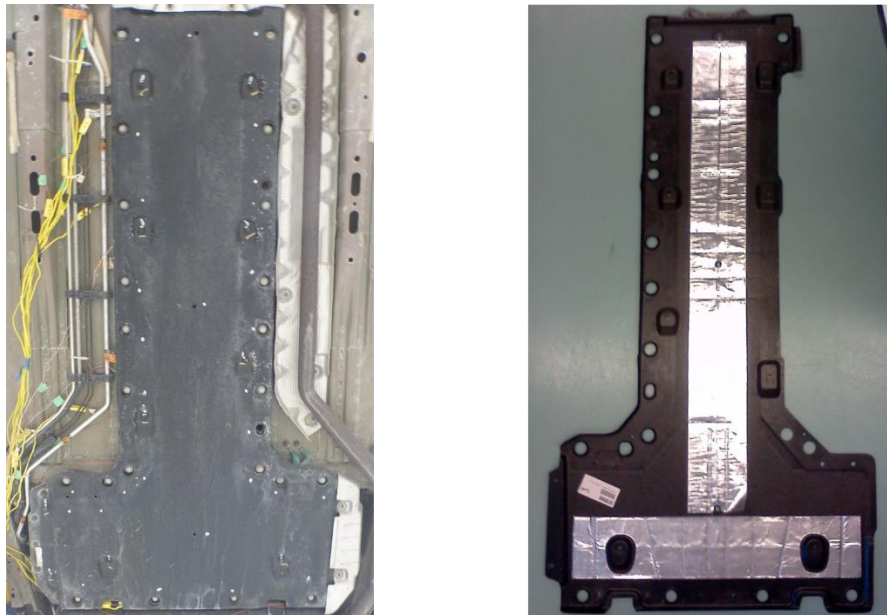


Figure 6.18 – Underbody shield: on the vehicle (left) and removed showing the interior face (right)

Figure 6.18 depicts the placement of the shield on (left), and off (right) the vehicle. To model this shield, a resistor and capacitor must be added in line with the baseplate resistor. The following sections describe the modelling process and the changes to the model.

## Modelling

Examining the baseplate/shield assembly, the two modes of heat transfer are radiation, and conduction through the airgap between them. Convection is assumed to be negligible since the shield curls around the edges of the baseplate, leaving little to no opening for air to enter and circulate inside the small gap. The airgap thus provides an extra layer of insulation between the baseplate and the environment. Equations (6.4) - (6.6) are utilized to calculate the combined radiative and conductive resistance between the baseplate and shield denoted as  $R_{sh}$ .

The following assumptions are made in the modelling of this resistor:

- The baseplate and shield have the same surface area
- The temperature difference does not vary enough during operating conditions to have a significant effect on the heat transfer coefficient, and thus resistance
- Thermal conductivity of air is constant
- Surface temperatures and airgap thickness are uniform
- The emissivity of the interior face of the shield is uniform and is the averaged value between the reflective foil and plastic

Figure 6.19 (left) schematically demonstrates how the shield resistance chain is constructed. The thermal resistance from the thickness of the shield  $R_t$  is added in series with that across the airgap ( $R_{gap}$ ) to form the total shield resistance  $R_{sh}$ .

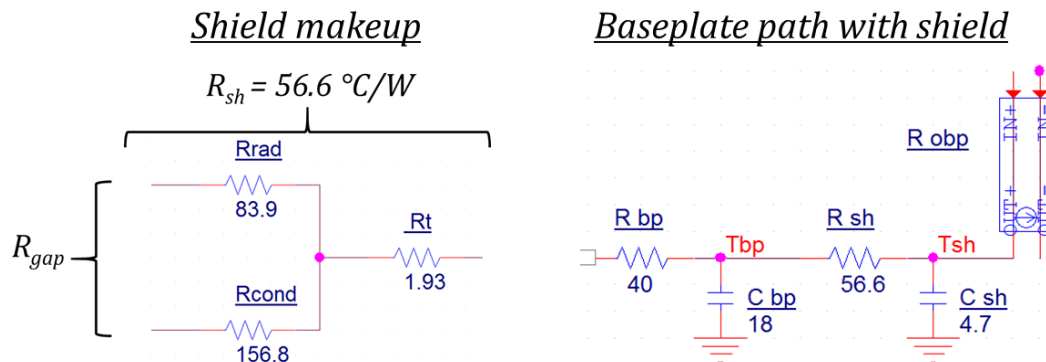


Figure 6.19 – Shield resistor broken up into its constituents (left) and combined baseplate/shield thermal network (right)

In the full thermal network, the total shield resistor and its capacitor,  $C_{sh}$ , are added between the baseplate and its respective ambient resistor as shown on the right side of Figure 6.19. The thermal capacitance of the shield was determined using the weighing method as described previously. The resultant resistance and capacitance are  $R_{sh} = 56.6 \text{ }^\circ\text{C}/\text{W}$  and  $C_{sh} = 4.7 \text{ J}/^\circ\text{C}$ .

### Validation

The shield resistor and capacitor values are validated by comparing the baseplate temperature response in a standard lab test, to a run with the shield installed (shown in Figure 6.20). An experimental test run at comparable ambient conditions without the shield is included for comparative purposes. The baseplate temperature without the shield reaches a steady-state value approximately  $2 \text{ }^\circ\text{C}$  lower than when the shield is installed, which indicates that the shield component is required for accurate baseplate path modelling.

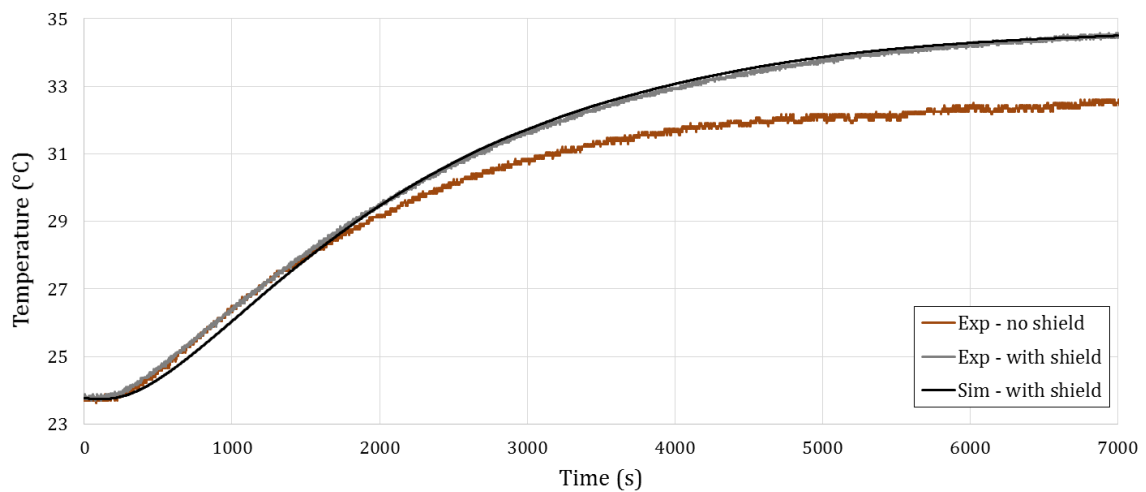


Figure 6.20 - Baseplate temperature with shield attached: experimental vs. simulation

The error in baseplate temperature recorded when the shield is added, both physically and in modelling, is comparable to when no shield is present such as in the other lab tests; the maximum error is  $0.46 \text{ }^\circ\text{C}$  with an RMS error of  $0.16 \text{ }^\circ\text{C}$ . The agreement between measurement and simulation indicates that the theoretical resistor and capacitor developed for the model with the shield are valid.

### **6.4.3.2 Road Radiation**

The radiation path represents the heat transfer between the baseplate shield and the road. This is considered separate from convection due to the effect the sun has on the temperature of the road. On a sunny day, the road temperature is much warmer than the ambient temperature, increasing its radiant heat output. As a result, the road temperature is added as a voltage source in the network.

The radiation heat transfer between the road and the shield was modelled as two parallel plates of equal size. This assumption is made in order to simplify the calculations involved in determining the radiation shape factor of the system. The distance between the two surfaces is relatively short, being only the ground clearance to the shield. The surrounding area of pavement would affect radiation heat transfer, with the majority of the heat coming from the area directly below the baseplate shield. As a result, Equation (6.3) is used to model the heat flow between the baseplate shield and the road, due to radiation. It is assumed that the shade provided by the vehicle itself is negligible when the vehicle is moving, or stationary for a short period, due to the large thermal mass of the heated road surface.

The equation governing radiation heat transfer is dependent on the temperature of both the baseplate shield and the road; since both terms appear in the equation to the fourth power. This suggests that a fixed resistor is not the most suitable component to represent such phenomena. A much better fit is a variable resistor modelled by a voltage-controlled current source, similar to what is utilized for the cover.

The GVALUE component (voltage-controlled current source) in this case is implemented differently. Rather than using a lookup table for resistances and temperatures, the radiation heat flow as described by Equation (6.3) is employed for the direct current output of the component. This equation is programmed into the GVALUE component's properties ( $R_{rad}$ ), which is dependent on both the baseplate shield and road temperatures. In essence, the theoretical heat flow out of the baseplate (current output) is calculated based on the instantaneous baseplate and

road temperatures. Figure 6.21 illustrates how Equation (6.3) is programmed into the output properties of  $R_{rad}$  in PSpice.

$$\dot{Q}_{rad} = \frac{A_{bp}\sigma}{\frac{1}{\epsilon_{sh}} + \left(\frac{1}{\epsilon_{road}} - 1\right)} \underbrace{T_{sh}^4}_{\text{}} \underbrace{T_{road}^4}_{\text{}} \underbrace{\# \text{ of cells}}_{\text{}} / 288$$

$$\dot{Q}_{rad} = (0.00000003952 * (\text{PWR}((273+V(\%IN+,0)),4) - \text{PWR}((273+V(\%IN-,0)),4))) / 288$$

Figure 6.21 –Current output expression for  $R_{rad}$  PSpice component with corresponding equation terms

Variables denoted by the subscript *sh* represents a property of the shield. The output of this expression represents the per cell heat flow from the baseplate to the road in mW. If the temperature of the road is greater than that of the shield, the current output would be negative, meaning that heat is entering the baseplate. The new configuration of the entire baseplate path is shown later in Figure 6.24 on page 134.

### 6.4.3.3 Convection

The level of convection over the baseplate was relatively unknown but remained a key piece of information required for the modelling of the baseplate path. The hot-film CTD anemometer discussed earlier was mounted to the underbody and positioned approximately 2 cm below the centre of the baseplate shield. This configuration was maintained for road tests #4 and #5. Figure 6.22 compares the anemometer reading to the vehicle forward speed in {km/h} for test run #4. For the most part, the air velocity is comparable to the vehicle’s forward speed. The larger differences in the last 200 s of the run could be caused by wind gusts and oncoming traffic. Similar conclusions can also be made by examining the test run at highway speeds shown in Figure 6.23. The higher anemometer readings during the first half of this test run, and the convergence during the second half can be attributed to a reversal of direction, indicating that the wind direction has a slight effect on underbody airspeed.

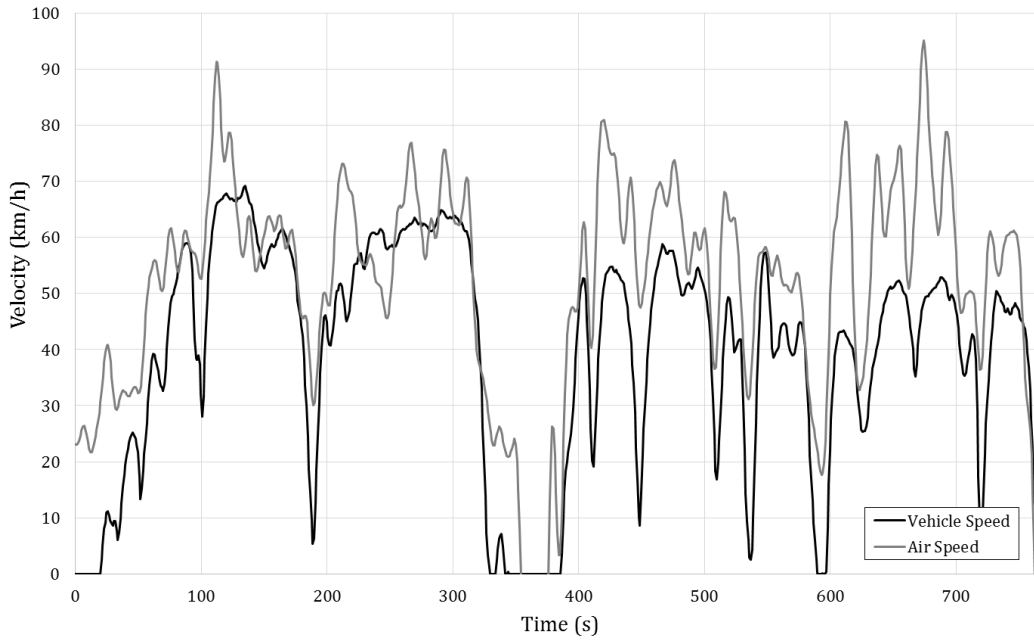


Figure 6.22 - Underbody air velocity and vehicle speed (km/h) for road test run #4

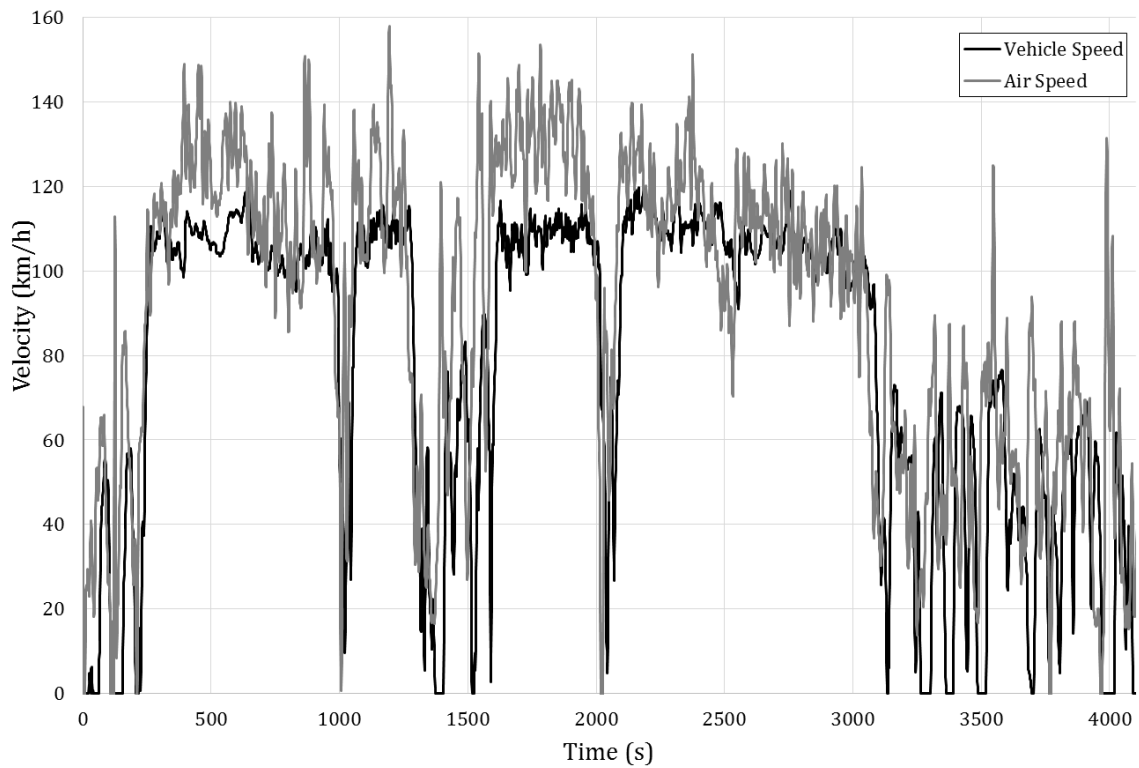


Figure 6.23 - Underbody air velocity and vehicle speed (km/h) for highway speed road test run #5

Based on these observations, a logical conclusion would be to presume that the local airspeed under the baseplate can be estimated by the vehicle forward speed, and

wind effects may be added if they are known. This assumption is dependent on the aerodynamics of the vehicle being modelled. The airflow sensors in this case merely suggest that on the Volt, the air speed under the exposed baseplate is comparable to the vehicle forward speed, indicating that there are no perceivable “ground effects” during the test runs presented. This assumption was used in the modelling of the convective resistor  $R_{conv}$  which can also be applied to other road tests. The original intent of the CTD anemometers was to map out the convective circulation occurring in tight locations such as behind heat shields and various body cavities surrounding the pack, but due to vehicle access restrictions, measurements were limited to under the baseplate.

The heat flow from the baseplate shield to the air, due to forced convection, is modelled using the following relation [49]:

$$\dot{Q}_{conv} = \frac{k_{air} A_s Nu (T_{sh} - T_{air})}{L} \quad (6.7)$$

Where  $L$  is the length of the baseplate shield. Due to its length (1.62 m), the laminar airflow region is too long to be neglected, and the following relations are used to determine the Nusselt number [49]:

$$Nu = (0.037 Re_L^{0.8} - 0.871) Pr^{1/3} \quad (6.8)$$

$$0.6 \leq Pr \leq 60, \text{ and } 5 \times 10^5 \leq Re_L \leq 10^7$$

$$Nu = 0.664 Re_L^{0.5} * Pr^{1/3} \quad (6.9)$$

$$Re_L < 5 \times 10^5$$

Equation (6.8) applies to higher speed force-convection, and accounts for a laminar flow region that cannot be ignored and may be applied to any fluid. Equation (6.9) is used for low speed cases. The Prandtl number ( $Pr$ ) and thermal conductivity ( $k_{air}$ ) are assumed to be relatively constant throughout the thermal operating range of the road tests. The kinematic viscosity ( $\nu$ ) of air is approximated using a linear relationship

based on the film temperature of the fluid, and the Reynolds number ( $Re$ ) is determined using Equation (6.10), where  $V$  is the velocity of the air in m/s.

$$Re = \frac{VL}{\nu} \quad (6.10)$$

Equations (6.7)-(6.10) demonstrate that convective heat transfer is less than proportional (to the power of 0.5-0.8) to the air speed, which reduces the overall impact of errors present in the air speed approximation. The more sensitive parameter is the temperature differential (directly proportional), which has been adequately measured during the road tests.

Similar to the radiation path, the heat flow equation (6.7) is programmed into the voltage-controlled current source  $R_{conv}$ . The temperature of the environment is defined by the voltage source  $T_{air}$ , which is the underbody air temperature. In addition, the air speed is defined as a separate voltage source  $V_{air}$  which is used as an input to  $R_{conv}$ . As a result,  $R_{conv}$  dynamically calculates and outputs the theoretical heat flow based on baseplate temperature, air temperature, and air velocity. An *if* statement is programmed to apply the correct  $Nu$  relation based on  $Re$  (i.e. air speed). As in the case of the radiation resistor, the output of  $R_{conv}$  is in {mW/cell} and a positive value represents heat flowing out of the baseplate.

Figure 6.24 depicts the baseplate path configuration for the full vehicle model along with the air speed as a separate voltage source input. It is important to note that the air velocity sub-circuit is completely separate from the thermal network, and only serves as an input to the  $R_{conv}$  component.

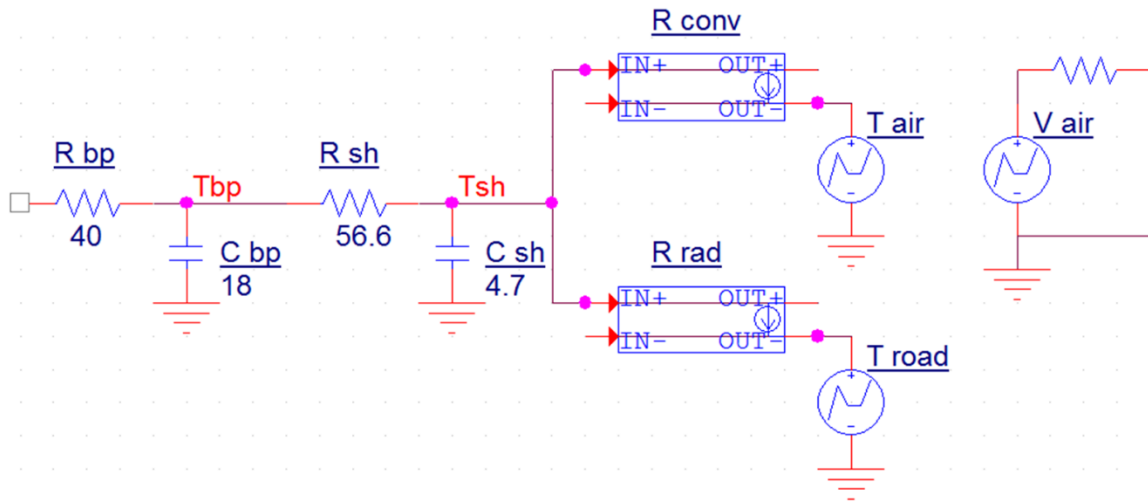


Figure 6.24 – Full baseplate path including shield, convection, and radiation sources

#### 6.4.3.4 Validation

The validation for the convection and radiation components in the baseplate path is performed using temperature and heat flux data from the road tests. To assess the accuracy of the convection and radiation components, an isolated thermal network consisting of only the baseplate to the environment is created as shown in Figure 6.25.

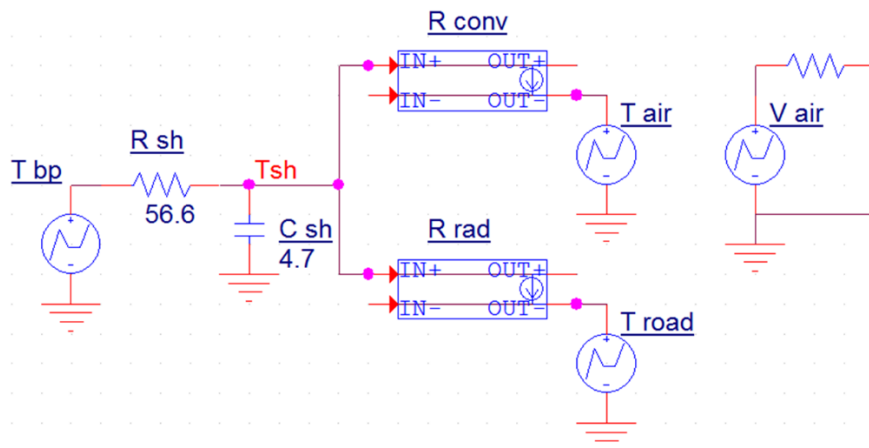


Figure 6.25 - Baseplate environment test network

The measurement points taken during the road test are as follows: the outer baseplate surface temperature  $T_{bp}$  (under the shield), the air temperature at approximately 10 cm below the shield ( $T_{air}$ ), and the road temperature recorded during the stationary test by a thermocouple taped to the pavement ( $T_{road}$ ). The  $V_{air}$

source is the underbody air speed input which is approximated by the vehicle forward speed reading taken from the CAN bus during driving tests, and the average wind speed during the time of testing (from Environment Canada database) is used as the input for static tests. The rate of heat flow through the baseplate, measured by heat flux sensors, is used to validate the reduced test network. By defining the temperature difference across each branch, the only unknown is the total rate of heat flow through the baseplate. If the modelling of the radiation and convection components is sound, the heat flow in the simulation should match the measurement.

Two road tests are used for validation. The first is a parking lot heat soak (Run #3), where the vehicle is parked in the sun for an afternoon, and the second test is a normal city drive with traffic as well as some rural highway driving (Run #2). The use of these two drastically different scenarios allows for thorough testing of the accuracy of the convection modelling.

### ***Parking Lot Heat Soak***

In this test, the vehicle was stationed in a sunny parking lot for a portion of the afternoon. The temperature inputs are shown in the top half of Figure 6.26. The air velocity is entered as the average wind speed during each hour of the test. For example, the test began at 1:43 pm, and the corresponding air speed for that hour was 4.44 m/s. During the next hour, the average hourly wind speed increased to 4.72 m/s. The road temperature profile decreases from 1800 to 3700 s (Troad) which is the result of poor sensor placement during the test; more detailed explanation is provided subsequently in Section 6.5.1. The heat flow per cell (in mW) entering the baseplate is shown in the bottom portion of the figure.

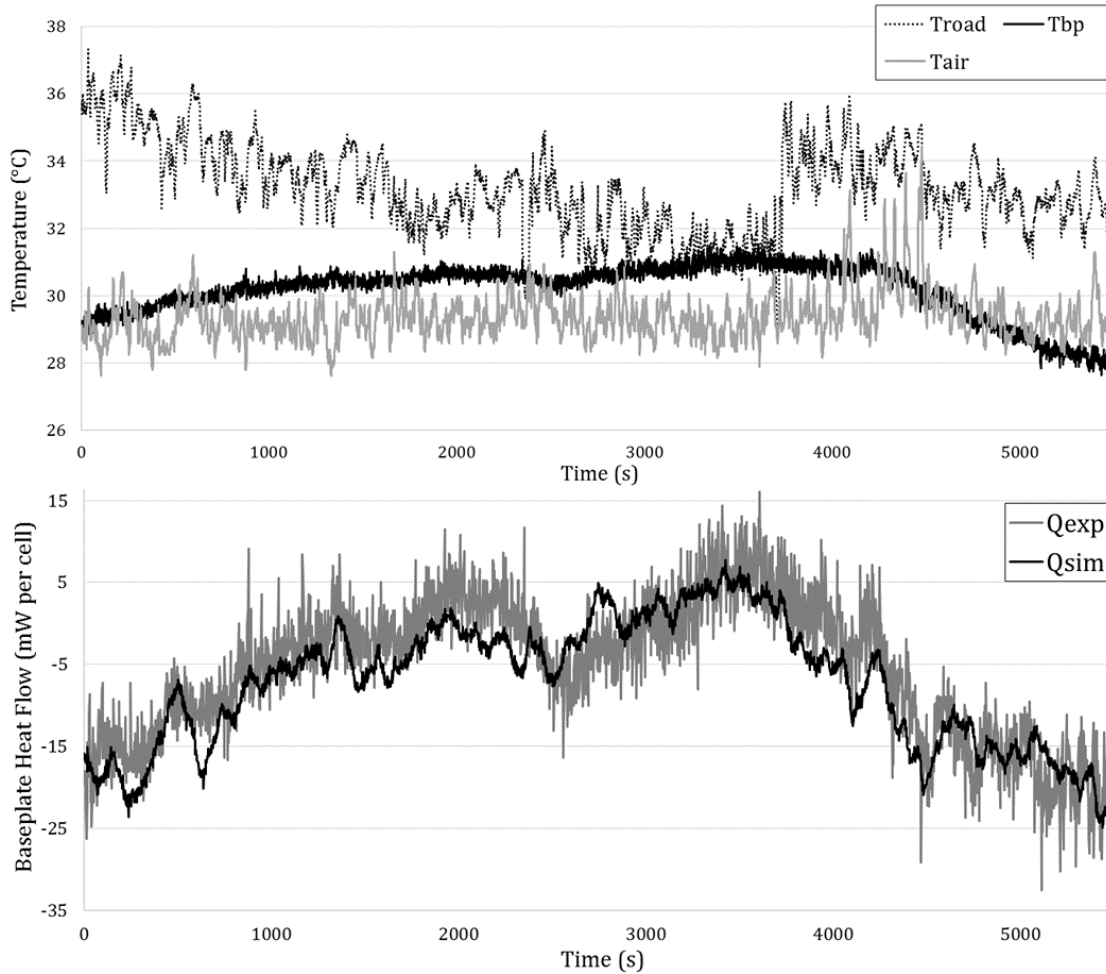


Figure 6.26 – Static parking lot test temperature conditions (top) and experimental vs simulation baseplate heat flow in mW per cell (bottom)

The results of the heat flow through the baseplate path during the parking lot test prove satisfactory considering the assumptions made during modelling.

### ***Commuting Drive Cycle***

This drive cycle consists of stop-and-go driving and highway driving at speeds around 90 km/h. Figure 6.27 shows the input air speed (top) along with the input temperature sources (bottom). The road temperature is estimated to vary linearly between a starting and ending temperature. The ending temperature was defined as 35.6 °C, which is by measurement taken at the end of the test. The starting temperature is assumed to be 30 °C, which is based on other experiments with similar conditions.

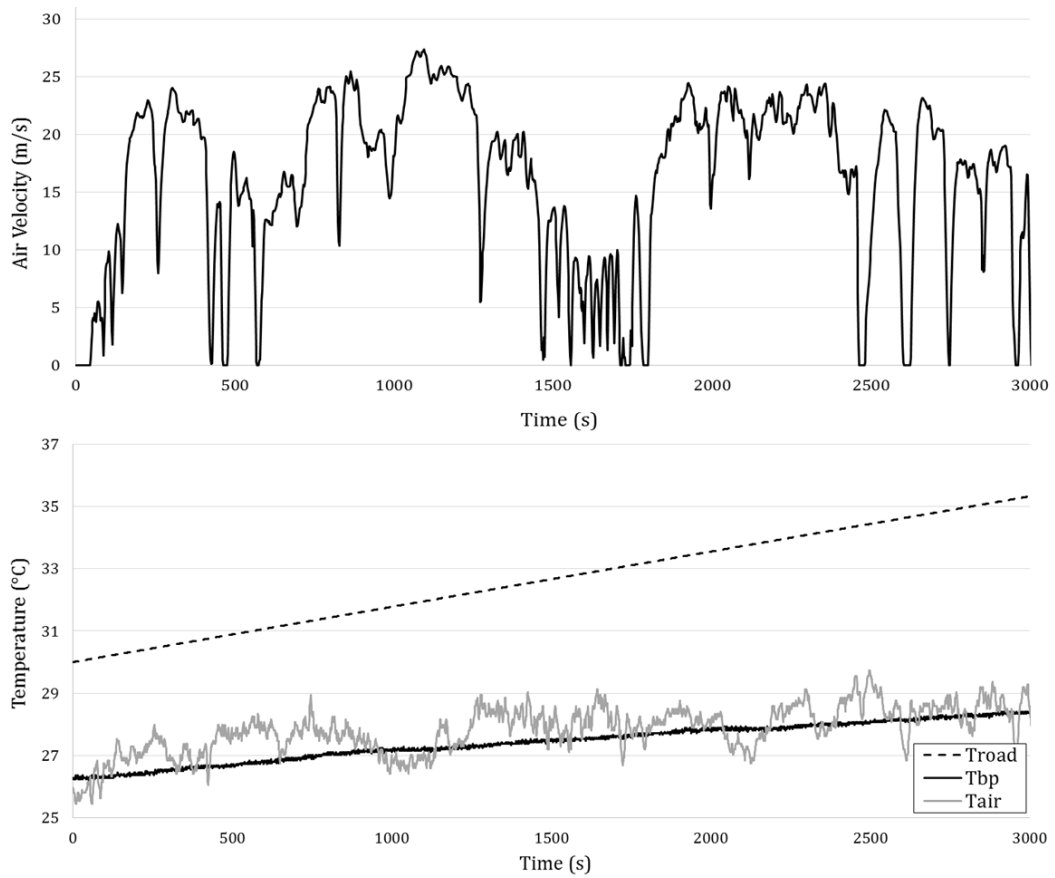


Figure 6.27 - Commuting drive cycle inputs: air speed in m/s (top) and temperature sources (bottom)

Inputting the source profiles as shown into the test circuit from Figure 6.25 yields the heat flow results shown in Figure 6.28.

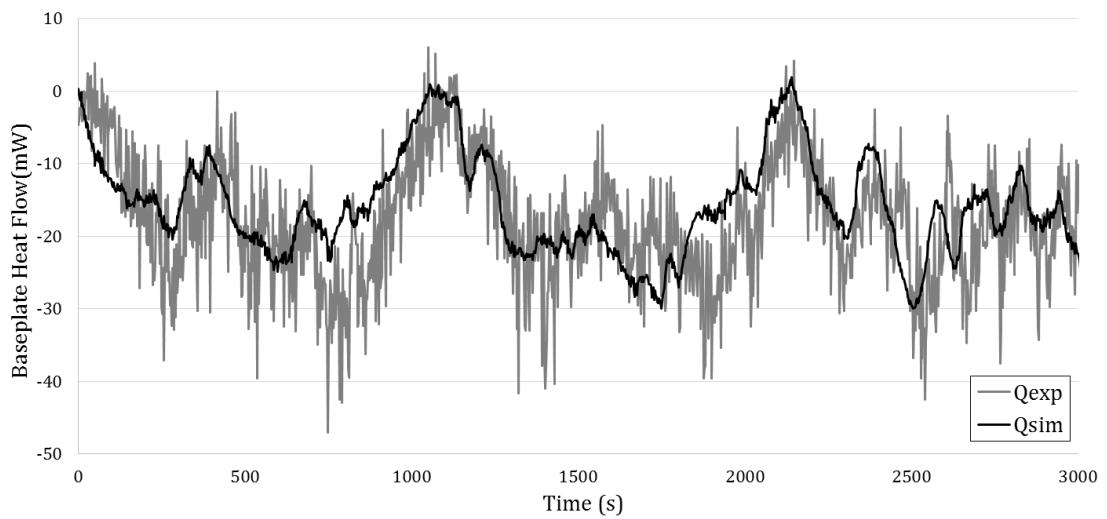


Figure 6.28 - Heat flow out of baseplate (mW per cell): experimental vs simulation

Figure 6.28 compares the simulated heat flow with the readings from the heat flux sensors. The values represent the heat flow exiting the baseplate on a per-cell basis. The negative values indicate that heat is flowing from the environment to the baseplate. The simulation mimics the real system fairly accurately considering the assumptions for wind speed and road temperature. Based on the favourable results seen from two separate tests, and for the purposes of validating this method, the results are deemed acceptable.

#### **6.4.4 Summary**

In this section, the three exterior paths of the laboratory-validated thermal model were modified to match the external conditions on the vehicle using data gathered during road testing. The ambient conditions of the bulkhead were similar enough to the lab situation that the use of the existing variable resistor was deemed sufficient. The outer cover resistance was derived mathematically and implemented using a voltage-controlled current source. A resistor and capacitor were added to the baseplate path to represent the plastic shield. Convection between the baseplate and road was modelled based on vehicle speed and underbody air temperature. Radiation effects from the road were modelled based on the road and baseplate temperature. The convection and radiation resistances were implemented by programming their respective governing heat transfer equations into voltage-controlled current sources. The modelling methods in turn provided satisfactory results where experimental validation was possible. The resultant thermal model with the adaptations described in this section is shown in Figure 6.29. This model is used to produce the results presented in the subsequent section.



Rather, a 3<sup>rd</sup> research student will use the balance of road tests to validate the full battery pack thermal model (including the interior of the modules) combined with a powertrain model. Since test run #3 consists of a heat soak of the stationary vehicle, the effects of battery heat generation are minimal with the vast majority of heat transfer being affected by construction of the cell module surroundings and the environment. This test can therefore be used to validate the model presented.

The environmental temperature sources  $T_{eng}$ ,  $T_{chassis}$ ,  $T_{air}$ , and  $T_{road}$  were measured using the methods described in Sections 6.3 and 6.4. Additionally, the inlet fluid temperature source  $T_{in}$  was taken from the vehicle CAN bus recordings. These five input temperature sources are displayed in Figure 6.30. One event of interest during the test is around 4200 s, which corresponds to when the vehicle's battery cooling system turns on, and the inlet fluid temperature decreases very rapidly. During the time span 1800-3700 s, the road thermocouple began to peel, eventually breaking free from the road. This is cause of the dip in measured road temperature seen during this time. An alternative method for measuring road temperature would be to employ an infrared thermometer, which would allow for surface temperature measurement while the vehicle is in motion.

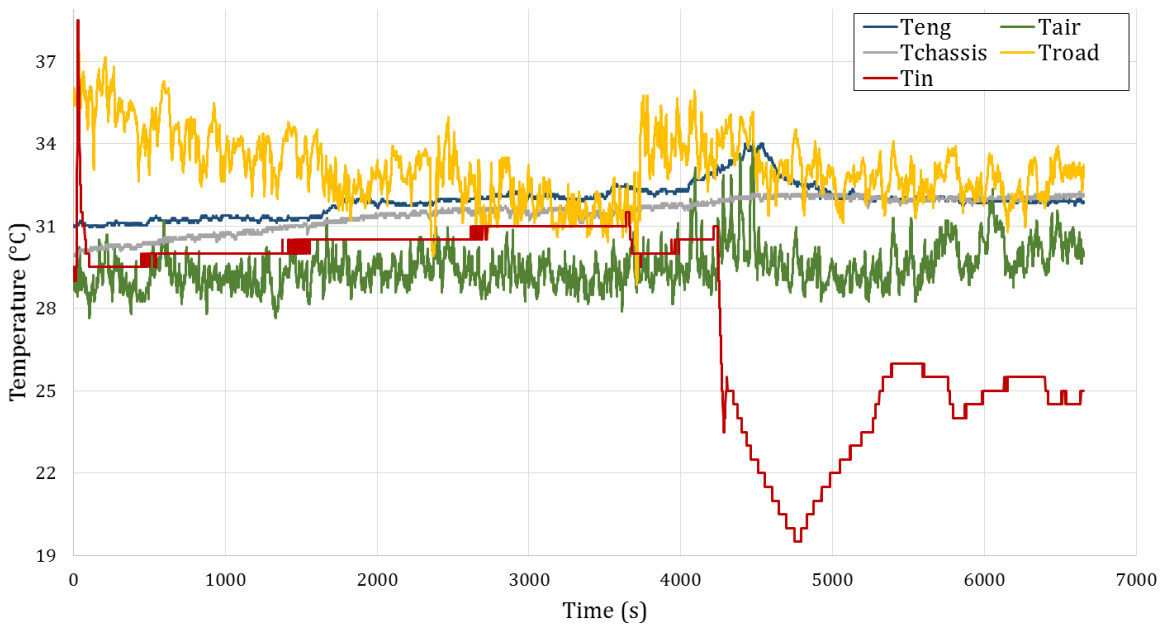


Figure 6.30 - Input temperature sources for parking lot heat soak

### 6.5.1 Results

As discussed in Chapter 6.3, the measurement points accessible on a rental vehicle were limited mainly to the baseplate region and different air temperatures. Since the air temperatures represent environmental sources, the baseplate is the main area of focus in the verification of the thermal model. A comparison of experimental and simulated baseplate temperatures is shown in Figure 6.31. The simulation matches the experimental measurement rather well, with an absolute maximum error of 0.57 °C and an RMS error of 0.21 °C. The effects of the dip in road temperature mentioned earlier is most noticeable from 2500-3600 s. This is an experimental error caused by poor sensor placement. At 2436 s into the test, the vehicle was moved forward but the road temperature sensor was placed incorrectly thereafter. The thermocouple was not making full contact with the pavement, and registered a temperature that was lower than the actual road temperature. The vehicle was moved again at 3815 s, and the sensor was positioned correctly afterwards. This later event can be seen clearly in Figure 6.30 where the road temperature sharply increases approximately 4 °C.

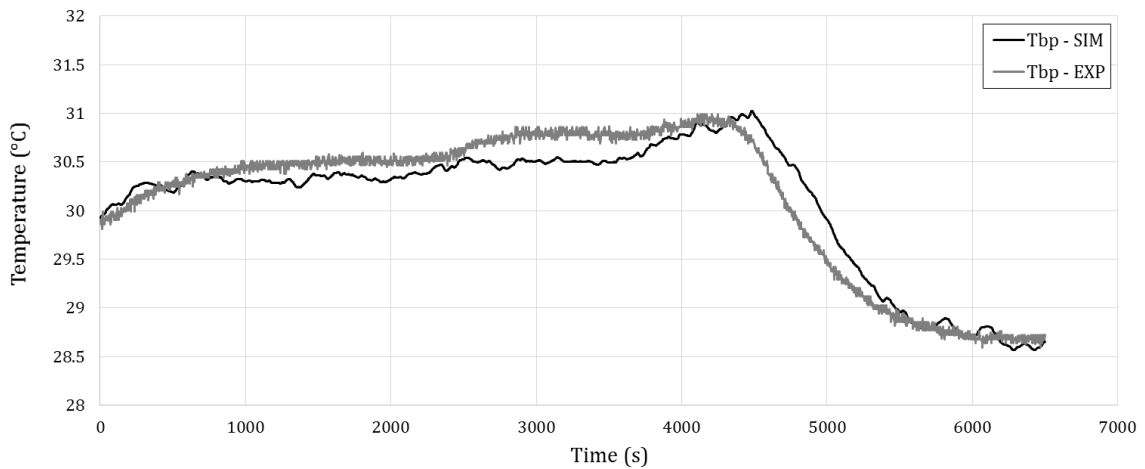


Figure 6.31 - Baseplate temperature: experimental vs simulation during heat soak

After the cooling system turns on, at 4195 s, the simulation lags by 140 s, which is maintained while the cooling system is in operation. The maximum error occurs here, but remains mostly below 0.5 °C until the simulation converges with the measured

value shortly after. This level of error in temperature is very close to the accuracy achieved in the lab setting.

The baseplate heat flow results in mW per cell are presented in Figure 6.32 below.

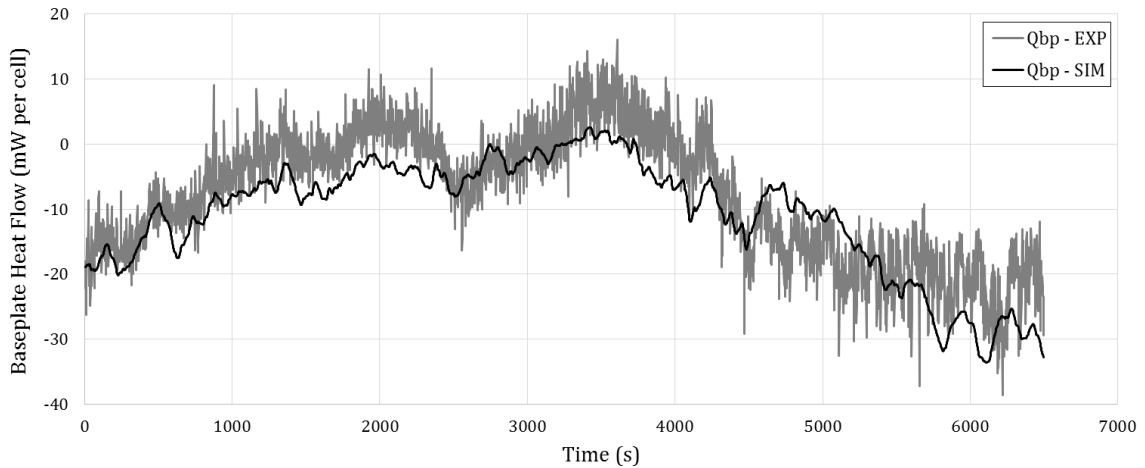


Figure 6.32 –Baseplate heat flow: experimental vs simulation during heat soak

The maximum absolute error is 20.7 mW occurring at 5100 s. The large absolute errors are mainly due to the low signal-to-noise ratio of the heat flux measurement. The RMS error is 6.1 mW, which is comparable to the 6.9 mW noise level of the measurement signal. Such level of error is again similar to what was achieved in the lab setting.

To further investigate the efficacy of the thermal model, two other areas relating to the cooling system are examined. The first is the average fluid temperature, shown in Figure 6.33. The experimental value is the mean temperature of the inlet and outlet fluid, extracted from the CAN bus. The simulation follows the measurement trace fairly accurately. The simulation exhibits a smoother response since it represents the mean fluid temperature averaged throughout the battery pack. In the vehicle, fluid temperatures are measured close to the front of the battery pack, and the average is instantly influenced by a change in inlet temperature. The resolution of the temperature measurements on the vehicle via CAN bus is 0.5 °C, which is another cause for the choppiness of the experimental values.

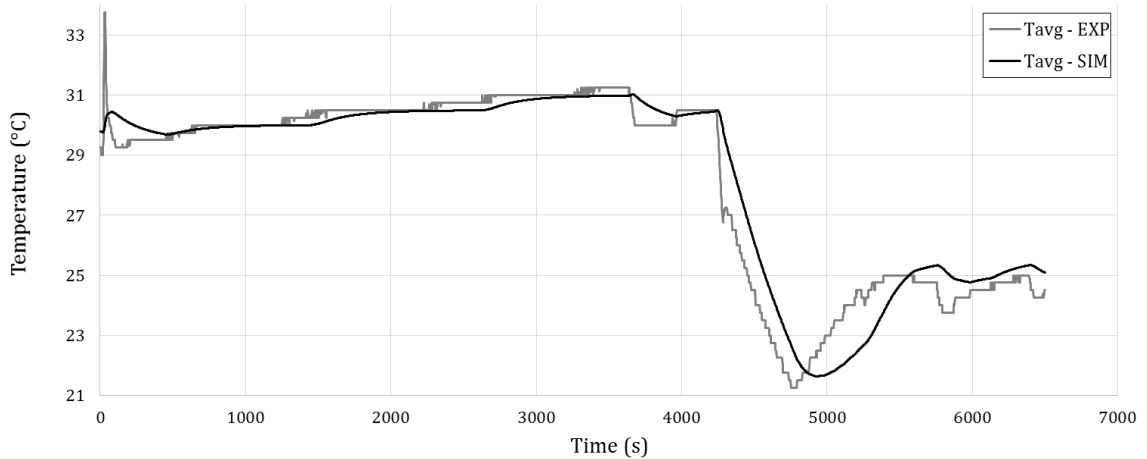


Figure 6.33 - Average fluid temperature during heat soak test: experimental vs simulation

The second area of examination is the thermal power requirement when the cooling system is in operation. If the system is modelled correctly, the current being pulled from the circuit by the voltage source  $T_{in}$  (i.e. cooling power  $\dot{Q}_{in}$ ) should scale to the input power of the vehicle's A/C compressor ( $\dot{W}_{comp}$  taken from the CAN bus). The thermal system power and the fluid source current from the model, in W per cell, are shown in Figure 6.35. The inlet fluid temperature (black line) is also plotted to provide context for the differences in behaviour.

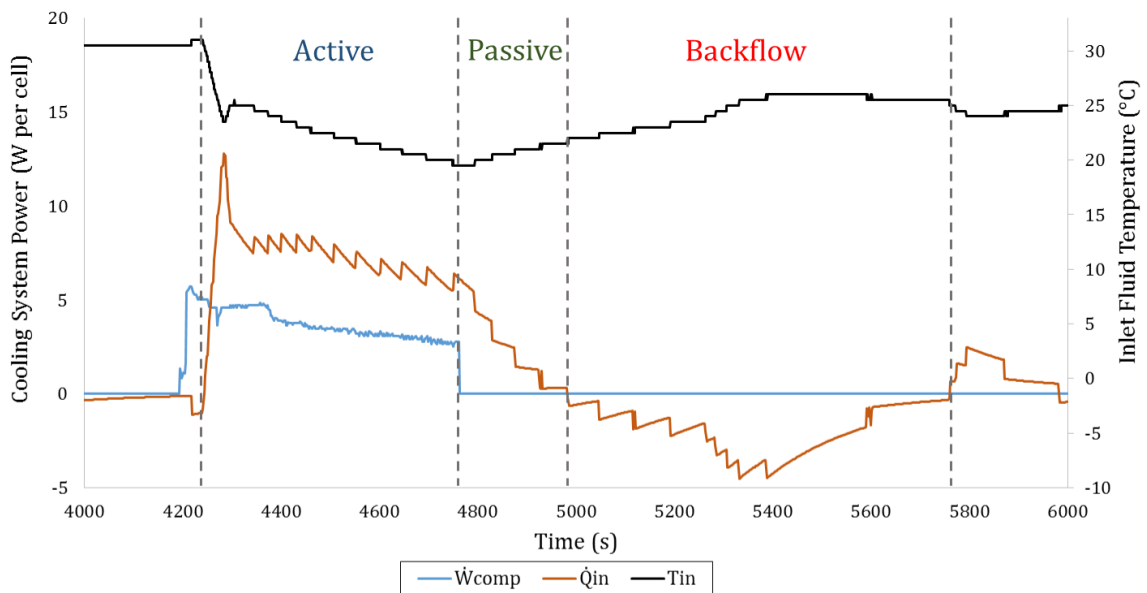


Figure 6.34 – Comparison of A/C compressor power to simulation input source heat flow (W per cell) with correlated inlet fluid temperature

The initial cooling power is used to begin the refrigeration cycle and cool the fluid in the refrigerant/glycol heat exchanger. The fluid must then circulate to the battery pack, where it can begin cooling the cells, thus resulting in a time delay. This can also be confirmed by observing the inlet fluid temperature lag relative to the compressor power profile (~45 s). One aspect to note is that the experimental value represents only the active cooling power input to the battery cooling system and does not include the passive cooling effects due to the re-circulating fluid after compressor shutdown. For this reason,  $\dot{W}_{comp}$  drops to zero and remains there after the active cooling stops. The “passive cooling” period has been identified on Figure 6.34. During this time, the fluid is below the cell temperature and provides additional cooling due to the thermal inertia of the coolant. Consequently, the heat contained in the cell packaging cascades back into the fluid, beginning the “backflow” phase.  $\dot{Q}_{in}$  turns negative which represents the re-emergence of heat energy from the packaging working its way back into the cells and coolant. While this is not a direct comparison of the system operation, it does indicate that the model can provide valuable information relating to the vehicle thermal system’s actual cooling power delivered.

By comparing the simulated battery pack cooling profile ( $\dot{Q}_{in}$ ) to the electrical power consumption of the vehicle’s A/C compressor ( $\dot{W}_{comp}$ ) during the “active cooling” period, information about the cooling system’s coefficient of performance (COP) can be extracted using Equation (6.11).

$$COP = \frac{\text{Cooling power}}{\text{Input power}} = \frac{\dot{Q}_{in}}{\dot{W}_{comp}} \quad (6.11)$$

Figure 6.35 compares the same cooling profiles as Figure 6.34, but focuses on the “active cooling” portion of the curves. The resulting COP is plotted with its scale on the right-hand side of the graph.

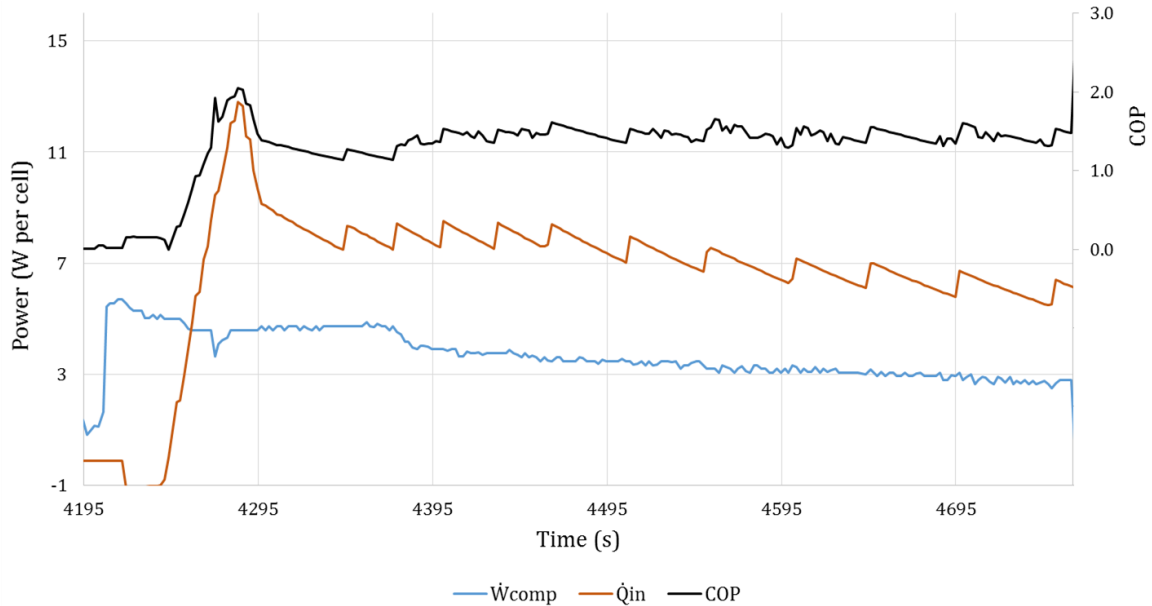


Figure 6.35 – Power profiles ( $\dot{Q}_{in}$  and  $\dot{W}_{comp}$ ) during active cooling with corresponding COP

The COP of the system based on the simulation response was calculated to be 1.44 on average. This means the amount of cooling provided to the battery pack is approximately 44% higher than the electrical power input to the compressor. Such information can prove useful in thermal system design and component selection. For example, the required cooling power for a given battery temperature pulldown rate can be estimated by defining the desired inlet temperature as an input to the simulation. This gives an idea of the effective power requirements of the cooling system, and allows the designer to size the system accordingly. Electrical power consumption of the cooling system can then be estimated based on battery cooling requirements derived from simulated environment exposures and drive cycle combinations, in conjunction with the fluid cooling method/hardware employed.

Conversely, the battery cooling performance of an alternative system can be analyzed by defining the input fluid source heat rate rather than temperature. The effects of cooling power on the battery temperature pulldown rates could provide set-point information which would be useful in designing the BTMS control strategy. When coupled to a full powertrain simulation, this thermal model could shed light on the

effects of cooling strategies (hardware and control) on vehicle range and energy consumption during any custom or standardized drive cycle.

## 6.6 SUMMARY

The purpose of this chapter was to extend the functionality of the battery pack thermal model developed in the previous chapters, from a static laboratory setting to the dynamic environment of a real vehicle. This was achieved by splitting the single lab environmental source into three separate paths: engine compartment to bulkhead, vehicle chassis to cover, and underbody to baseplate. These new paths contain temperature sources and corresponding thermal resistances that replace their respective components in the lab model.

In order to capture and understand the new thermal conditions, a week-long series of road tests were conducted during the month of August 2015. Thermal measurements were gathered with thermocouples and heat flux sensors and the air speed under the vehicle was measured using a CTD hot-film anemometer. The vehicle CAN bus was also monitored using an OBD-II scan tool in order to gather powertrain and thermal system information concurrently.

Based on the thermocouple measurements taken in front of the bulkhead, it was theorized and shown that the level of convection was minimal due to the structures surrounding the bulkhead. As a result, the same variable resistor  $R_{obh}$  developed for the lab model could be utilized in the new vehicle model.

For the cover, the external environment was considered to be the air gap between it and the vehicle chassis. The chassis temperature was used as the voltage source inside the thermal model and its corresponding thermal resistance was derived mathematically based on heat transfer between parallel plates. The radiation and conduction equations were used to generate a resistance lookup table based on cover temperature, which was programmed into a voltage-controlled current-source that effectively mimics a variable resistor  $R_{oc}$ .

The environmental conditions between the baseplate and underbody were split into forced convection  $R_{conv}$  and radiation  $R_{rad}$  paths. The road temperature  $T_{road}$  was used as the radiation source, and its variable thermal resistance was also modelled using a voltage-controlled current-source. The convection path was modelled as forced air, at temperature  $T_{air}$ , flowing over a flat plate. Based on road testing data, the air velocity under the baseplate was determined to be comparable to the vehicle's forward speed. For both  $R_{rad}$  and  $R_{conv}$ , the governing heat-transfer equations were programmed into their respective variable resistors. Voltage-controlled current-sources were used to directly output the required current (heat flow) based on the baseplate, air, and road temperatures. An additional separate input source  $V_{air}$  is used to pass the recorded vehicle and wind speed into the simulation and utilized in the  $R_{conv}$  calculation. Both baseplate environmental paths were successfully verified using heat flux and temperature data taken from a heat soak and a drive cycle.

The full model was then verified by comparing the simulation to measured data from a parking lot heat soak test. Simulated baseplate temperature and heat flux matched the experimental measurements within similar error bands as experienced in the lab. Additionally, the model was able to reproduce valuable thermal system information such as average fluid temperature and total cooling power delivered. Based on the available data taken from the road tests, the extension of the battery pack thermal model from the lab to the real vehicle installation was deemed successful.

## 7 CONCLUSION

---

### 7.1 SUMMARY

A brief introduction to thermal management of EVs was presented, outlining the motivation behind the improvement of BTMS operation and understanding the effects of the environment on battery function. A review of thermal modelling methods was presented along with a review of battery pack models found in the literature. The modelling of the battery pack's dynamic environment is usually very limited (generally ignored), which is one of the main motivations for this project.

In Chapter 4, the general methods used for measuring thermal resistance, and constructing the thermal network were presented. A preliminary steady-state network was shown in Chapter 5, along with necessary refinements that improved model performance. The initial fixed ambient source resistors (bulkhead, cover, and baseplate) were replaced by variable resistors which are dependent on the temperature difference between the component surface and ambient temperature. Resistor "tolerances" were established based on measurement uncertainties, and each individual resistor was tuned within its specified tolerance. These refinements lowered the steady-state errors within acceptable limits.

Thermal dynamics were then introduced by adding capacitors to the thermal circuit. The fluid heat source was modified to mimic the nature of a true fluid source. A current limit based on the maximum heating power of the fluid was applied to the inlet temperature source. The capacitor value representing the thermal mass of the interior of the modules was determined by matching the inlet source current to the measured heat absorption of the battery pack during the initial transient heating period in the lab tests. The transient responses of the model were then compared to experimental measurements with acceptable results.

In Chapter 6, the lab-based battery pack model was adapted to suit the environment of the real vehicle. The environmental temperature sources (excluding coolant temperature) were modified based on observations made during a series of road tests. The underbody source was split into a convection and a road radiation component. The convection resistance is dynamically dependent on both air temperature and air speed (approximated by vehicle speed). The radiation source varies with pavement temperature. This new thermal model was validated through road testing data. Due to the limitations of testing on a rental vehicle, only the temperature and heat flow of the baseplate were directly verified, but were in good agreement with experimental measurements. The model was also able to produce the average fluid temperature within acceptable error.

## **7.2 CONCLUSIONS**

The initial literature review demonstrated the lack of full battery pack thermal models, especially ones that can execute in real time. The experimental method described in Chapter 4 was shown to be an effective way to create a thermal network model. During transient lab tests, the model is accurate to 0.6 °C RMS for component temperatures, and errors in heat flow are comparable to the level of signal noise (4-16% of signal level). The steady-state temperature errors are well within 0.5 °C, spanning the full testing temperature range, and heat flow errors are within 5% of their measured values; some outliers do exist due to varying experimental conditions (as explained in Section 5.2.3). The level of accuracy established in the lab setting is well within the range achieved by other experimentally validated models. This demonstrates that a structurally complex battery pack can be accurately modelled using the thermal circuit method. This accuracy relies heavily on the validity modelled thermal connections, assumptions about dominating modes of heat transfer, and the accuracy the RC parameter extraction techniques employed (experimental, theoretical, optimization fit, CAD simulation).

The modifications to the environmental sources carried out in Chapter 6 were shown to sufficiently mimic normal summer driving conditions, by comparing baseplate heat flow and temperatures during several road tests; simulation accuracy was comparable to that achieved in the transient lab tests.

Since the road testing was only conducted during a single week where temperatures ranged from 20-32 °C, the model has not yet been verified under colder conditions. The ambient resistors modelled here (minus the bulkhead) are derived from heat transfer theory, which adequately covers the temperature range of the winter months (down to -40 °C) and as such are expected to remain valid. The bulkhead resistor is modelled based on temperature difference, which is not expected to drastically differ from the testing conditions seen. The packaging component resistors are also not expected to change at lower temperatures, under the assumption that conventional material properties remain relatively constant over the temperature range under consideration. The only resistance and thermal capacitance that is expected to vary is that of the cells themselves; but the scope of this work is focused on modelling the pack construction and external influence conditions. Such refinements pertaining the cells can be added at a later stage. Additionally, colder weather virtually eliminates the road radiation path, reducing any errors associated with its modelling and influences.

The possible effects of rain on the heat transfer out of the battery pack have been neglected along with changes in humidity and variations in barometric pressure. These effects are not seen as particularly detrimental to the environment of the cells, but are rather beneficial due to an additional evaporative cooling effect, so predictions would remain conservative. The extent of verification carried out in this work spans a range of temperatures and ambient conditions, though certainly not all. Steps have been taken to minimize errors when employing the model outside this range, and as a result, the model is still expected to perform adequately down to around freezing. Certainly more verification work is still in order.

To the author's knowledge, this is the most structurally comprehensive battery pack thermal network model available in current public literature. The level of dynamic environmental modelling is also beyond the scope of other EV battery pack models. The Volt specific battery pack thermal network model developed is capable of solving lengthy drive cycle simulations very quickly using a variety of flexible inputs (ambient conditions and vehicle speed), making it compatible with the powertrain model in Autonomie. This fast solving speed also opens up the possibilities for use in BTMS controls.

The thermal network model's ability to provide cooling/heating requirements and system sizing information was briefly demonstrated, and the effects of physical design changes to the system can be analyzed relatively quickly as a result. These abilities allow for design iterations to be analyzed in terms of thermal performance (system COP, thermal time constants, and power requirements) and cost-effectiveness.

While the model presented in this thesis is specific to the Chevrolet Volt platform, the methods presented are still applicable to other battery packs given that sensor placement, measurement points, and circuit layout may be adjusted based on the construction of the battery pack to be modelled. Alternatively, in an engineering environment where a proposed battery pack assembly has been designed in CAD, FE and CFD packages can be used to generate an equivalent thermal circuit by employing a similar approach as described in this thesis. Resistances of complex 3D structures may be determined from heat flux across imaginary boundaries or "cutting planes" and the temperature differentials separating these key components, when driven from a heat source. Capacitor values are derived by summing the corresponding material properties and masses.

Any findings regarding battery pack design that can be extracted using the thermal model presented may also be applied to other liquid-cooled battery pack configurations, since the underlying principles do not change. This modelling approach as demonstrated should become a useful tool in better understanding the

thermal design implications of physical features and provide an outline for evaluation procedures in similar packs destined for EVs of the future.

### **7.3 CONTRIBUTIONS**

The major contribution here is the experimental development and refinement of a full battery pack thermal network model that considers detailed battery construction and realistic environmental effects. Through this process, it was shown that a complex system (structurally and dynamically) can be represented with reasonable accuracy, via a relatively simple thermal network. This model can be run faster than real time when incorporated in the vehicle powertrain simulation, and it considers road effects, ambient temperatures, and vehicle speed. The thermal network model can also be employed in conjunction with a powertrain model for further studies. Thus far, no such comprehensive simulation has been reported in the public domain, and it remains unique.

In Chapter 4, a simple method for measuring thermal resistance and generating a thermal network based on the physical layout is presented. The thermal resistance measurement technique presented here can be applied to other systems, as long as the heat flux sensors can be placed correctly. Alternatively, R and C values can be extracted from CAD simulations under the same principles as deployed in the experimental approach.

Practical considerations on the use of heat flux sensors were discussed, and solutions to improve measurement accuracy are provided. Issues regarding measuring temperature and heat flux on low emissivity surfaces were brought to light, and possible solutions were proposed. A detailed uncertainty analysis on direct and compound measurements was carried out, and presented in a manner that is relevant to modern data-acquisition methods (i.e. continuous measurement signal). This is an area which is commonly neglected or vaguely mentioned in the literature, but is a

valuable tool for understanding the significance of the measurements being carried out.

In Chapter 5, a simple method for modelling ambient resistances based on experimental measurements (convection and radiation effects) is developed using temperature-controlled resistors. Also, a method for implementing a heat flow-controlled temperature-source that mimics the behaviour of a fluid source is presented. This is achieved using a simple current limiter in line with an ideal voltage source, and respects the physics involved with heat transfer from a fluid source.

In Chapter 6, a simple method for implementing dynamic convection and radiation resistances in a SPICE (simulation program with integrated circuit emphasis) environment is presented. The technique is used to model radiation and convection under the vehicle. The result is a unique and elegant way to accurately simulate highly dynamic environmental conditions.

In sum, this collection of methods helps assemble a comprehensive battery pack system thermal network model that is experimentally verifiable and far surpasses the accuracy of any like attempt previously achieved.

## **7.4 FUTURE WORK**

One of the main tasks to wrap up the full battery pack thermal model is to implement the internal portion of the circuit (“Section A”), which should improve the transient response. This would allow cell heat generation to be better considered in the model. Additionally, the heating of the battery terminals could be added in as a heat source after the top frame resistor ( $R_{top1}$ ). More lab tests could be performed in the future, with the batteries electrically active to help verify these additions.

Thermal resistance and capacitance values can be refined more precisely by employing an optimization method to minimize the transient and steady-state errors

in the simulation. This could provide a slight improvement in overall model performance.

More comprehensive road tests on a vehicle whose battery pack may be removed would allow for better external resistance modelling and provide more validation points. Orienting an air flow sensor (with tube) perpendicular to the direction of travel would provide crosswind information and improve the estimate for total air flow. Placing hot-film anemometers and heat flux sensors around the cover and in front of the bulkhead would provide more than adequate modelling data. The full vehicle model (with integrated cell model) could then be completely validated using the road tests described in Chapter 6.

The gaps in cold weather validation can be filled in by conducting another set of comprehensive road tests in the winter months. This would help verify the modelling as well as provide more information regarding the vehicle and BTMS operation under these conditions.

Other model extensions considered might implement phase-change materials and/or a thermoelectric coolant device inside the battery. Physical design changes and isolation improvements can be made on the lab battery pack and assessed for effectiveness using the thermal network model. The model can be used to study the relative effects of adding insulation in different locations, which would help identify the most cost-effective strategies and provide performance metrics for these effects. Metrics such as thermal time constants, overall system COP, energy consumption, and power requirements can be extracted from the model and used for design analysis.

Combined with a suitable powertrain model, there are many other possible scenarios to investigate, with the ultimate aim of uncovering more efficient battery thermal management strategies, optimal constructions, and cost/benefit analysis of proposed alterations.

## REFERENCES

---

- [1] N. Javani, I. Dincer, G. F. Naterer, and G. L. Rohrauer, "Modeling of passive thermal management for electric vehicle battery packs with PCM between cells," *Appl. Therm. Eng.*, vol. 73, no. 1, pp. 305–314, 2014.
- [2] S. Petryna, "Model predictive control of a thermoelectric-based heat pump," University of Ontario Institute of Technology, 2013.
- [3] S. Petryna, J. M. Eklund, and G. Rohrauer, "Modelling a thermoelectric heat exchanger," in *Canadian Conference on Electrical and Computer Engineering*, 2013.
- [4] G. Clark, "Achieving high efficiency thermoelectric heating and cooling with metal foam heat exchangers," University of Ontario Institute of Technology, 2014.
- [5] J. Brennan, "Experimental and numerical quantification of EV and PHEV battery pack thermal isolation strategies," University of Ontario Institute of Technology, 2015.
- [6] L. Ramotar, G. L. Rohrauer, R. Filion, and K. MacDonald, "Experimental verification of a thermal equivalent circuit dynamic model on an extended range electric vehicle battery pack," *J. Power Sources*, vol. 343, pp. 383–394, 2017.
- [7] J. M. Miller, *Propulsion Systems for Hybrid Vehicles*, 2nd ed. Institution of Engineering and Technology, 2010.
- [8] USCAR, "Energy Storage System Goals," 2017. [Online]. Available: [http://www.uscar.org/guest/article\\_view.php?articles\\_id=85](http://www.uscar.org/guest/article_view.php?articles_id=85).
- [9] T. Yuksel, S. Litster, V. Viswanathan, and J. J. Michalek, "Plug-in hybrid electric vehicle LiFePO<sub>4</sub> battery life implications of thermal management, driving conditions, and regional climate," *J. Power Sources*, vol. 338, pp. 49–64, 2017.
- [10] T. Reddy, *Linden's Handbook of Batteries*, 4th ed. McGraw Hill Professional, 2010.
- [11] G. Nagasubramanian, "Electrical characteristics of 18650 Li-ion cells at low temperatures," *J. Appl. Electrochem.*, no. 31, pp. 99–104, 2001.
- [12] T. Saxton, "Plug In America's LEAF Battery Survey," 2012.
- [13] A. A. Pesaran, "Battery thermal models for hybrid vehicle simulations," *J. Power Sources*, vol. 110, no. 2, pp. 377–382, 2002.
- [14] I. N. Laboratory, "Hybrid Electric Vehicles," *Advanced Vehicle Testing Activity*, 2017. [Online]. Available: <https://avt.inl.gov/vehicle-type/hev>.
- [15] I. N. Laboratory, "Plug-in Hybrid Electric Vehicles/Extended Range Electric Vehicles," *Advanced Vehicle Testing Activity*, 2017. [Online]. Available: <https://avt.inl.gov/vehicle-type/phev>.

- [16] G. Cho, J. Choi, J. Park, and S. Cha, "Transient modeling and validation of lithium ion battery pack with air cooled thermal management system for electric vehicles," *Int. J. Automot. ...*, vol. 15, no. 5, pp. 795–803, 2014.
- [17] M. Zolot, A. a. Pesaran, and M. Mihalic, "Thermal Evaluation of Toyota Prius Battery Pack," *SAE Int.*, Jun. 2002.
- [18] M. Zolot, K. Kelly, M. Keyser, M. Mihalic, A. Pesaran, and A. Hieronymus, "Thermal evaluation of the Honda insight battery pack," *Intersoc. ...*, no. June, 2001.
- [19] R. Matthe, L. Turner, and H. Mettlach, "VOLTEC battery system for electric vehicle with extended range," *SAE Int.*, 2011.
- [20] R. Parrish, K. Elankumaran, M. Gandhi, and B. Nance, "Voltec battery design and manufacturing," *SAE Int.*, 2011.
- [21] A. Faass and E. Clough, "Battery module with integrated thermal management system," US20130196184A1, 2013.
- [22] B. Scrosati, J. Garche, and W. Tillmetz, *Advances in Battery Technologies for Electric Vehicles*. Woodhead Publishing Limited, 2015.
- [23] P. Nelson, D. Dees, K. Amine, and G. Henriksen, "Modeling thermal management of lithium-ion PNGV batteries," *J. Power Sources*, vol. 110, no. 2, pp. 349–356, Aug. 2002.
- [24] R. Carlson, M. Duoba, D. Bocci, and H. Lohse-Busch, "On-Road Evaluation of Advanced Hybrid Electric Vehicles over a Wide Range of Ambient Temperatures," *EVS23*, 2007.
- [25] J. Smart, "Advanced Vehicle Testing Activity – Cold Weather On-road Testing of a 2012 Chevrolet Volt," 2014.
- [26] D. Ghosh, P. D. Maguire, and D. X. Zhu, "Design and CFD Simulation of a Battery Module for a Hybrid Electric Vehicle," *SAE Int.*, Apr. 2009.
- [27] D. Ghosh, K. King, and B. Schwemmin, "Full Hybrid Electrical Vehicle Battery Pack System Design , CFD Simulation and Testing," *SAE Int.*, Apr. 2010.
- [28] H. Park, "A design of air flow configuration for cooling lithium ion battery in hybrid electric vehicles," *J. Power Sources*, vol. 239, pp. 30–36, Oct. 2013.
- [29] H. Sun, X. Wang, B. Tossan, and R. Dixon, "Three-dimensional thermal modeling of a lithium-ion battery pack," *J. Power Sources*, vol. 206, pp. 349–356, 2012.
- [30] R. Mahamud and C. Park, "Reciprocating air flow for Li-ion battery thermal management to improve temperature uniformity," *J. Power Sources*, vol. 196, no. 13, pp. 5685–5696, 2011.
- [31] K. Yu, X. Yang, Y. Cheng, and C. Li, "Thermal analysis and two-directional air flow thermal management for lithium-ion battery pack," *J. Power Sources*, vol. 270, pp. 193–200, 2014.

- [32] L. Fan, J. M. Khodadadi, and A. A. Pesaran, "A parametric study on thermal management of an air-cooled lithium-ion battery module for plug-in hybrid electric vehicles," *J. Power Sources*, vol. 238, pp. 301–312, 2013.
- [33] P. Cicconi, M. Germani, and D. Landi, "Modeling and thermal simulation of a PHEV battery module with cylindrical LFP cells," *World Electr. Veh. J.*, vol. 6, no. 1, pp. 175–185, 2013.
- [34] L. W. Jin, P. S. Lee, X. X. Kong, Y. Fan, and S. K. Chou, "Ultra-thin minichannel LCP for EV battery thermal management," *Appl. Energy*, vol. 113, pp. 1786–1794, Jan. 2014.
- [35] A. Greco, D. Cao, X. Jiang, and H. Yang, "A theoretical and computational study of lithium-ion battery thermal management for electric vehicles using heat pipes," *J. Power Sources*, vol. 257, pp. 344–355, 2014.
- [36] G.-H. Kim and A. Pesaran, "Battery Thermal Management System Design Modeling," *22nd Int. Batter. Hybrid Fuel Cell Electr. Veh. Conf. Exhib. EVS22*, vol. 1, no. November, pp. 126–133, 2006.
- [37] N. Javani, I. Dincer, G. F. Naterer, and B. S. Yilbas, "Heat transfer and thermal management with PCMs in a Li-ion battery cell for electric vehicles," *Int. J. Heat Mass Transf.*, vol. 72, pp. 690–703, 2014.
- [38] S. Nategh, Z. Huang, and A. Krings, "Thermal Modeling of Directly Cooled Electric Machines Using Lumped Parameter," *IEEE Trans. Energy Convers.*, vol. 28, no. 4, pp. 979–990, 2013.
- [39] X. Hu, S. Lin, S. Stanton, and W. Lian, "A Foster network thermal model for HEV/EV battery modeling," *IEEE Trans. Ind. Appl.*, vol. 47, no. 4, pp. 1692–1699, 2011.
- [40] A. Pesaran, A. Vlahinos, and S. D. Burch, "Thermal Performance of EV and HEV Battery Modules and Packs," *Fourteenth Int. Electr. Veh. Symp.*, no. September, 1997.
- [41] C. Lin, K. Chen, F. Sun, P. Tang, and H. Zhao, "Research on thermo-physical properties identification and thermal analysis of EV Li-ion battery," *5th IEEE Veh. Power Propuls. Conf. VPPC '09*, pp. 1643–1648, 2009.
- [42] A. R. Mayyas, M. Omar, P. Pisu, A. Mayyas, A. Alahmer, and C. Montes, "Thermal modeling of an on-board nickel-metal hydride pack in a power-split hybrid configuration using a cell-based resistance-capacitance, electro-thermal model," *Int. J. Energy Res.*, vol. 37, pp. 331–346, 2013.
- [43] G. Karimi and X. Li, "Thermal management of lithium-ion batteries for electric vehicles," *Int. J. Energy Res.*, vol. 37, pp. 13–24, 2013.
- [44] S. Zhang, R. Zhao, J. Liu, and J. Gu, "Investigation on a hydrogel based passive thermal management system for lithium ion batteries," *Energy*, vol. 68, pp. 854–861, 2014.
- [45] T.-H. Tran, S. Harmand, and B. Sahut, "Experimental investigation on heat pipe cooling for Hybrid Electric Vehicle and Electric Vehicle lithium-ion battery," *J. Power Sources*, vol. 265, pp. 262–272, 2014.

- [46] C. Mi, B. Li, D. Buck, and N. Ota, "Advanced electro-thermal modeling of lithium-ion battery system for hybrid electric vehicle applications," *Veh. Power Propuls. ...*, 2007.
- [47] H. Khasawneh, J. Neal, M. Canova, Y. Guezennec, R. Wayne, J. Taylor, M. Smalc, and J. Norley, "Analysis of heat-spreading thermal management solutions for lithium-ion batteries," in *ASME 2011 International Mechanical Engineering Congress and Exposition, IMECE 2011*, 2011, vol. 4, no. PARTS A AND B, pp. 421–428.
- [48] A. R. Mayyas, M. Omar, P. Pisu, A. Al-Ahmer, A. Mayyas, C. Montes, and S. Dongri, "Comprehensive thermal modeling of a power-split hybrid powertrain using battery cell model," *J. Power Sources*, vol. 196, no. 15, pp. 6588–6594, 2011.
- [49] Y. A. Çengel, *Heat and mass transfer: a practical approach*. McGraw-Hill, 2007.
- [50] F. P. Incropera, D. P. DeWitt, T. L. Bergman, and A. S. Lavine, *Fundamentals of Heat and Mass Transfer*, 6th ed. 2007.
- [51] M. N. Ozisik, *Heat Conduction*, 2nd ed. Raleigh, North Carolina: John Wiley & Sons, 1993.
- [52] J. . Holman, *Heat transfer*, 10th ed. New York: McGraw-Hill, 2010.
- [53] K. M. Letherman, "A Rational Criterion for Accuracy of Modelling of Periodic Heat Conduction in Plane Slabs," *Build. Environ.*, vol. 12, pp. 127–130, 1977.
- [54] M. M. Gouda, S. Danaher, and C. P. Underwood, "Low-order model for the simulation of a building and its heating system," *Build. Serv. Eng. Res. Technol.*, vol. 21, no. 3, pp. 199–208, 2000.
- [55] D. A. Coley and J. M. Penman, "Second order system identification in the thermal response of real buildings. Paper II: Recursive formulation for on-line building energy management and control," *Build. Environ.*, vol. 27, no. 3, pp. 269–277, 1992.
- [56] J. A. Crabb, N. Murdoch, and J. M. Penman, "A simplified thermal response model," *Build. Serv. Eng. Res. Technol.*, vol. 8, pp. 13–19, 1987.
- [57] P. Butler and K. M. Letherman, "A criterion for the accuracy of modelling of transient heat conduction in plane slabs," *Build. Environ.*, vol. 15, no. 3, pp. 143–149, 1980.
- [58] S. Barbaro, C. Giaconia, and A. Orioli, "Analysis of the accuracy in modelling of transient heat conduction in plane slabs," *Build. Environ.*, vol. 21, no. 2, pp. 81–87, 1986.
- [59] E. H. Mathews, P. G. Richards, and C. Lombard, "A first-order thermal model for building design," *Energy Build.*, vol. 21, no. 2, pp. 133–145, 1994.
- [60] M. G. Davies, "Optimum design of resistance and capacitance elements in modelling a sinusoidally excited building wall," *Build. Environ.*, vol. 18, no. 1–2, pp. 19–37, 1983.
- [61] A. P. Ramallo-González, M. E. Eames, and D. A. Coley, "Lumped parameter models for building thermal modelling: An analytic approach to simplifying complex multi-layered constructions," *Energy Build.*, vol. 60, pp. 174–184, 2013.

- [62] X. Xu and S. Wang, "Optimal simplified thermal models of building envelope based on frequency domain regression using genetic algorithm," *Energy Build.*, vol. 39, no. 5, pp. 525–536, 2007.
- [63] G. Fraisse, C. Viardot, O. Lafabrie, and G. Achard, "Development of a simplified and accurate building model based on electrical analogy," *Energy Build.*, vol. 34, pp. 1017–1031, 2002.
- [64] S. Wang and X. Xu, "Simplified building model for transient thermal performance estimation using GA-based parameter identification," *Int. J. Therm. Sci.*, vol. 45, no. 4, pp. 419–432, 2006.
- [65] C. P. Underwood, "An improved lumped parameter method for building thermal modelling," *Energy Build.*, vol. 79, pp. 191–201, 2014.
- [66] S. Karagol and M. Bikdash, "Generation of equivalent-circuit models from simulation data of a thermal system," *IEEE Trans. Power Electron.*, vol. 25, no. 4, pp. 820–828, 2010.
- [67] J. Galloway and S. Shidore, "Implementing Compact Thermal Models Under Non-Symmetric Trace Routing Conditions."
- [68] D. V Malyna, J. A. Ferreira, J. L. Duarte, P. Bauer, P. E. Group, E. Power, and P. Group, "Combined Electrical and Thermal Modeling in Power Supplies," *Power*, pp. 1–10, 1898.
- [69] R. Wrobel, N. Mcneill, and P. Mellor, "Performance Analysis and Thermal Modeling of a High Energy Density Pre-Biased Inductor," vol. 57, no. 1, pp. 1–8, 2009.
- [70] G. Swift, T. S. Molinski, and W. Lehn, "A fundamental approach to transformer thermal modeling - Part I: Theory and equivalent circuit," *IEEE Trans. Power Deliv.*, vol. 16, no. 2, pp. 171–175, 2001.
- [71] M. N. Touzelbaev, J. Miler, Y. Yang, G. Refai-Ahmed, and K. E. Goodson, "High-Efficiency Transient Temperature Calculations for Applications in Dynamic Thermal Management of Electronic Devices," *J. Electron. Packag.*, vol. 135, no. 3, p. 31001, 2013.
- [72] R. Wu, H. Wang, K. Ma, P. Ghimire, F. Iannuzzo, and F. Blaabjerg, "A temperature-dependent thermal model of IGBT modules suitable for circuit-level simulations," *2014 IEEE Energy Convers. Congr. Expo. ECCE 2014*, vol. 52, no. 4, pp. 3306–3314, 2014.
- [73] Z. Wang and W. Qiao, "A Physics-Based Improved Cauer-Type Thermal Equivalent Circuit for IGBT Modules," *IEEE Trans. Power Electron.*, vol. 31, no. 10, pp. 6781–6786, 2016.
- [74] Aldo Boglietti, Andrea Cavagnino, David Staton, Martin Shanel, Markus Mueller, and Carlos Mejuto, "Evolution and Modern Approaches for Thermal Analysis of Electrical Machines," *IEEE Trans. Ind. Electron.*, vol. 56, no. 3, pp. 871–882, 2009.
- [75] P. Mellor, D. Roberts, and D. Turner, "Lumped parameter thermal model for electrical machines of TEFC design," *IEE Proc. B (Electric Power ...)*, vol. 138, no. 5, 1991.

- [76] A. Boglietti, A. Cavagnino, and D. A. Staton, "TEFC induction motors thermal models: a parameter sensitivity analysis," *IEEE Trans. Ind. Appl.*, vol. 41, no. 3, pp. 756–763, 2005.
- [77] T. a Jankowski, F. C. Prenger, D. D. Hill, S. R. O. Bryan, K. K. Sheth, E. B. Brookbank, D. F. a Hunt, and Y. a Orrego, "Development and validation of a thermal model for electric induction motors," *IEEE Trans. Ind. Electron.*, vol. 57, no. 12, pp. 4043–4054, 2010.
- [78] N. Rostami, M. Feyzi, J. Pyrhönen, A. Parviainen, and M. Niemelä, "Lumped-Parameter Thermal Model for Axial Flux Permanent Magnet Machines," *Magn. IEEE Trans.*, vol. PP, no. 99, p. 1, 2012.
- [79] A. Boglietti, E. Carpaneto, M. Cossale, A. L. Boriera, D. Staton, and M. Popescu, "Electrical machine first order short-time thermal transients model: Measurements and parameters evaluation," *IECON Proc. (Industrial Electron. Conf.)*, vol. 40th Annua, pp. 555–561, 2014.
- [80] K. S. Kim, B. H. Lee, H. J. Kim, J. P. Hong, and J. H. Jun, "Thermal analysis of outer rotor type IPMSM using thermal equivalent circuit," *15th Int. Conf. Electr. Mach. Syst.*, vol. 2, no. 2, 2012.
- [81] K. S. Kim, H. J. Kim, and J. P. Hong, "Thermal Equivalent Circuit Network for Outer Rotor Type Motors," *Power Electron. Mach. Drives (PEMD 2014), 7th IET Int. Conf. on. IET*, no. 1, pp. 1–4, 2014.
- [82] A. G. D. Kuehbacher D. Kelleter, "An improved approach for transient thermal modeling using lumped parameter networks," *IEEE Int.*, no. table II, pp. 824–831, 2013.
- [83] C. K. Member, A. Haumer, M. Haigis, and H. Lang, "Comparison of Measurements with a CFD Analysis and a Thermal Equivalent Circuit Model of a TEFC Induction Machine," vol. 24, no. 4, pp. 809–818, 2009.
- [84] Y. S. Choi and D. M. Kang, "Prediction of thermal behaviors of an air-cooled lithium-ion battery system for hybrid electric vehicles," *J. Power Sources*, vol. 270, pp. 273–280, 2014.
- [85] Z. Gao, C. Chin, W. Woo, and J. Jia, "Integrated Equivalent Circuit and Thermal Model for Simulation of Temperature-Dependent LiFePO<sub>4</sub> Battery in Actual Embedded Application," *Energies*, vol. 10, no. 1, p. 85, 2017.
- [86] M. Debert, G. Colin, G. Bloch, and Y. Chamaillard, "An observer looks at the cell temperature in automotive battery packs," *Control Eng. Pract.*, vol. 21, no. 8, pp. 1035–1042, 2013.
- [87] X. Lin, H. E. Perez, J. B. Siegel, A. G. Stefanopoulou, Y. Li, R. D. Anderson, Y. Ding, and M. P. Castanier, "Online Parameterization of Lumped Thermal Dynamics in Cylindrical Lithium Ion Batteries for Core Temperature Estimation and Health Monitoring," vol. 21, no. 5, pp. 1–11, 2012.
- [88] X. Lin, H. E. Perez, S. Mohan, J. B. Siegel, A. G. Stefanopoulou, Y. Ding, and M. P. Castanier, "A lumped-parameter electro-thermal model for cylindrical batteries," *J. Power*

*Sources*, vol. 257, pp. 1–11, 2014.

- [89] C. Forgez, D. Vinh Do, G. Friedrich, M. Morcrette, and C. Delacourt, “Thermal modeling of a cylindrical LiFePO<sub>4</sub>/graphite lithium-ion battery,” *J. Power Sources*, vol. 195, no. 9, pp. 2961–2968, 2010.
- [90] K. Smith and C.-Y. Wang, “Power and thermal characterization of a lithium-ion battery pack for hybrid-electric vehicles,” *J. Power Sources*, vol. 160, no. 1, pp. 662–673, 2006.
- [91] K. Smith, G.-H. Kim, E. Darcy, and A. Pesaran, “Thermal/electrical modeling for abuse-tolerant design of lithium ion modules,” *Int. J. Engine Res.*, vol. 34, pp. 204–215, 2010.
- [92] N. Damay, C. Forgez, M. P. Bichat, and G. Friedrich, “Thermal modeling of large prismatic LiFePO<sub>4</sub>/graphite battery. Coupled thermal and heat generation models for characterization and simulation,” *J. Power Sources*, vol. 283, pp. 37–45, 2015.
- [93] J. Neubauer and E. Wood, “Thru-life impacts of driver aggression, climate, cabin thermal management, and battery thermal management on battery electric vehicle utility,” *J. Power Sources*, vol. 259, pp. 262–275, 2014.
- [94] J. Fraden, *Handbook of Modern Sensors*, Fourth. New York, NY: Springer New York, 2010.
- [95] R. J. Moffat, “Describing the uncertainties in experimental results,” *Exp. Therm. Fluid Sci.*, vol. 1, no. 1, pp. 3–17, Jan. 1988.
- [96] National Aeronautics and Space Association, “Measurement uncertainty analysis principles and methods,” *NASA Meas. Qual. Assur. Handb.*, no. July, pp. 1–275, 2010.
- [97] A. S. Morris, *Measurement and Instrumentation Principles*, 3rd ed. Butterworth-Heinemann, 2001.
- [98] D. Yu and S. Yuvarajan, “A novel circuit model for PEM fuel cells,” *Proc. 19th Annu. IEEE Appl. Power Electron. Conf. Expo.*, vol. 1, no. C, pp. 362–366, 2004.
- [99] T. Jokinen and J. Saari, “Modelling of the coolant flow with heat flow controlled temperature sources in thermal networks,” *IEE Proceedings, Elect. Power Appl.*, vol. 144, no. 5, pp. 1–5, 1997.
- [100] A. Loges, S. Herberger, P. Seegert, and T. Wetzel, “A study on specific heat capacities of Li-ion cell components and their influence on thermal management,” *J. Power Sources*, vol. 336, pp. 341–350, 2016.
- [101] C. Tropea, A. L. Yarin, and J. F. Foss, *Springer handbook of experimental fluid mechanics*. Springer, 2007.
- [102] W.-H. Hucho, *Aerodynamics of road vehicles*, Fourth Edi. SAE International, 1998.
- [103] W. K. George, P. D. Beuther, and A. Shabbir, “Polynomial calibration for how wire in thermally varying flows,” *Exp. Therm. Fluid Sci.*, pp. 230–235, 1987.

- [104] S. A. Sherif, "Hot-wire/film anemometry measurements in flows with heat transfer and signal correction," *ISA Trans.*, vol. 37, pp. 141–146, 1998.
- [105] M. Manshadi and M. Esfeh, "Analytical and Experimental Investigation About Heat Transfer of Hot-Wire Anemometry," *An Overv. Heat Transf. Phenom.*, pp. 67–88, 2012.
- [106] I. S. Technology, "Application note: thermal mass flow sensor FS5," 2015.
- [107] R. Y. Que, R. Zhu, Q. Z. Wei, and Z. Cao, "Temperature compensation for thermal anemometers using temperature sensors independent of flow sensors," *Meas. Sci. Technol.*, vol. 22, no. 8, p. 85404, 2011.
- [108] P. Bradshaw and R. C. Pankhurst, "The design of low-speed wind tunnels," *Prog. Aerosp. Sci.*, vol. 5, pp. 1–69, 1964.
- [109] M. A. Ardekani and F. Farhani, "Practical considerations for validity of constant temperature anemometer flow measurements in industrial applications," *Flow Meas. Instrum.*, vol. 21, no. 2, pp. 123–127, 2010.

# APPENDICES

## APPENDIX A: RESISTOR TOLERANCE SHEET

Table A1 - Resistor tolerance data

Resistor / Area {m <sup>2</sup> }	$R_i$ {°C/W}	$\Delta T_i$ {°C}	$\frac{\partial R}{\partial \Delta T}$	$\dot{Q}_i$ {W}	$\frac{\partial R}{\partial \dot{Q}}$	$B_R$	$S_R$	$U_R$ {°C/W}
$R_{bp}$ 0.6590	0.194	7.133	0.0307	37.55	0.0055	0.0113	0.0005	3.23
$R_{man\ inlet}$ 0.1623	0.314	2.733	0.1366	8.69	0.0409	0.0249	0.0004	7.18
$R_{man\ outlet}$ 0.1623	0.259	2.400	0.1299	8.99	0.0314	0.0209	0.0003	6.02
$R_{side\ inlet}$ 0.2474	0.196	2.500	0.1010	12.28	0.0178	0.0173	0.0003	4.98
$R_{side\ outlet}$ 0.2474	0.230	2.533	0.1090	10.92	0.0234	0.0211	0.0003	6.07
$R_{top1}$ 0.2474	0.134	1.633	0.1023	12.05	0.0128	0.0161	0.0002	4.64
$R_{top2}$ 0.4168	0.305	4.800	0.0759	15.93	0.0219	0.0287	0.0005	8.27
$R_{end}$ 0.268	0.207	3.667	0.0676	17.72	0.0135	0.0132	0.0002	3.79
$R_{bot}$ 0.5116	0.127	5.233	0.0286	40.09	0.0034	0.0061	0.0001	1.77
$R_{ag\ man\ outlet}$ 0.1623	0.853	7.167	0.1415	8.60	0.1172	0.0592	0.0010	17.05
$R_{ag\ man\ inlet}$ 0.1623	0.726	6.267	0.1383	8.84	0.0974	0.0498	0.0008	14.34
$R_{ag\ side\ outlet}$ 0.2474	0.496	6.100	0.0989	12.20	0.0462	0.0359	0.0006	10.36
$R_{ag\ side\ inlet}$ 0.2474	0.528	6.100	0.1012	12.04	0.0529	0.0408	0.0007	11.76
$R_{ag\ top}$ 0.2474	0.372	5.167	0.0779	15.04	0.0293	0.0375	0.0007	10.81
$R_{ag\ end}$ 0.268	0.473	7.733	0.0711	16.80	0.0330	0.0277	0.0005	7.97
$R_{bh1}$ 0.0544	1.087	6.567	0.1965	6.31	0.2169	0.0415	0.0007	11.95

Table A2 - Resistor tolerance data continued

<b>Resistor / Area {m<sup>2</sup>}</b>	<b><math>R_i</math> {°C/W}</b>	<b><math>\Delta T_i</math> {°C}</b>	<b><math>\frac{\partial R}{\partial \Delta T}</math></b>	<b><math>\dot{Q}_i</math> {W}</b>	<b><math>\frac{\partial R}{\partial \dot{Q}}</math></b>	<b><math>B_R</math></b>	<b><math>S_R</math></b>	<b><math>U_R</math> {°C/W}</b>
<b><math>R_{c\ man}</math> 0.4354</b>	0.034	1.250	0.0269	37.12	0.0008	0.0031	0.0001	0.90
<b><math>R_{c\ side}</math> 0.4538</b>	0.020	0.900	0.0226	44.18	0.0004	0.0025	0.0000	0.73
<b><math>R_{c\ top}</math> 0.4122</b>	0.062	1.800	0.0344	29.07	0.0018	0.0044	0.0002	1.26
<b><math>R_{oc\ man}</math> 0.4354</b>	0.390	14.000	0.0279	35.88	0.0093	0.0126	0.0010	3.66
<b><math>R_{oc\ side}</math> 0.4538</b>	0.360	15.600	0.0231	43.30	0.0073	0.0102	0.0008	2.98
<b><math>R_{oc\ top}</math> 0.4122</b>	0.569	11.500	0.0495	20.20	0.0221	0.0278	0.0022	8.11
<b><math>R_{obp}</math> 0.6590</b>	0.225	8.333	0.0307	37.55	0.0063	0.0129	0.0006	3.74
<b><math>R_{obh}</math> 0.0544</b>	2.368	14.133	0.1965	6.31	0.4640	0.0788	0.0034	22.78
<b><math>R_{bh2}</math> 0.0544</b>	4.295	6.681	0.7251	1.53	2.5051	0.4165	0.0198	120.53
<b><math>R_{int}</math></b>	0.003	0.483	0.0099	161.31	0.0000	0.0011	0.0000	0.31

## APPENDIX B: TRANSIENT LAB TESTING RESULTS @ 37 °C

### Temperature Profiles

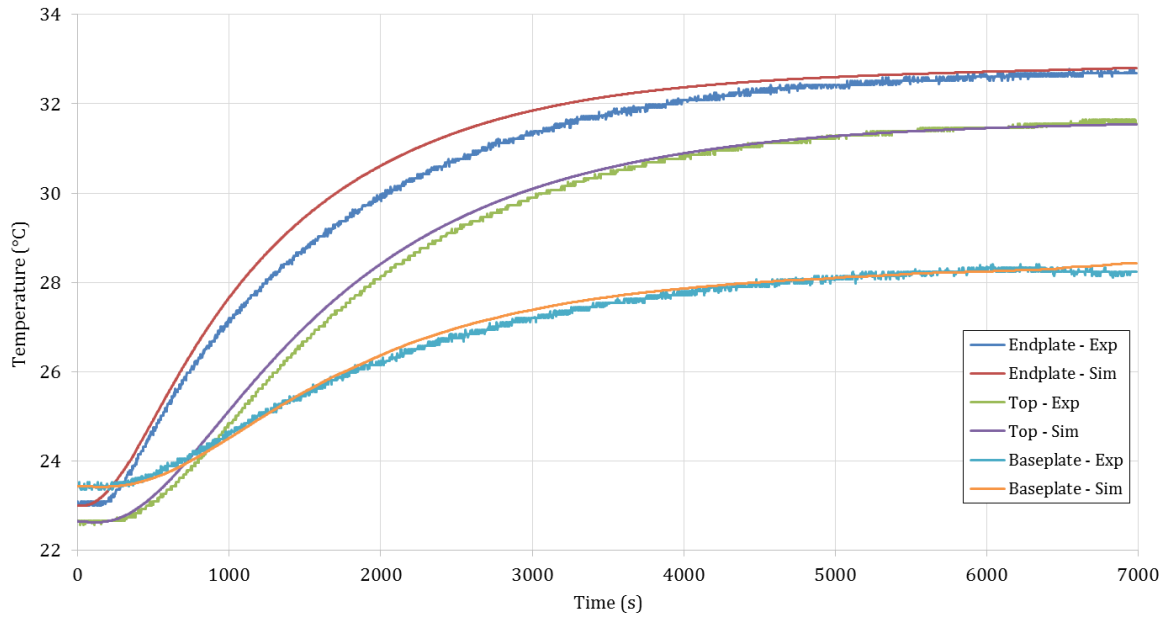


Figure A1 - Simulated vs. measured temperatures: endplate, top, and baseplate

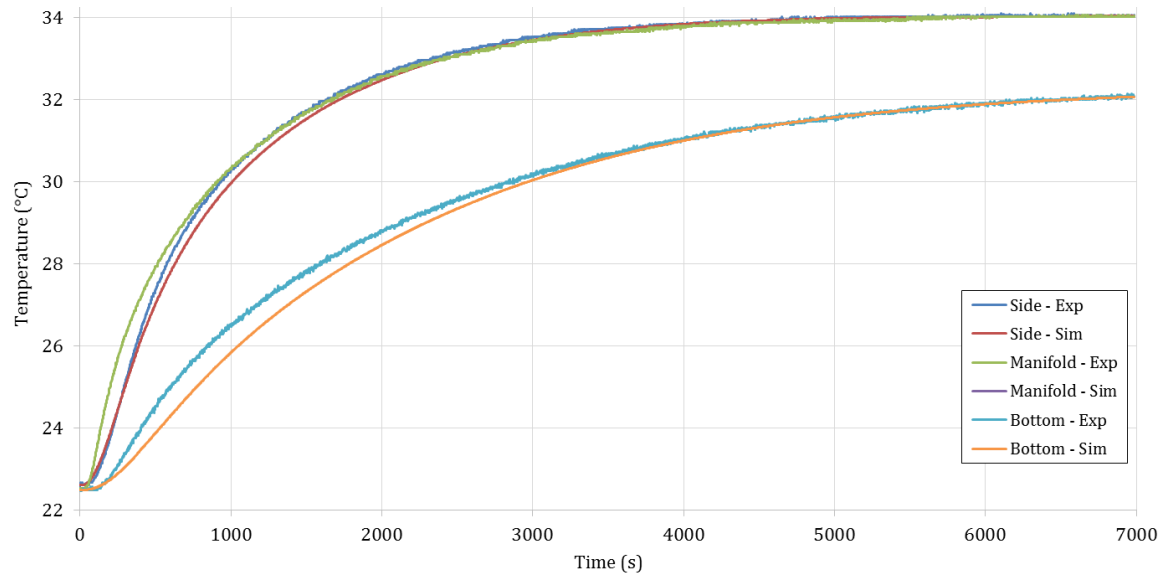


Figure A2 - Simulated vs. measured temperatures: side and manifold

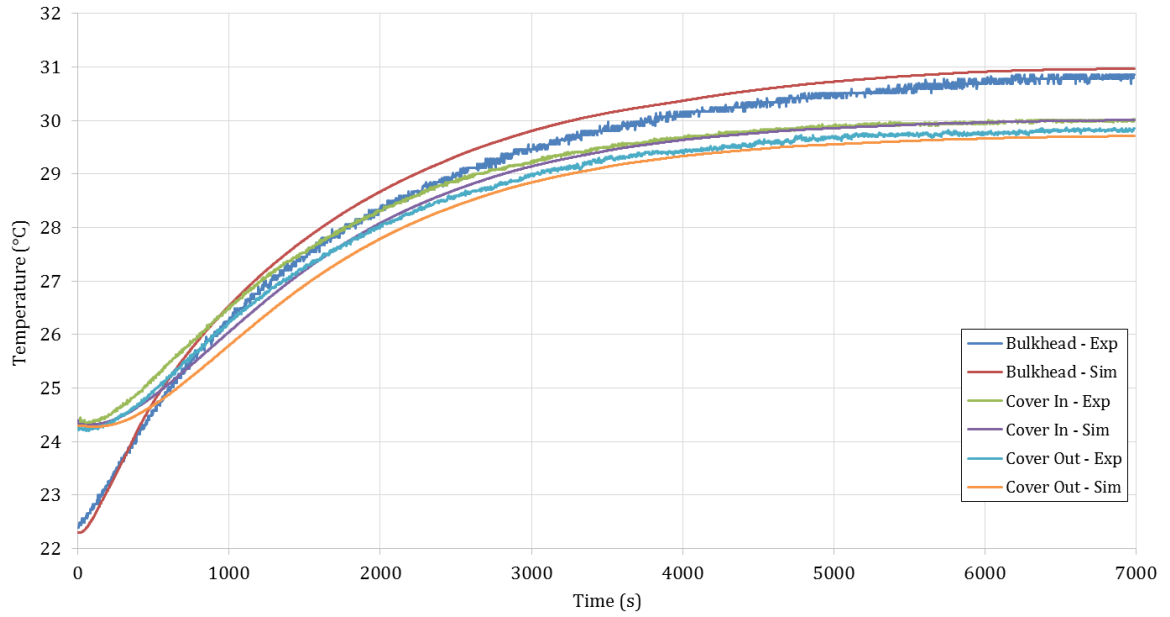


Figure A3 - Simulated vs. measured temperatures: bulkhead, inside cover, and outside cover

Table A3 - Absolute maximum and RMS errors in temperature during transient heating

<b>Component ↓</b>	<b>Absolute Max Error {°C}</b>	<b>RMS Error {°C}</b>	<b>RMS Error {% ΔT}</b>
<b>Endplate</b>	0.84	0.41	4.2
<b>Top</b>	0.39	0.18	2.0
<b>Side</b>	0.42	0.14	1.2
<b>Manifold</b>	1.44	0.38	3.3
<b>Bottom</b>	0.79	0.30	3.1
<b>Baseplate</b>	0.35	0.12	2.4
<b>Bulkhead</b>	0.47	0.26	3.1
<b>Inside Cover</b>	0.50	0.20	3.5
<b>Outside Cover</b>	0.48	0.20	4.4

## Heat Flow Profiles

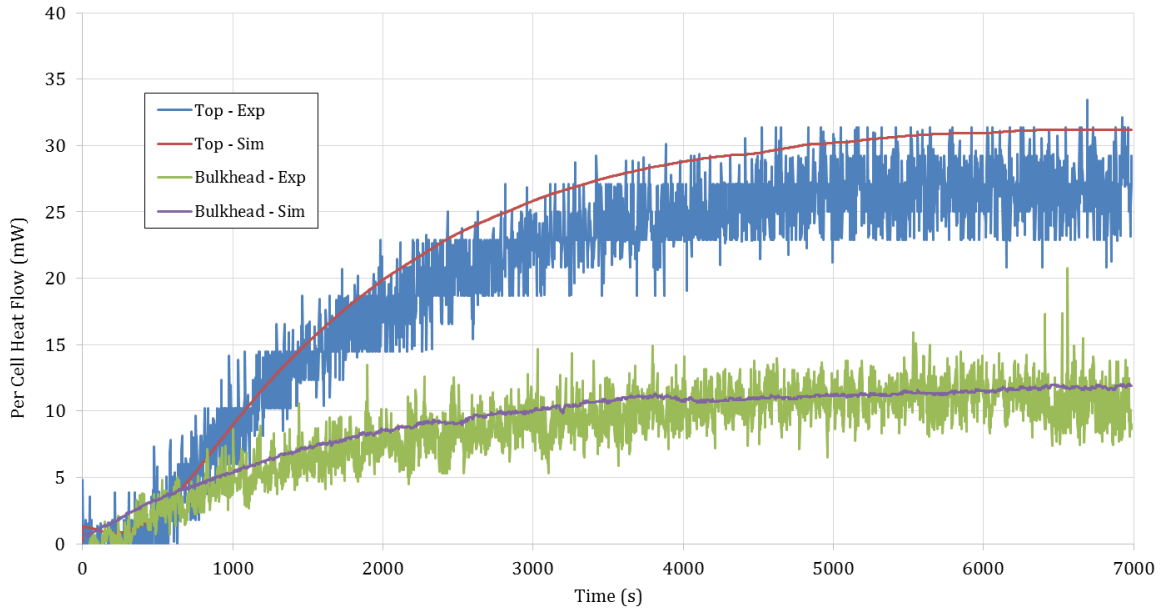


Figure A4 - Simulated vs. measured heat flow: top and bulkhead

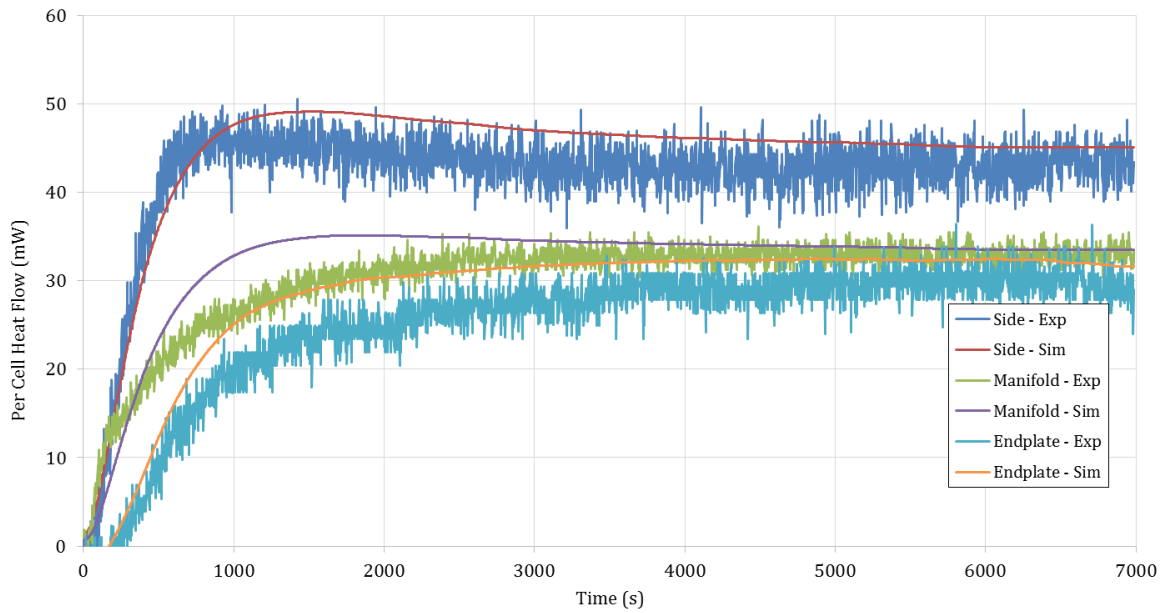


Figure A5 - Simulated vs. measured heat flow: side, manifold, and endplate

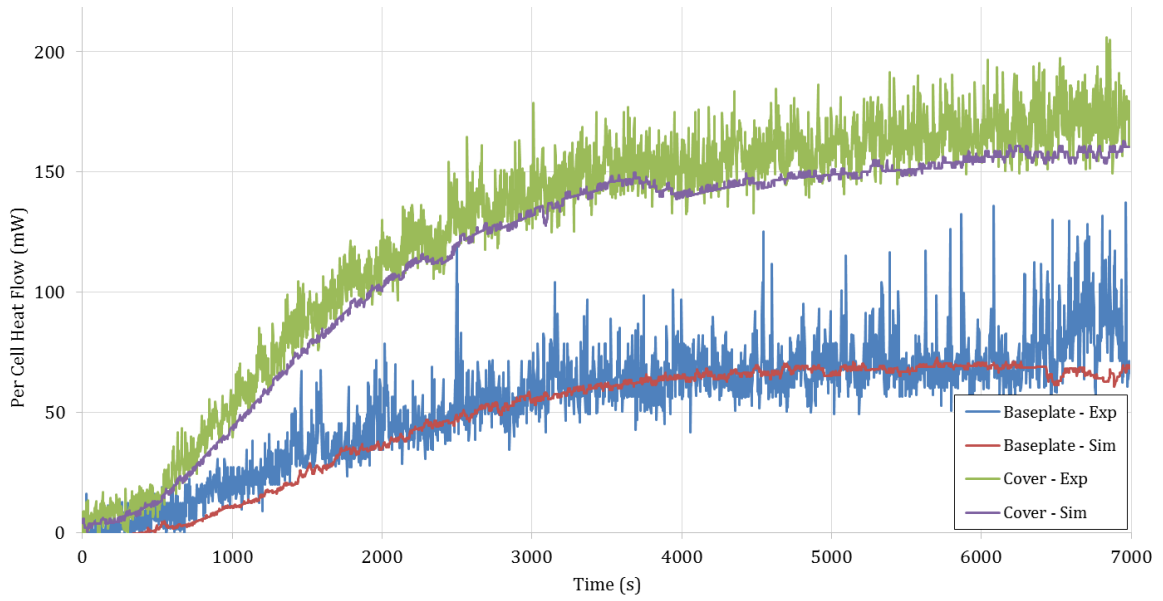


Figure A6 - Simulated vs. measured heat flow: baseplate and cover

Table A4 - Absolute maximum and RMS errors in heat flow during transient heating and signal noise levels

Component ↓	Max absolute error {mW}	RMS Error {mW}	Signal Noise {mW}
<b>Endplate</b>	10.98	4.00	1.55
<b>Top</b>	10.39	3.81	2.14
<b>Side</b>	10.86	3.70	2.00
<b>Manifold</b>	9.01	3.11	0.97
<b>Baseplate</b>	70.74	12.28	14.09
<b>Bulkhead</b>	9.02	1.59	1.55
<b>Cover</b>	52.49	13.49	10.12